

PROTON SCATTERING FROM POLARIZED HELIUM-3

IN THE ENERGY RANGE FROM 20 TO 35 MEV

By

Petrus J.T. Verheijen

A thesis submitted to the University of Manitoba in partial fulfillment
of the requirements for the degree of Doctor of Philosophy.

1983

THE UNIVERSITY OF MANITOBA
FACULTY OF GRADUATE STUDIES

The undersigned certify that they have read, and recommend to
the Faculty of Graduate Studies for acceptance, a Ph.D. thesis
entitled: Proton Scattering From Polarized Helium-3
..... in the Energy Range from 20 to 35 MEV
.....
.....
submitted by Petrus J.T. Veheijen
in partial fulfilment of the requirements for the Ph.D. degree.

U. Veheijen
.....
Advisor
.....
J. Brown
.....
W. Feld
.....
G.S. Clark
.....

.....
Dr. S.D. Baker
.....
External Examiner
.....
Department of Physics
.....
Rice University
.....
Houston, Texas. 77251
.....

Date of oral examination: September 7th, 1983.
The student has satisfactorily completed and passed the Ph.D.
oral examination.

U. Veheijen
.....
Advisor
.....
J. Brown
.....
W. Feld
.....
G.S. Clark
.....

.....
H.C. Card
.....
Chairman of Ph.D. Oral*

(*The signature of the Chairman does not necessarily signify that
the Chairman has read the complete thesis.)

PROTON SCATTERING FROM POLARIZED HELIUM-3
IN THE ENERGY RANGE FROM 20 TO 35 MEV

by

Petrus J.T. Verheijen

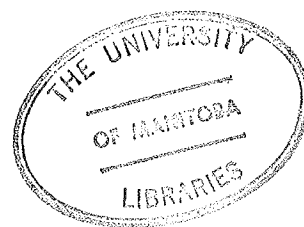
A thesis submitted to the Faculty of Graduate Studies of
the University of Manitoba in partial fulfillment of the requirements
of the degree of

DOCTOR OF PHILOSOPHY

© 1983

Permission has been granted to the LIBRARY OF THE UNIVER-
SITY OF MANITOBA to lend or sell copies of this thesis, to
the NATIONAL LIBRARY OF CANADA to microfilm this
thesis and to lend or sell copies of the film, and UNIVERSITY
MICROFILMS to publish an abstract of this thesis.

The author reserves other publication rights, and neither the
thesis nor extensive extracts from it may be printed or other-
wise reproduced without the author's written permission.



ABSTRACT

The ^3He analyzing powers have been measured at the forward angles ($\leq 100^\circ$) and at energies of 25, 30, 32.5, and 35 MeV. A polarized ^3He target has been built using optical pumping with ^4He -discharge lamps. An improved version of the equations describing the balance between polarizing and depolarizing processes was developed. Polarization through excitation of alternative transitions is discussed. Among the depolarizing processes, especially the reabsorption of pumping light is considered. The experience with the polarized target in nuclear scattering experiments is described. Single energy phase shift analyses have been made using the available precise data at seven energies between 19.5 and 35 MeV. Real phases up to $L=4$, imaginary phases up to $L=3$, and coupling between channels with $J=1$ and 2 were allowed in the analysis. Singlet and triplet waves of the same angular momentum have considerable mixing, which reaches a maximum at 31 and 28 MeV for channels with respectively $J^\pi = 1^-$ and 2^+ . Mixing angles for tensor coupling were always found to be close to zero. Several ambiguities in previous phase shift analyses are clarified. Also, the real phases have a smoother energy dependence than was found before. No significant excursions in the imaginary phases could be detected.

TABLE OF CONTENTS

List of Figures	v
List of Tables	vii
Acknowledgements	ix
I. INTRODUCTION	1
II. POLARIZATION OF HELIUM-3	
A. Methods	8
B. Atomic Levels and Transitions	10
C. Polarization Kinetics	17
D. Target Cell	25
E. Instrumentation	30
F. Polarization Measurement	34
III. NUCLEAR SCATTERING EXPERIMENT	
A. Instrumentation	44
B. Preparatory Experiments	51
C. False Asymmetries and Measurement Procedure	53
IV. DATA PROCESSING	
A. Procedure	59
B. Consistency Tests	67
C. Results and Error Analysis	70
V. PHASE SHIFT ANALYSIS	
A. Introduction	76
B. Computer Program SHOSH2	80
C. Procedure and Results	84
D. Discussion	99

VI. CONCLUSION AND RECOMMENDATIONS

A. ^3He Polarization	108
B. ^3He Analyzing Powers	111
C. Phase Shift Analysis	112

APPENDIX A: OPTICAL PUMPING FROM THE TRIPLET METASTABLE STATE

IN HELIUM-3	114
-------------	-----

APPENDIX B: ESTIMATION OF THE REABSORPTION FACTOR

REFERENCES	142
------------	-----

LIST OF FIGURES

1.1	Isobar diagram of the four-nucleon system.	2
2.1	Schematic describing optical pumping on the metastable state of ^3He to polarize the ground state.	9
2.2	Energy level diagram for helium up to $n=5$.	11
2.3	Transition sequences for optical pumping showing only the favoured possibilities.	13
2.4	Schematic hyperfine structure and Zeeman splitting of the triplet S-states and P-states in ^3He , and the transitions occurring in conventional optical pumping.	15
2.5	Inverse of the extrapolated polarization as a function of the absorption factor, $a_n = n\sigma R$, for various values of the collision mixing probability, u .	26
2.6	Target cell.	27
2.7	Expected duration of the scattering experiment as a function of the cell pressure for (a) a cell without background proton scattering, (b) the cell of Fig. 2.6, and (c) a spherical cell.	29
2.8	Experimental layout of the apparatus for polarization and its measurement.	32
2.9	Sketch of the fluorescence signal during a measurement cycle.	35
2.10	Weak discharge intensity dependence of the polarization.	37
2.11	Pumping light intensity dependence of the polarization.	38
2.12	Fluorescence signal at zero polarization as a function of the weak discharge intensity.	43
3.1	Beamline configuration.	45
3.2	Scattering chamber.	47
3.3	Block diagram of the electronics for one telescope.	49
3.4	Timing diagram.	50
3.5	Peak-to-background ratios for measurements taken at 30 and 32.5 MeV at the forward angles.	54
4.1	Spectrum illustrating the method of defining the	60

	background and determining the peak area.	
4.2	Histogram of the reduced chi-square value calculated from the background fit to (a) one spectrum each time, and (b) two spectra simultaneously.	62
4.3	The distribution of consistency measures defined in the text [Eqs. (IV.19) to (IV.22)]. Smooth curves are the expected distributions.	71
4.4	A comparison of analyzing power data at 25 MeV with those of Muller et al. (Mul78). The smooth curve is calculated from the phase shift analysis in Sec. V.	73
4.5	^3He Analyzing powers at 30, 32.5 and 35 MeV. The smooth curves are calculated from the phase shift analysis in Sec. V.	74
5.1	Comparison of the data at 27.5 MeV and the observables calculated from the phase shift analysis.	89
5.2	Phase shifts for partial waves with $J = 0$.	92
5.3	Phase shifts and mixing angle for partial waves with $J = 1^-$.	93
5.4	Phase shifts and mixing angle for partial waves with $J = 1^+$.	94
5.5	Phase shifts and mixing angle for partial waves with $J = 2^+$.	95
5.6	Phase shifts and mixing angle for partial waves with $J = 2^-$.	96
5.7	Phase shifts for the $^3\text{D}_3^-$, $^1\text{F}_3^-$, $^3\text{F}_3^-$, and $^3\text{F}_4^-$ -waves.	97
5.8	Phase shifts for the G-waves.	98
A.1	Comparison of optical pumping efficiency with a laser tuned to either of five lines at minimum and at maximum collision mixing.	126
A.2	Comparison of optical pumping efficiency with an ^3He and an ^4He -lamp at minimum and at maximum collision mixing.	127
B.1	Spectral profile of the $2^3\text{S} - 2^3\text{P}$ transition in ^3He showing the division in groups adopted here.	129
B.2	Reabsorption factor as a function of the absorption factor for pumping light from an ^4He -lamp at different values of the collision mixing probability.	139

LIST OF TABLES

1.1	Previous results for ${}^3\text{He}(p,p){}^3\text{He}$ differential cross section measurements in the range of 18 to 50 MeV.	4
1.2	Previous results for ${}^3\text{He}(p,p){}^3\text{He}$ polarization measurements in the range of 18 to 50 MeV.	5
2.1	Relative probability of absorption from an S-state with respect to the 1083 nm line and the lifetimes of the excited P-states.	14
2.2	Values of P^2_p and methods of polarization measurement for different polarized ${}^3\text{He}$ targets.	31
3.1	Data obtained for the calibration of the bending magnet with the cross-over technique using a CD_2 -target.	52
3.2	Aperture dimensions and their contribution to the instrumental asymmetry.	56
4.1	Formulas defining the yields in the determination of nuclear scattering asymmetries.	64
4.2	${}^3\text{He}$ analyzing powers from 25 MeV to 35 MeV at angles less than 100° .	72
5.1	Previous reports on single energy phase shift analyses for energies less than 50 MeV.	77
5.2	Sets of real phase shifts and coupling parameters at 19.5 MeV by various authors.	87
5.3	Sets of real phase shifts and coupling parameters between 19.5 and 35 MeV.	91
A.1	Densities of atoms in the magnetic sublevels of the metastable 2^3S -state in equilibrium with polarized ground-state atoms.	115
A.2	Relative transition probabilities for absorption and emission between triplet 2S and 2P magnetic sublevels.	116
A.3	Possible modes of optical pumping with $\Delta m = +1$ from the triplet 2S-state in ${}^3\text{He}$.	117
A.4	Absorption rate of circularly polarized light as a function of the polarization.	123
A.5	Net angular momentum transfer rates (in units \hbar) per absorbed photon.	124

B.1	Grouping of the 2^3S-2^3P transitions that are less than one linewidth apart.	130
B.2	Relative absorption and emission probabilities for unpolarized light matching 2^3S-2^3P transitions.	133

ACKNOWLEDGEMENTS

I would like to thank Dr. W.T.H. van Oers for his guidance, support, and for a leadership, that was at times wearing, but at the end most appreciated. Dr. R.H. McCamis has been a continuous force behind the ^3He -project, and I am indebted to him for years of cooperation.

The scattering chamber was originally designed by D.K. Hasell and Dr. A.M. Sourkes, and it was constructed by the Physics Department Mechanical Workshop.

The original equipment for polarized ^3He -targets and for polarization measurement came from the University of Toronto, where we received cooperation from Dr. J.M. Daniels, Brian Head, Bill Hilgers, Jack Legge, and Dr. A.D. May. Dr. R.E. Brown of Los Alamos Scientific Laboratory provided advice on the R-matrix analysis done at that laboratory.

During the project we also received support from Ron Beavis, Dr. J. Birchall, Angela Bracco, Panos Drakopoulos, Mark de Jong, Claude Lapointe, and Daniel Levin.

Technical support was supplied by the Physics Department, and Cyclotron Laboratory; especially the Electronics Workshop was often called upon. The Chemistry Department, Glass Workshop has provided invaluable cooperation through Bryn Easterbrook and Ian Ward.

Special thanks are reserved for Enilo Ajakaiye and Michel Verheijen, without whom I would not have started this thesis work, and without whom I would not have completed it.

"Education is an admirable thing,
but it is well to remember from
time to time that nothing that is
worth knowing can be taught."

Oscar Wilde - The Critic as Artist

I. INTRODUCTION

The work presented in this thesis is part of a wider effort to find a more complete description of the four-nucleon system. Here we will concentrate on the proton- ^3He scattering system, which is the only method of studying the configuration of three protons and one neutron.

The nucleus that could be formed from these four nucleons, is ^4Li . No bound state exists, because its ground state is estimated to be 4.7 MeV above the summed energy of a proton plus a ^3He particle (Fig. 1.1). From low energy proton- ^3He scattering data (<19 MeV) four levels are deduced to exist (Fig. 1.1, Fia73). Above these levels no further structure has been found, although a preliminary R-matrix analysis (Bro78) indicated fluctuations in the singlet phases. Therefore, further work at proton energies in the range of the University of Manitoba cyclotron, 20 to 48 MeV, became the natural follow-up to the low energy studies.

The attempt to unravel a four-nucleon (or twelve-quark) system is an aim in itself, to which this work is a contribution. Especially, the p- ^3He data are directly applicable to the charge conjugate system, the interaction of a neutron with tritium, assuming charge symmetry of the nuclear forces. There is also the more practical aspect, that ^3He is used in these fusion processes, and that the availability of polarized ^3He significantly improves the efficiency of these fusion processes involving ^3He (Physics Today, August 1982, p. 17). The use of a polarized target is a major component of this thesis work.

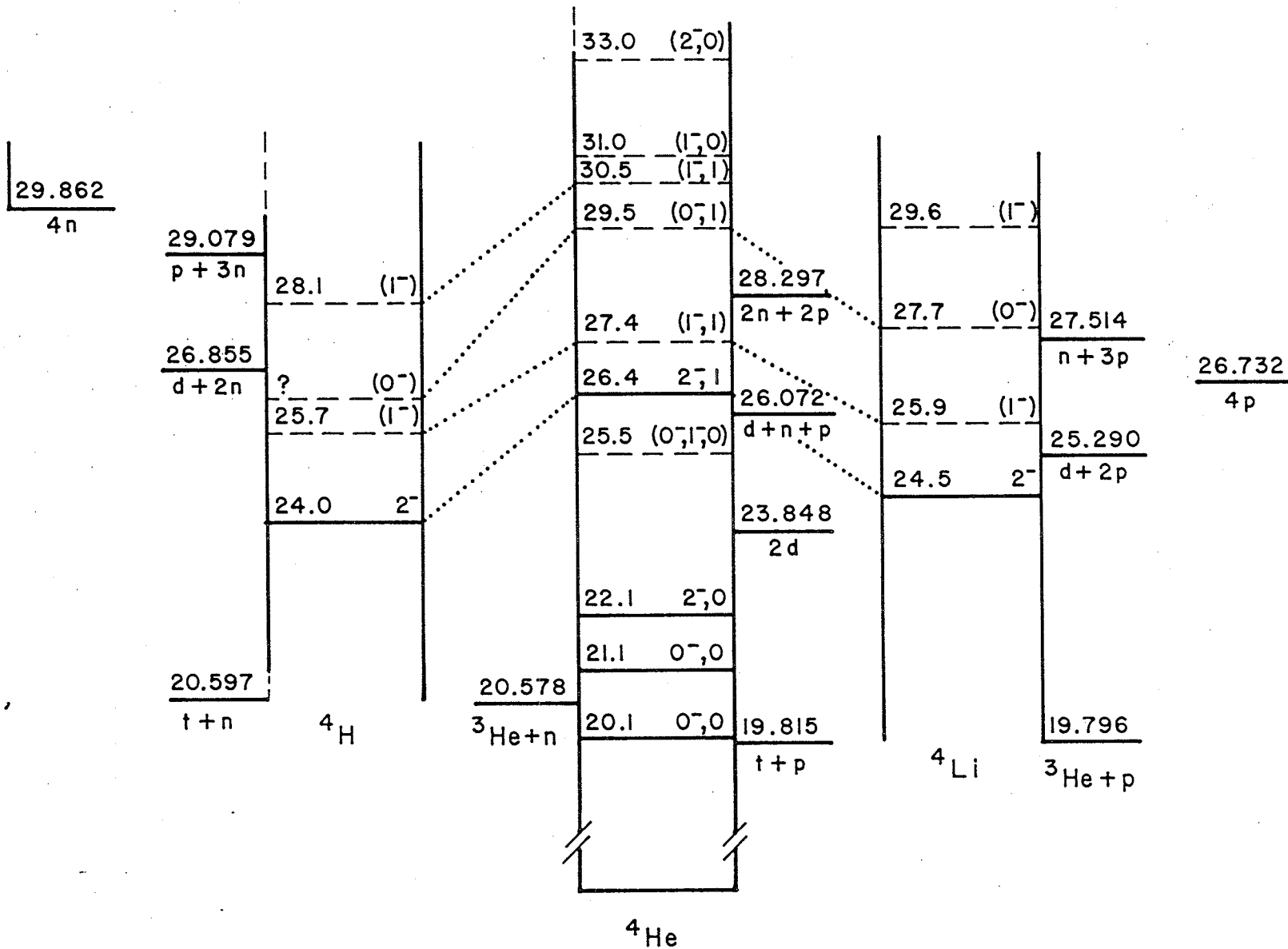


FIG. 1.1 Isobar diagram of the four-nucleon system (after Fia73).

Since the mid 1970s, groups at LBL and Manitoba have coordinated their efforts to produce a set of accurate data on the p - ^3He scattering system in the energy range from 20 to 50 MeV. So far, measurements have been made of the differential cross sections (Mur79), proton analyzing powers (Wat77, Bir81) and total reaction cross sections (Sou76). These, and earlier data form a data base of 1500 points (Tables 1.1 and 1.2, and Sou76).

Only two observables are well represented in the existing data: differential cross sections and proton analyzing powers. In theory, however, at least six different observables are necessary to describe the elastic scattering of two non-identical spinors without interfering reaction channels (LaF80).

The cause of this incompleteness in the data base is associated with the limitations imposed on the preparation of a polarized ^3He -target. Only thin targets (< 1 kPa) with low polarization (< 0.2) have been made using an optical pumping technique devised in the early 1960s (Co163). Such a target has been built, in the first instance, to increase the set of ^3He analyzing powers above 25 MeV (Table 1.2). It had been hoped that with the polarized target and with the development of the polarized proton beam at the University of Manitoba cyclotron, spin correlation parameters could also be measured. To date, these data have been taken only at 8.8 MeV (McS69, 2 data points) and at 19.5 MeV (Bak71, 19 data points). A satisfactorily polarized proton beam has so far not been obtained at the University of Manitoba cyclotron (DeJ81).

Table 1.1. Previous results for ${}^3\text{He}(p,p){}^3\text{He}$ differential cross section measurements in the range of 18 to 50 MeV.

Energy (MeV)	Angle (lab)	Number of datapoints	Error relative	scale	Reference
18.0	14 - 165	about 40	3 %	?	Mor75
19.48	12 - 168	25	0.6 %	0.3 %	Hut71
19.5	10 - 170	46	0.9 %	1.5 %	Mur79
20.0	14 - 165	about 40	3 %	?	Mor75
21.3	10 - 155	42	1.2 %	1.5 %	Mur79
22.5	14 - 165	about 40	3 %	?	Mor75
25.0	14 - 165	about 40	3 %	?	Mor75
25.0	8 - 170	48	1.6 %	1.5 %	Mur79
26.7	15 - 165	36	3 %	?	War75
27.5	14 - 165	about 40	3 %	?	Mor75
27.5	10 - 170	41	1.8 %	1.5 %	Mur79
30.0	14 - 165	about 40	3 %	?	Mor75
30.0	10 - 160	44	1.2 %	1.5 %	Mur79
30.6	11 - 156	42	3 %	4 %	Har70
31.0	6 - 160	39	4 %	?	Kim64
32.4	8 - 170	48	1.8 %	1.5 %	Mur79
35.0	14 - 165	about 40	3 %	?	Mor75
35.0	10 - 160	42	1.2 %	1.5 %	Mur79
37.5	8 - 160	40	2.5 %	1.5 %	Mur79
40.0	8 - 170	47	3.4 %	1.5 %	Mur79
42.7	14 - 165	about 40	3 %	?	Mor75
45.0	14 - 165	about 40	3 %	?	Mor75
45.0	8 - 170	36	1.6 %	1.5 %	Mur79
47.5	8 - 170	44	1.7 %	1.5 %	Mur79
48.5	14 - 165	about 40	3 %	?	Mor75
49.5	15 - 156	31	6 %	4 %	Har70

Table 1.2. Previous results for $^3\text{He}(p,p)^3\text{He}$ polarization measurements in the range of 18 to 50 MeV.

Energy (MeV)	Angle (lab)	Number of datapoints	Error relative	scale	Reference
Proton analyzing power					
19.4	38 - 115	13	0.007	4 %	Bak71
19.7	20 - 145	21	0.019	?	Tiv68
21.3	20 - 149	23	0.012	?	Tiv68
21.44	30 - 160	27	0.006	1.9 %	Wat77
24.84	30 - 160	26	0.006	2.4 %	Wat77
27.26	30 - 160	26	0.009	2.6 %	Wat77
30.0	25 - 150	15	0.06	2 %	Har68
30.0	15 - 155	32	?	?	Dar72
30.12	30 - 160	26	0.008	2.7 %	Wat77
32.4	20 - 150	26	0.006	?	Bir81
35.1	25 - 150	25	0.006	?	Bir81
37.6	20 - 150	27	0.008	?	Bir81
40.1	20 - 150	26	0.006	?	Bir81
45.0	20 - 160	29	0.008	?	Bir81
47.6	25 - 160	28	0.008	?	Bir81
49.0	18 - 160	17	0.11	2 %	Har70
49.6	50 - 155	15	0.010	?	Bir81
^3He analyzing power					
19.4	38 - 112	11	0.03	12 %	Bak71
19.4	38	1	0.011	5 %	War75
19.6	135	1	0.04	?	Mul78
21.1	135	1	0.04	?	Mul78
23.4	135	1	0.04	?	Mul78
25.0	35 - 145	9	0.03	?	Mul78
26.5	135	1	0.04	?	Mul78
26.8	30 - 150	15	0.022	5 %	War75
Spin-correlation parameters					
19.4	38 - 112	19	0.04	13 %	Bak71

Beyond data acquisition, there is the analysis of the data in terms of phase shifts and inelasticity parameters, describing the partial wave expansion of the scattering amplitudes. Harbison et al. (Har70) made a first survey at the energy range under consideration. These authors illustrated the incompleteness of the data by obtaining five different solutions on the basis of two observables. This analysis and other phase shift analyses will be discussed in chapter 5.

In this thesis, the set of accurate data of the LBL and Manitoba groups will be subjected to a similar single-energy phase shift analysis. This necessarily involves a larger parameter set than at the lower energies, because more partial waves are needed, and because breakup reactions play a more important role. The results provide an independent check on energy-dependent or model dependent phase shift analyses. In particular, they will be compared with the results from an R-matrix parametrization of the phase shifts (Bro78). It is expected that in future, the R-matrix analysis will include all low energy data, and the post-1978 spin-dependent observables (Bro78).

In summary, the objectives of this project included: a) the development of a polarized ^3He target, b) the determination of ^3He analyzing powers above 25 MeV, and c) single-energy phase shift analyses in the energy range under consideration.

Chapter 2 and the appendices describe the theory of polarizing ^3He , and the experimental experience with a polarized ^3He target. The nuclear scattering experiment to obtain ^3He analyzing powers is presented in Chapters 3 and 4. Chapter 5 contains the phase shift

analysis. Finally, Chapter 6 summarizes the results of the previous sections, and discusses future developments.

II. POLARIZATION OF HELIUM-3

A. Methods

So far the only useful technique for polarizing ^3He has been optical pumping of low pressure gas cells as originally developed by Colegrove et al. (Col63). Directing circularly polarized light onto atoms or molecules makes it possible to orient the total angular momentum of these particles and with that the nuclear spin. The polarized light induces a transition, and in the process of absorption and reemission the atom is left with a net nuclear polarization.

In the case of ^3He this situation may be technically realized for the transition between a metastable state and an excited state (Fig. 2.1). The reasons for using this system are that a source of light is fortuitously available to match the energy transition $2^3\text{S}_1-2^3\text{P}_0$, and that thermal collisions between metastable and ground-state atoms effectively transfer the polarization to the ground-state atoms. A detailed description of the method, the polarization kinetics as given by Daniels and Timsit (Dan71a), and the experience gained with its utilization during nuclear scattering experiments will be discussed in this chapter.

Extensions of the optical pumping method have been suggested in order to get denser target cells by using an intermediate vapour such as rubidium (Gam65, Bha82), or by pressurizing low density polarized ^3He gas (Sza70, Tim71c). In these cases the polarizations obtained were too small to be of interest for nuclear scattering experiments. A recent

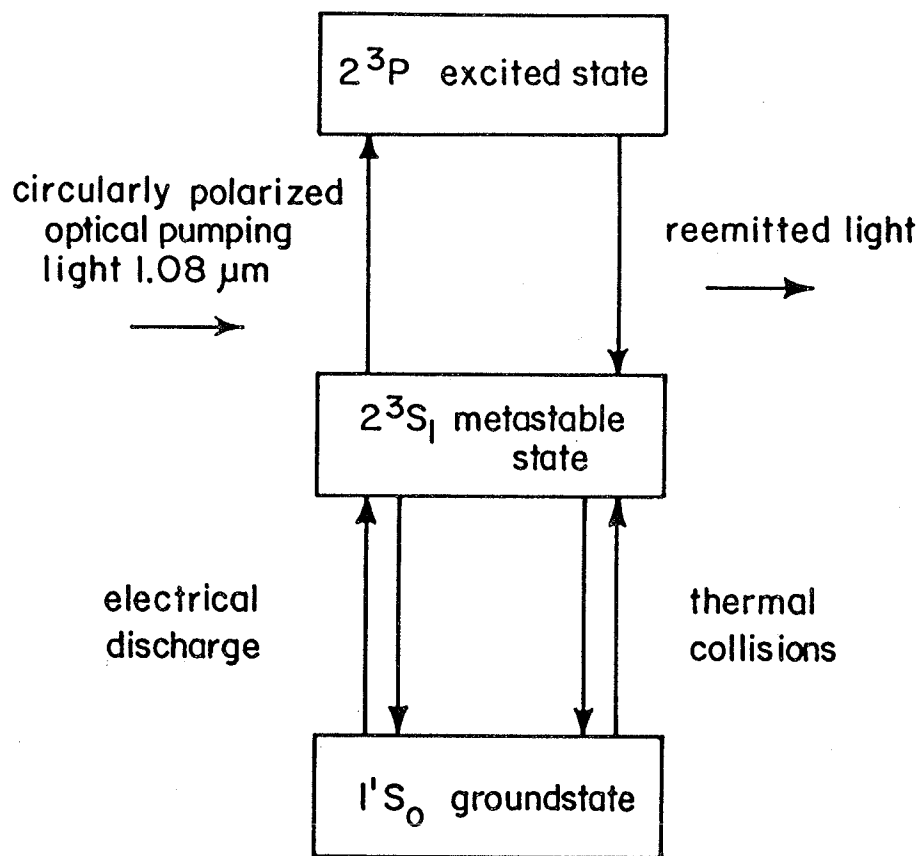


FIG. 2.1 Schematic describing optical pumping on the metastable state of ^3He to polarize the groundstate.

development (Cra83) is the use of laser optical pumping of ^3He gas in dynamical contact with liquid ^3He . Polarizations of 0.5 at a density of 10^{24} m^{-3} have been reported (Cra83), which is a significant improvement over earlier trials with this approach (McA68).

Principally different approaches use the Overhauser and "solid"-effect techniques (Col63), and the "brute-force" technique with high magnetic fields and low temperatures (Gam65). In these cases the reported polarizations were no more than 0.01. Although solid ^3He is antiferromagnetic it was found possible to obtain a weakly ferromagnetic state at temperatures in the order of 1 mK and magnetic fields of greater than 410 mT (Rog83). Further technological developments are necessary to construct in this manner useable targets for nuclear scattering experiments.

B. Atomic Levels and Transitions

Fig. 2.2 depicts the decay scheme of atomic helium. Due to parity conservation, no transitions can take place between the triplet and the singlet states. This leads to two distinct sections in the decay scheme, such that all excited atoms finally decay to the ground state (1^1S_0) or either of two metastable states (singlet 2^1S_0 , triplet 2^3S_1). Both types of metastable atoms will appear in a discharge, where their lifetimes are mainly determined by atomic collisions with impurities and container walls.

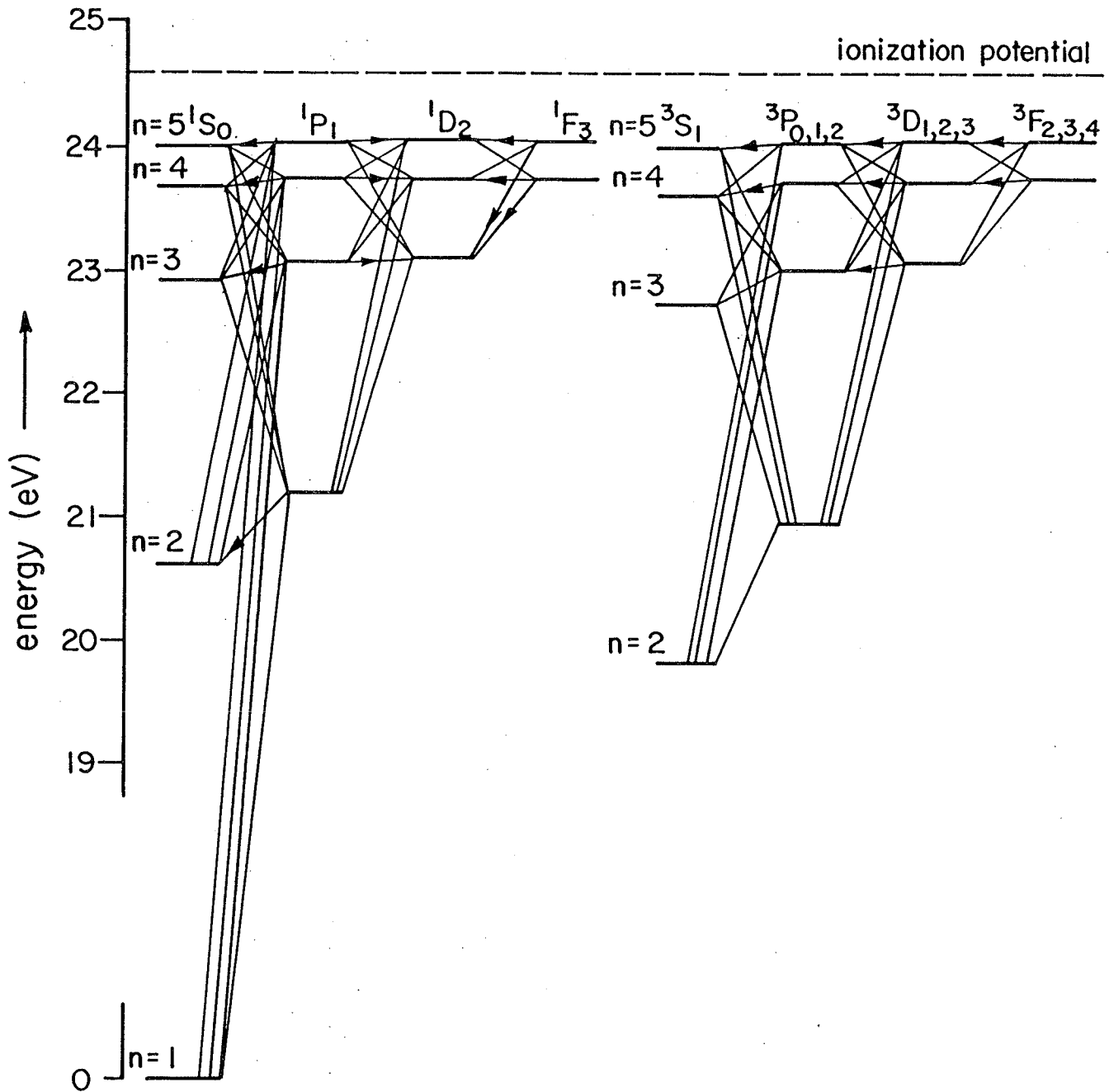


FIG. 2.2 Energy level diagram for helium up to $n=5$.

In order to apply optical pumping, only the long-lived states need to be considered as a starting point for the absorption of circularly polarized light. This limits the possibilities to transitions from the ground state and the two metastable states. The subsequent decay from the excited P-state to any of the lower lying S-states is determined by transition probabilities. In all cases more than 90% of the decays go to the lowest S-state. This means that for optical pumping from the ground state (Fig. 2.3a) and the singlet metastable state (Fig. 2.3b) the endpoint is the ground state, while starting from the triplet metastable state (Fig. 2.3c) results in a decay to that same state.

When the complications due to the hyperfine structure are excluded, the possibilities for optical pumping can be considered for any of the groups in Fig. 2.3. The efficiency of the polarization process is directly proportional to the absorption probability. Table 2.1 lists these relative to the absorption probability of the 1083 nm line calculating the photoabsorption cross section on the assumption that the linewidth is only due to Doppler broadening. A short lifetime of the excited P-state also increases the efficiency because depolarization can be caused by thermal collisions while an atom is still in its excited state. These values (Table 2.1) should be compared with the collision times, which are on the order of 10 ns at 0.13 kPa (1 Torr).

The above is valid for all helium isotopes. In the case of ^3He a further splitting of the levels occurs due to the coupling of the nuclear spin to the electronic spin. This and the Zeeman splitting in the presence of a magnetic field are illustrated in Fig. 2.4 for the case of triplet states and their transitions. The splitting of the

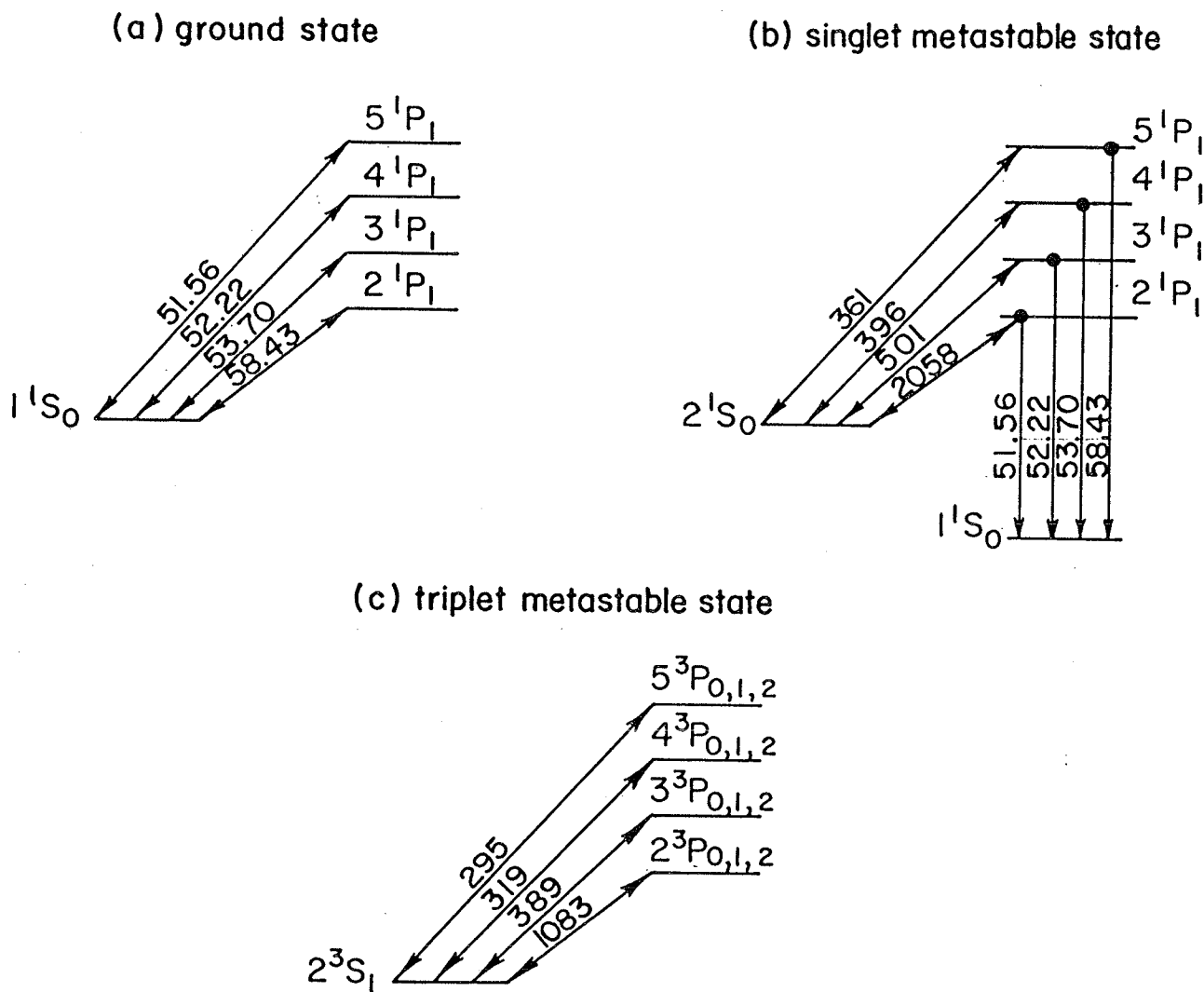


FIG. 2.3 Transition sequences for optical pumping showing only the favoured possibilities. (All wavelengths in nm)

Table 2.1. Relative probability of absorption from an S-state with respect to the 1083 nm line, and the lifetimes of the excited P-states (data adapted from Wie66).

	Rate of spontaneous emission (10^8 s^{-1})	Relative absorption probability	Lifetime (ns)
$1^1\text{S}-2^1\text{P}$	58.43	$1.5 \cdot 10^{-3}$	0.55
3^1P	53.70	$3.3 \cdot 10^{-4}$	1.8
4^1P	52.22	$1.3 \cdot 10^{-4}$	4.1
5^1P	51.56	$6.4 \cdot 10^{-5}$	7.8
$2^1\text{S}-2^1\text{P}$	2058.13	2.5	0.55
3^1P	501.57	$6.0 \cdot 10^{-2}$	1.8
4^1P	396.47	$1.3 \cdot 10^{-2}$	4.1
5^1P	361.36	$4.6 \cdot 10^{-3}$	7.8
$2^3\text{S}-2^3\text{P}$	1083.03	1	98
3^3P	388.86	$1.5 \cdot 10^{-2}$	106
4^3P	318.77	$3.7 \cdot 10^{-3}$	198
5^3P	294.51	$1.6 \cdot 10^{-3}$	341

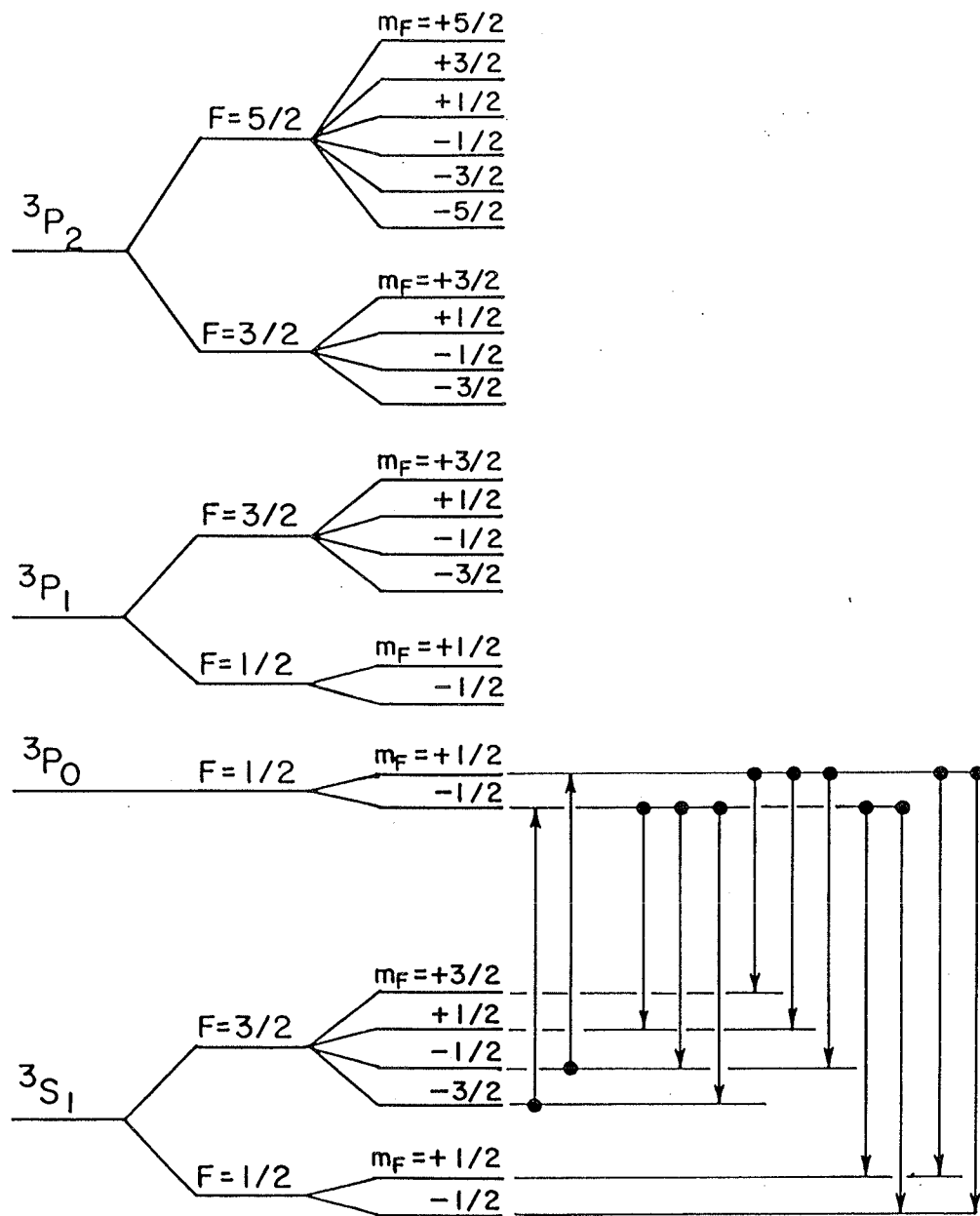


FIG. 2.4 Schematic hyperfine structure and Zeeman splitting of the triplet S-states and P-states in ^3He , and the transitions occurring in conventional optical pumping.

singlet states follows a pattern similar to the structure of the $^3S_1;F=1/2$ and the 3P_1 -states.

Given a source of circularly polarized light, any transition can be excited when the photon energy matches the energy difference within the linewidth of the transition, which is on the order of a few μeV . Because the hyperfine structure typically separates levels by 10 to 100 μeV , absorbed radiation excites the atom to one or a limited number of the F-states. The decay from the excited to the metastable or ground state is allowed to any member of the hyperfine structure of the final state. Appendix A lists all possibilities and shows that any 2^3S-n^3P transition separates into 9 modes each with a slightly different energy.

The 1083 nm transition used here is that from $2^3S_1;F=3/2$ to $2^3P_0;F=1/2$ which decays to $2^3S_1;F=1/2$ or $F=3/2$ (Fig. 2.4). This energy matches within 3.7 μeV that of the $2^3S_1-2^3P_2$ transition in ^4He which is less than the linewidth of 8 μeV (Tim72). No other matchings occur and the other two 2^3S-2^3P lines in the ^4He spectra are well separated from the remaining lines in the ^3He spectrum (Gre64, Tim72). Earlier work (Bak71, Hub69) included a correction for the probability of other transitions to occur. This resulted in apparently higher polarizations. The observations of Timsit and May (Tim72) show that these corrections are not necessary, because the nearest spectral line is more than two linewidths away.

C. Polarization Kinetics

Optical pumping with 1083 nm light requires the existence of metastable atoms and therefore a discharge to create these. Other atoms and molecules also appear in a discharge. Consequently, the presence of a variety of species such as singlet and triplet metastable helium, excited He^* , He^+ -ion and diatomic molecules (He_2 , He_2^* and He_2^+) should be taken into account in depolarization processes. Furthermore, there are contributions to the depolarization from photon trapping, electron interactions, impurities and magnetic field inhomogeneities. Discussions and observations on the various processes are presented by Colegrove et al. (Col63), Scheerer and Walters (Sch65), Byerly (Bye67), Daniels and Timsit (Dan71a), Dupont-Roc et al. (Dup73), and Lefevre-Seguin et al. (Lef82).

Here we start from an expression derived earlier for the polarization rate (Dan71a), which differentiates four groups of processes: gain due to optical pumping [Eq. (II.1a)], loss due to photon reabsorption [Eq. (II.1b)], loss due to ground-state relaxation [Eq. (II.1c)] and loss due to metastable state relaxation [Eq. (II.1d)]. Eqs. (II.1)-(II.4) below have the same contents as equations [4.1], [4.8] and [4.10] of Daniels and Timsit (Dan71a), but are given in a different formulation.

$$\frac{dP}{dt} = \frac{2Q}{N} \sum_{m=-1}^{+1} R_m I_m(P) T_m(P) \quad (\text{II.1a})$$

$$-\frac{2Q}{N} r_o P \frac{11}{6} \frac{1 + P^2/11}{1 + P^2/3} \sum_{m=-1}^{+1} R_m I_m(P) \quad (\text{II.1b})$$

$$\frac{-P}{\tau'} \quad (\text{II.1c})$$

$$\frac{-P}{\tau} \frac{n}{N} \frac{11}{3} \frac{1 + P^2/11}{1 + P^2/3} \quad (\text{II.1d})$$

The functions $T_m(P)$ and $I_m(P)$ are defined as

$$T_m(P) = m + w \frac{m - 2P}{1 - \frac{m}{2P}} \quad (\text{II.2})$$

$$I_m(P) = \frac{(1 - P)^{1+m} (1 + P)^{1-m}}{1 + P^2/3} \left(1 - \frac{m}{2P}\right) \quad (\text{II.3})$$

with w defined by

$$\dot{w} = 0.05317 + 0.19683 u, \quad (\text{II.4})$$

where

P = polarization,

t = time (in s),

Q = photon absorption rate (in $s^{-1}m^{-3}$) at $P=0$,

N = density of ground-state atoms (in m^{-3}),

m = change in magnetic quantum number: $-1, 0$ or 1 ,

R_m = relative rates of $m=-1, 0$ or $+1$ transitions,

T_m = net angular momentum transfer per absorbed photon,

- I_m = photon absorption rate relative to $P=0$,
- r_o = reabsorption factor,
- τ' = ground-state relaxation time (in s),
- n = density of triplet metastable atoms (in m^{-3}),
- τ = triplet metastable atom relaxation time (in s), and
- u = probability of collision mixing in the P-state.

The constants R_m above account for the fact that the pumping light is neither parallel, nor 100% circularly polarized. Daniels and Timsit (Dan71a) developed expressions to estimate these constants and they obtained for the light sources used in this work

$$R_{-1} = 0.0015, \quad R_0 = 0.0640 \quad \text{and} \quad R_{+1} = 0.9345. \quad (\text{II.5})$$

In the case of an ideal source these constants are respectively 0, 0, and 1. Such a situation could be better achieved by utilizing a laser.

Timsit and Daniels (Tim71a) compared the results of Eq. (II.1) with their experimental observations and found a level of agreement that was not completely satisfactory. In the following, suggestions are made to extend Eq. (II.1).

Firstly the product $QI_m(P)$ in Eq. (II.1a) and (II.1b) stands for the absorption rate per unit volume and should be interpreted

$$QI_m(P) = I'_S n \sigma_o I_m(P), \quad (\text{II.6})$$

where

$$I'_S = \text{photon flux from the source (in } m^{-2}s^{-1} \text{), and}$$

σ_o = photoabsorption cross section (in m^2).

This assumes that the photon flux is a constant throughout the cell volume. However this is an absorption process, so the flux decreases exponentially when it passes through the total length of the cell (Che82). The absorption rate per unit volume should therefore be described using

$$\frac{I_s}{V_c} [1 - e^{-n\sigma_o LI_m(P)}], \quad (II.7)$$

where

I_s = total photon production rate (in s^{-1}),

V_c = gas cell volume (in m^3), and

L = average photon path length (in m) e.g. about $2R$ for a sphere.

The deviation of Eq. (II.7) from Eq. (II.6) becomes significant when $n\sigma_o L$ is more than 0.1. Using Eq. (II.7) to replace $QI_m(P)$ in the expression for the polarization rate [Eq. (II.1)] gives

$$\frac{dP}{dt} = \frac{2I_s}{NV_c} \sum_{m=-1}^{+1} R_m [1 - e^{-n\sigma_o LI_m(P)}] \left(m + w \frac{m - 2P}{1 - \frac{m}{2}} - r_o \frac{11}{6} \frac{1 + P^2/11}{1 + P^2/3} \right) - P \left(\frac{1}{\tau} + \frac{1}{\tau} \frac{n}{N} \frac{11}{3} \frac{1 + P^2/11}{1 + P^2/3} \right). \quad (II.8)$$

Furthermore, collision-induced mixing of the 2^3P -state not only affects the net angular momentum transfer rate, T_m , but also the reabsorption factor, r_o , as will be explained below. The magnitude of collision mixing is introduced with the factor u . Expressed in terms of

the collision time, τ_c , and the radiative decay time, τ_e , this is given by

$$u = \frac{\tau_e}{\tau_e + \tau_c} \quad (\text{II.9})$$

The decay time was found to be $\tau_e = 105$ ns (Lif65) and the collision time at 300 K is calculated from the relative velocity of ^3He atoms, 2060 ms^{-1} , and the cross section for scattering out of the 2^3P_0 -state and into the 2^3P_1 and 2^3P_2 states, $(68 \pm 3)10^{-20} \text{ m}^2$ (Sch67). In the calculation of u , the cross section is multiplied by 18/16 to get the total cross section for scattering from any 2^3P -state leading to a random distribution over all 2^3P -states.

$$u = \frac{N}{N + 6.0 \cdot 10^{21}} = \frac{p}{p + 25} = \frac{p'}{p' + 0.19} \quad (\text{II.10})$$

where p = pressure in Pa, and p' = pressure in Torr. Eq. (II.10) shows that for the commonly employed pressures of over 100 Pa (1 Torr) more than 80% of the excited atoms undergo collision mixing (i.e. $u > 0.8$).

Timsit and Daniels (Tim71a) estimated that the reabsorption factor, r_0 , would be about 0.1, because the relative absorption of pumping light in the cell was measured to be of that order. This assumes that the reemitted photons only excite the 2^3S_1 - 2^3P_0 transition, which is valid as long as the excited atom remains unperturbed. As shown above, this is unlikely. Therefore all the spectral lines will be present. The most intense line among these has a significantly higher absorption probability, resulting in a reabsorption factor that could be an order

of magnitude higher than expected without collision mixing. This effect is therefore more significant than previously understood. In Appendix B a series of equations are derived that are used here to estimate r_o as a function of the collision mixing probability. The full relation cannot easily be given in closed form, but the first approximation (Appendix B) is

$$r_o = a_n (0.75 + 5.98 u) \quad (\text{II.11})$$

where $a_n = n\sigma_o R$, the absorption factor, and $R =$ cell radius. The absorption factor is of the order of 10^{-2} depending on geometry, level of weak discharge and pressure.

Qualitatively the above process can explain why even with increasing pumping light intensity still no full polarization of the system can be achieved. Using a laser as light source gave an upper limit of 0.70 at 40 Pa (0.3 Torr, Nac82).

Not only is reabsorption associated with pumping light absorption, but it also occurs in the presence of a discharge, because excited atoms are continuously formed and photons are emitted in the decay. All interactions of these photons with ^3He atoms cause depolarization. An important contribution to this could be the trapping of UV-radiation caused by the decay of singlet P-states to the ground state (Fig. 2.3a). The emitted photons are easily absorbed by the relatively high density of the ground-state atoms. Several tens of interactions occur, until the absorption of the photon is followed by a decay to the singlet metastable state rather than the ground state (Fig. 2.2). It is

recommended that the magnitude of this effect be appraised. So far no report has been found in the literature relating depolarization to photon trapping of singlet P-state decay.

Intrinsically all discharge-related depolarization processes add to Eq. (II.1) a term proportional to the discharge intensity. As has been noted before (Tim71a) such processes are accounted for by an appropriate choice of the metastable relaxation time in Eq. (II.1d).

To conclude this section the polarization rate equation is derived for the case of small values of polarization. This is relevant here, because most observed polarizations are less than 0.25. The Taylor expansion up to the first order in P of the right-hand side of Eq. (II.8) gives

$$\begin{aligned} \frac{dP}{dt} &= \frac{2I_s}{NV_c} (1 - e^{-n\sigma_o L}) (1 + w) \sum_{m=-1}^{+1} mR_m \\ &- P \frac{2I_s}{NV_c} (1 - e^{-n\sigma_o L}) \sum_{m=-1}^{+1} R_m \left[\frac{\frac{5}{2} m^2 n\sigma_o L (w+1)}{e^{n\sigma_o L} - 1} + w(2 - \frac{1}{2} m^2) + \frac{11}{6} r_o \right] \\ &- P \left(\frac{1}{\tau} + \frac{1}{\tau} \frac{n}{N} \frac{11}{3} \right) \end{aligned} \quad (II.12)$$

Compare this with the differential equation of a first order system

$$\frac{dP}{dt} = \frac{P_o - P}{T_p} \quad (II.13)$$

where P_o is the equilibrium polarization and T_p is the pumping time. So

from Eqs. (II.12) and (II.13) it follows that

$$\frac{P_o}{T_p} = \frac{2I_s}{NV_c} (1 - e^{-n\sigma_o L}) (1 + w) \sum_{m=-1}^{+1} mR_m \quad (\text{II.14})$$

$$\frac{1}{T_p} = \frac{1}{\tau'} + \frac{1}{\tau} \frac{n}{N} \frac{11}{3} + \frac{2I_s}{NV_c} (1 - e^{-n\sigma_o L}) \times \sum_{m=-1}^{+1} R_m \left(\frac{\frac{5}{2} n^2 \sigma_o L (1 + w)}{e^{n\sigma_o L} - 1} + w \left(2 - \frac{1}{2} m^2 \right) + \frac{11}{6} r_o \right) \quad (\text{II.15})$$

and dividing Eq. (II.15) by Eq. (II.14) the saturation polarization is

found

$$\frac{1}{P_o} = \frac{\sum_{m=-1}^{+1} R_m \left(\frac{\frac{5}{2} n^2 \sigma_o L (1 + w)}{e^{n\sigma_o L} - 1} + w \left(2 - \frac{1}{2} m^2 \right) + \frac{11}{6} r_o \right)}{(1 + w) \sum_{m=-1}^{+1} mR_m} + \frac{NV_c}{2I_s} \frac{\frac{1}{\tau'} + \frac{1}{\tau} \frac{n}{N} \frac{11}{3}}{(1 - e^{-n\sigma_o L}) (1 + w) \sum_{m=-1}^{+1} mR_m} \quad (\text{II.16})$$

The limiting value of P for I_s approaching large values is called here the extrapolated polarization, P_e , which can be determined experimentally by plotting $1/P$ against $1/I_s$. Such a graph exhibits a straight line dependence as is implied by Eq. (II.16) and has also been found elsewhere (Bec75). However, this is not the maximum obtainable polarization, because at higher polarizations the approximation by Eq. (II.12) is not sufficient.

For a spherical cell it is estimated that $L=2R$ and therefore $n\sigma_0 L=2a_n$. Substitution of this in Eq. (II.16) and the estimation of r_0 (Appendix B) the extrapolated polarization can be calculated as a function of u and a_n (Fig. 2.5).

D. Target Cell

With the cooperation of the University of Toronto specially designed cells (Fig. 2.6) were made to reduce the background proton scattering from the walls of the glass cell (see Sec. III.B). In these cells the proton beam enters through a thin window fused to an extension. The outer perimeter in the equatorial plane of the cell was etched to the lowest possible thickness of 0.2 to 0.3 mm to reduce energy loss and straggling of protons scattered from the ^3He nuclei. Similar designs had been used before, but all with exit windows for the proton beam (Bak69, War75) or even exit windows on extensions for the scattered protons (Mul78, Sza78b). In this work the proton energies are higher than previously used. Consequently, the effect of double scattering from glass becomes relatively less significant.

Corning No. 1720 was used as material for the glass cells for two reasons. Firstly, the permeation at room temperature of helium through this glass is five orders of magnitude lower than for standard Pyrex (Corning, data sheets) and secondly, the ground-state relaxation time due to helium atom collisions with the container wall is superior to all other glass types (Tim71b). The disadvantage is that its high softening point and low thermal shock resistance make it a difficult glass to

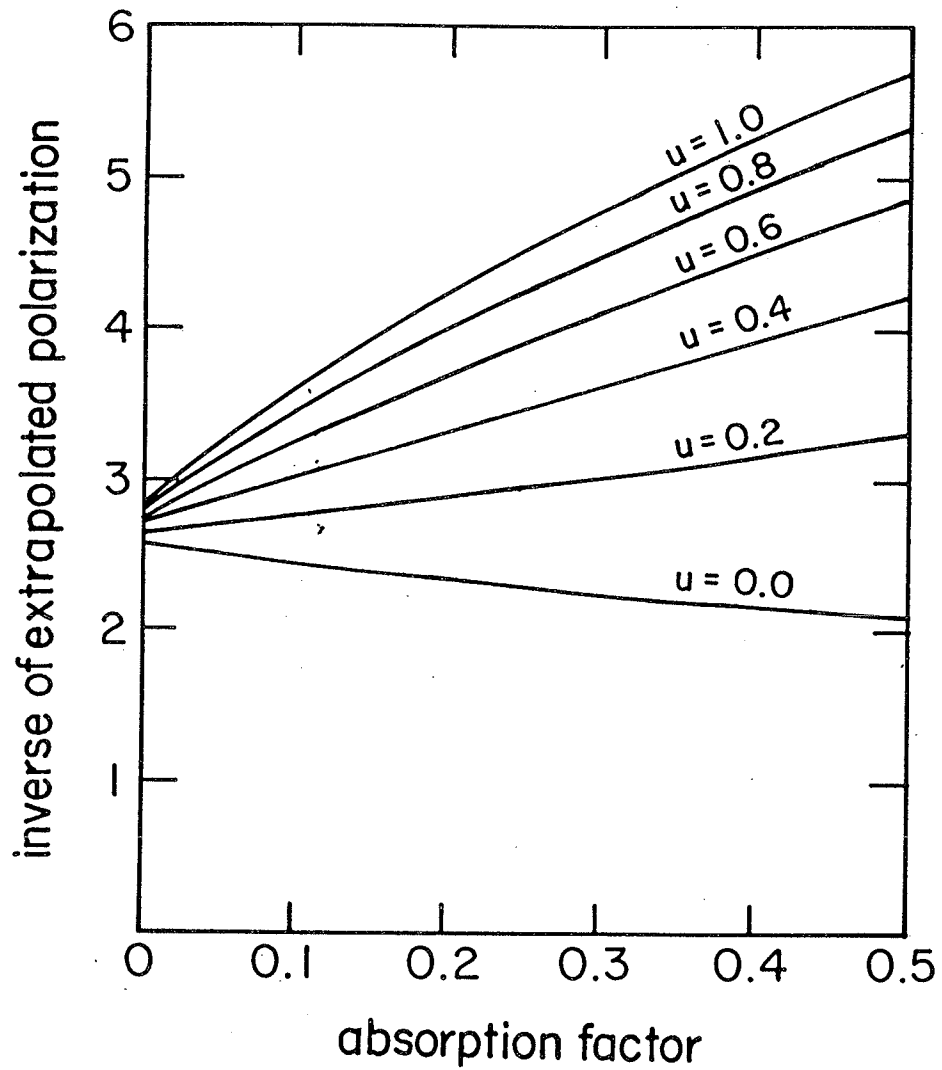


FIG. 2.5 Inverse of the extrapolated polarization as a function of the absorption factor, $a_n = n\sigma R$, for various values of the collision mixing probability, u .

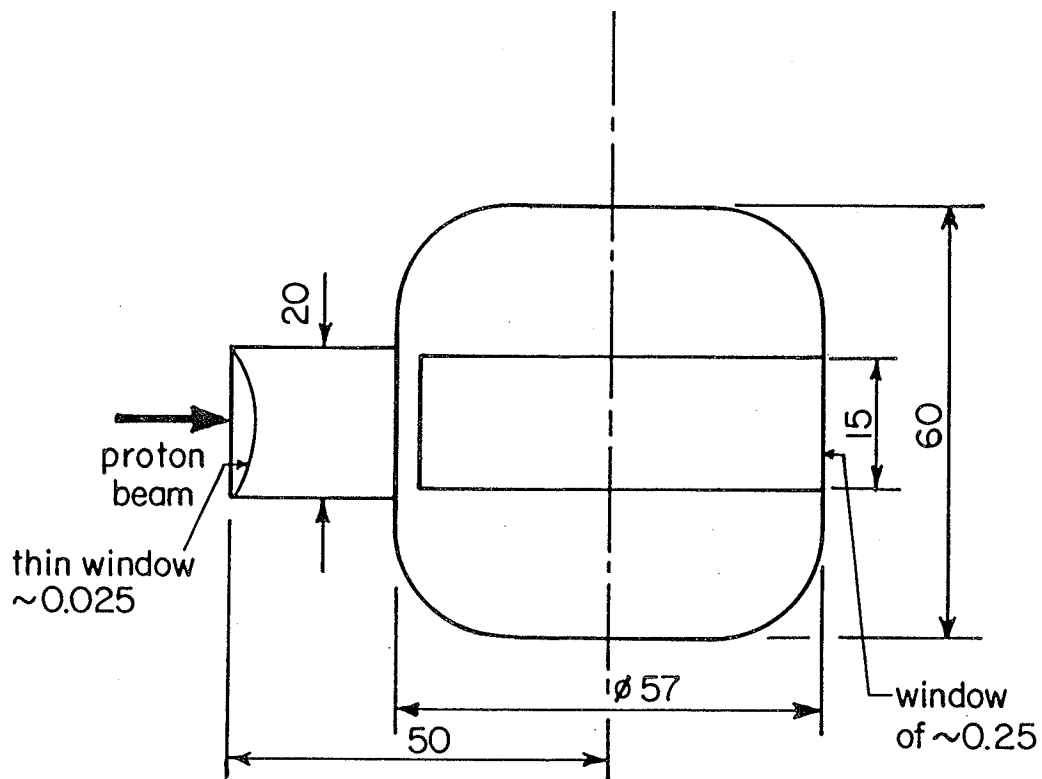


FIG. 2.6 Target cell (all dimensions in mm).

handle. Because of this, for example, for the thin window on the extension a special technique had to be developed (Hil72).

To ensure decontamination of the cells, they were cleaned with dilute hydrofluoric acid, distilled water and acetone. This was followed by a bakeout period of five days at 280°C after which the cells were filled with ^3He through a quartz diffusion cell (Tim70).

The ^3He pressure affects both the polarization and the count rates in a nuclear scattering experiment. These, in turn, influence the error of the analyzing powers. In order to find the optimal pressure, an analysis was made whereby the duration of the experiment was calculated with the following input data: a) the analyzing powers to be determined at angle intervals of 10° from 30° to 150° and energy intervals of 5 MeV from 20 MeV to 45 MeV, b) an error in the analyzing powers of 0.025, c) an error in the polarization measurement of 0.005, d) the background count rates estimated from experiments with empty cells (Sec. III.B), e) the anticipated beam currents at the various energies, and f) the pressure dependence of the polarization as given by Timsit and Daniels (Tim71a). This analysis (Fig. 2.7) for the target cell of Fig. 2.6 shows that the required duration of the experiment as a function of the cell pressure (Fig. 2.7) has a minimum at 0.21 kPa (1.6 Torr) with a range of 0.15 to 0.45 kPa (1.1 to 3.4 Torr), when an increase in running time of 30% is considered acceptable.

Incidentally, the cell on which most nuclear scattering experiments were done had a pressure of 647 Pa (4.85 Torr) and a typical polarization of around 0.11. This can be compared with other polarized

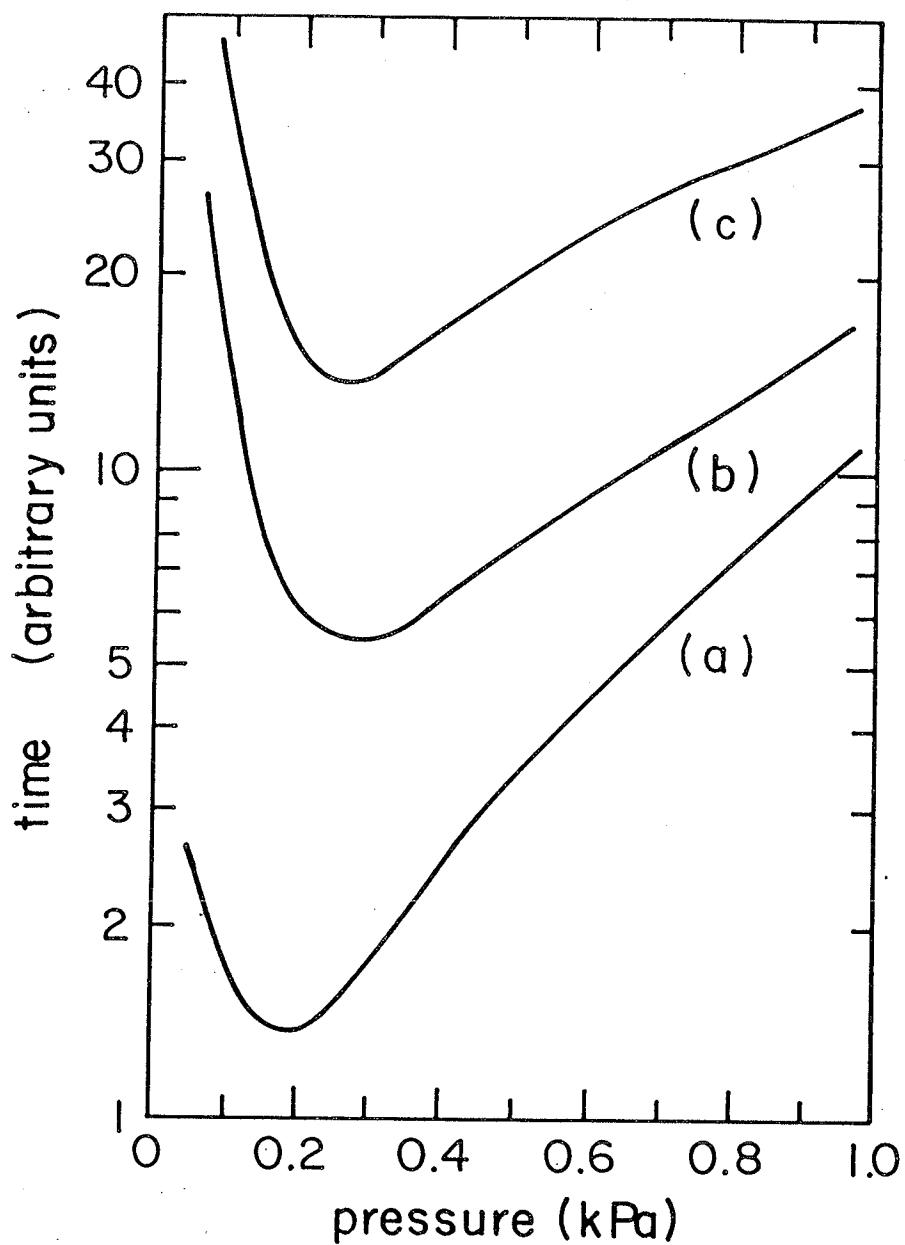


FIG. 2.7 Expected duration of the scattering experiment as a function of the cell pressure for (a) a cell without background proton scattering, (b) the cell of Fig. 2.6, and (c) a spherical cell.

^3He -targets by using as criterion the product P^2p , where p is the cell pressure (Table 2.2).

Finally, most cells had a limited lifetime when they were put in the scattering chamber and exposed to a proton beam. The probable cause of this was narrowed down to the occurrence of leakage on the seal between the thin window on the extension and the extension tube (Fig. 2.6). This was confirmed with cells made of laboratory Pyrex, Corning No. 7740. The University of Manitoba glass workshop was able to make Pyrex seals, that could withstand proton beam exposures with a drastically improved success rate. These cells could be made with an entrance window of 0.03 mm thickness, and a window on the perimeter of 0.15 mm thickness. However, only cells made of Corning No. 1720 were used in the experiments reported here.

E. Instrumentation

Fig. 2.8 illustrates the experimental layout which is similar to the setup developed by the Toronto group (Tim71a). The Helmholtz coils give a uniform magnetic field to provide an orientation axis for the atoms. One ^4He -lamp above and one below the target cell, supply circularly polarized light with opposite handedness. Metastable atoms are produced by the 1 MHz oscillator. The remainder of the system measures the polarization by observing the fluorescent light with a photodiode before and after depolarization. A set of coils are included that can introduce an inhomogeneous magnetic field effectively to quench the polarization. Only the photodiode, the weak discharge electrodes

Table 2.2. Values for P^2_p and methods of polarization measurement for different polarized ^3He targets.

Reference	Pressure (kPa)	Polarization	P^2_p (Pa)	Measurement method
Bak69	0.53	0.093	5	absorption
McS69	0.53	0.105	6	absorption
Bak71	0.53	0.15	12	absorption
Roh71	0.53	0.22	26	beam transmittance
Tim71a	0.20	0.16	5	various methods
Bec74	0.60	0.10	6	absorption
War75	0.53	0.165	14	fluorescence
Mul78	0.27	0.18	9	absorption and beam transmittance
Sza78	0.53	0.22	26	beam transmittance
Nac82	0.4	0.38	58	circular polarization of 668 nm line
this work	0.647	0.13	11	fluorescence

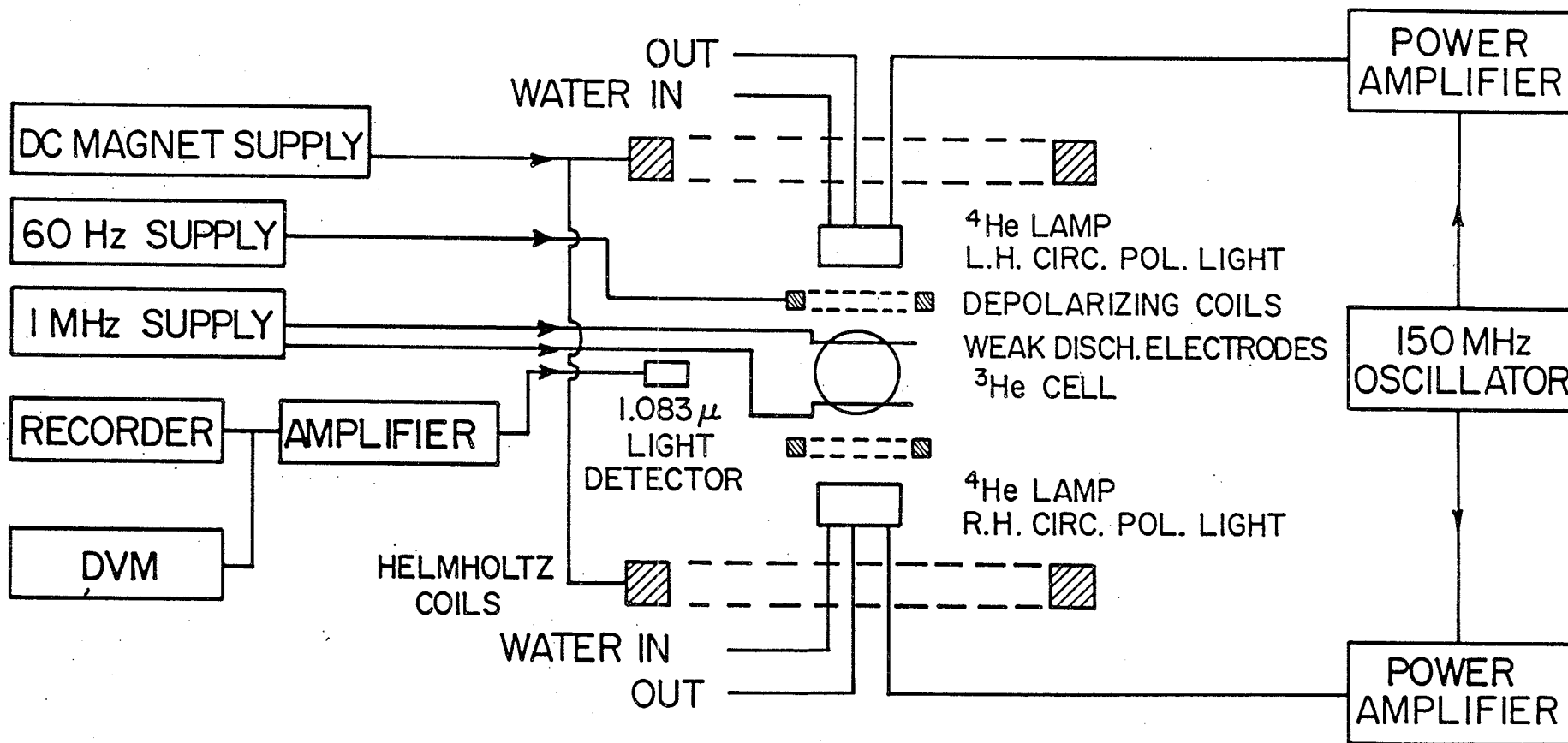


FIG. 2.8 Experimental layout of the apparatus for polarization and its measurement.

and the depolarizing coils are inside the scattering chamber.

At the cell position the magnetic field is 4.2 mT produced by Helmholtz coils of 0.3 m radius. The field gradients are such that no noticeable depolarization is caused. This was confirmed by comparison of the polarization measurements for two cells on a setup of the Toronto group as well as on the present setup.

The weak discharge intensity was adjusted for each cell such that the maximum polarization was obtained. Normally this was slightly above the lowest sustainable discharge intensity, but below the ignition voltage. The choice of frequency, 1 MHz, is discussed by Timsit (Tim70) and experimental data on this are given by Beckmann et al. (Bec74).

The pumping light sources were built by the Toronto group (Dan71c). Each consists of a water cooled discharge tube with a collector lens and a Fresnel lens. The latter part has a polaroid and a quarter-wave plate sandwiched between the two halves of the lens. To change from left-handed to right-handed circularly polarized light or vice versa, the whole Fresnel lens assembly was exchanged. The essential parameters of the lamps are: ^4He pressure = 0.4 to 0.55 kPa, RF frequency = 150 MHz, operating power = 500 to 600 W and the maximum photon intensity at 1083 nm = $1.4 \cdot 10^{17} \text{ s}^{-1}$. Our experience has shown that after approximately one week the power output of the lamp diminishes because of electrode sputtering. The demise of a lamp is preceded by a period of intermittent flickering which can be reduced temporarily by driving the lamp at higher power levels.

The ageing of the lamps also increases the amount of stray electromagnetic radiation that can be picked up by the surface barrier detectors located in the scattering chamber. In this situation, the outputs of these detectors carry the difference frequency between the top and the bottom lamp when either one of the lamps begins to deteriorate. Replacing the two RF lamp supplies by power amplifiers driven from one master oscillator effectively quenched the effect. This also improved the stability of the pumping light and the fluorescence signal. When only one lamp is in service, the other lamp can be replaced by a mirror (Bec77), which reflects 20% of the incident light in the present configuration.

F. Polarization Measurement

In order to measure the polarization during a nuclear scattering experiment most experimental groups have used one of the optical techniques originally developed by Colegrove et al. (Col63) and modified by Greenhow (Gre64). In the present work the fluorescence signal from the pumping light absorption is observed. This was chosen because of its reliability (Dan71b) and the possibility of using two pumping light sources thereby increasing the maximum obtainable polarization.

Most commonly the pumping time for the polarization is on the order of minutes, so that the equilibrium polarization is reached after ten to fifteen minutes, which corresponds to a minimum in the fluorescence signal (Fig. 2.9). A measurement cycle consists of observation of the fluorescence signal before and immediately after a depolarization

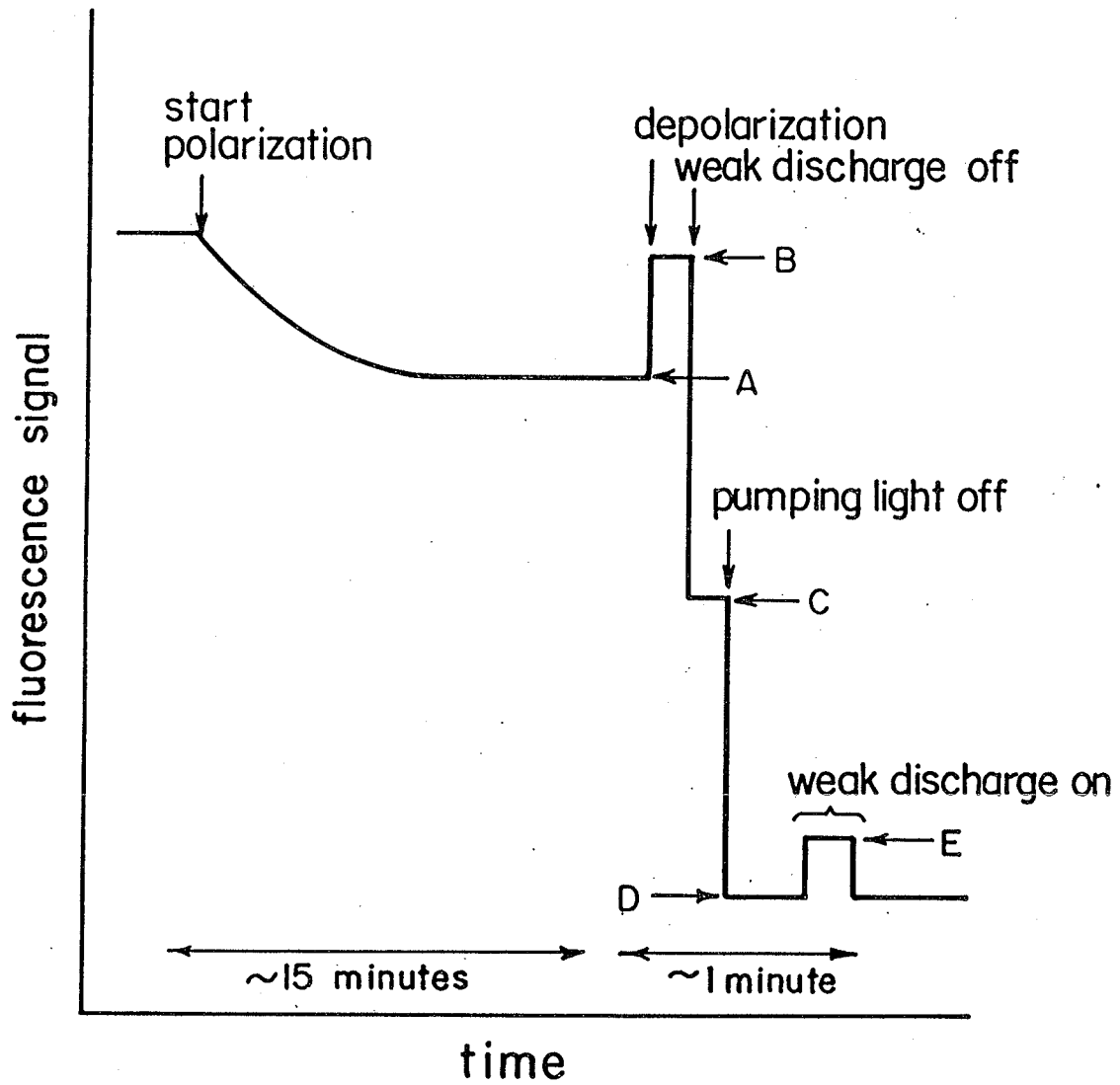


FIG. 2.9 Sketch of the fluorescence signal during a measurement cycle.

(Fig. 2.9). Assuming that the fluorescence from pumping light absorption is proportional to the absorption rate per atom as in Eq. (II.6), the relative change in fluorescence is related to the polarization by

$$\frac{S_{AB}}{S_{BC} - S_{DE}} = \frac{S_{abs}(0) - S_{abs}(P)}{S_{abs}(0)} = \sum_{m=-1}^{+1} R_m (1 - I_m(P)) \quad (II.17)$$

where

S = the observed signal in arbitrary units, with A to E the various stages in the measurement cycle (Fig. 2.9), and

S_{abs} = fluorescence from pumping light absorption, i.e. the signal S corrected for the discharge fluorescence S_{DE} .

The polarization dependence of this ratio is calculated from Eqs. (II.3) and (II.5), and is approximately equal to $2.33P$.

The fluorescence from only the weak discharge, S_{DE} (Fig. 2.9), is used as a correction in Eq. (II.17). In addition, it can be considered as a measure for the discharge intensity. This is utilized to illustrate the dependence of the polarization on this discharge intensity (Fig. 2.10). For each cell such a curve was determined to get the optimal polarization.

A measure of the pumping light strength is obtained from the magnitude of the stray light reflected from the glass, S_{CD} (Fig. 2.9). The dependence of the polarization on the pumping light intensity (Fig. 2.11) shows the linear relationship between $1/P$ and $1/I_S$ as derived from Eq. (II.16). From the extrapolated polarization an estimate can be made for the absorption factor [Eq. (II.16)]. It was

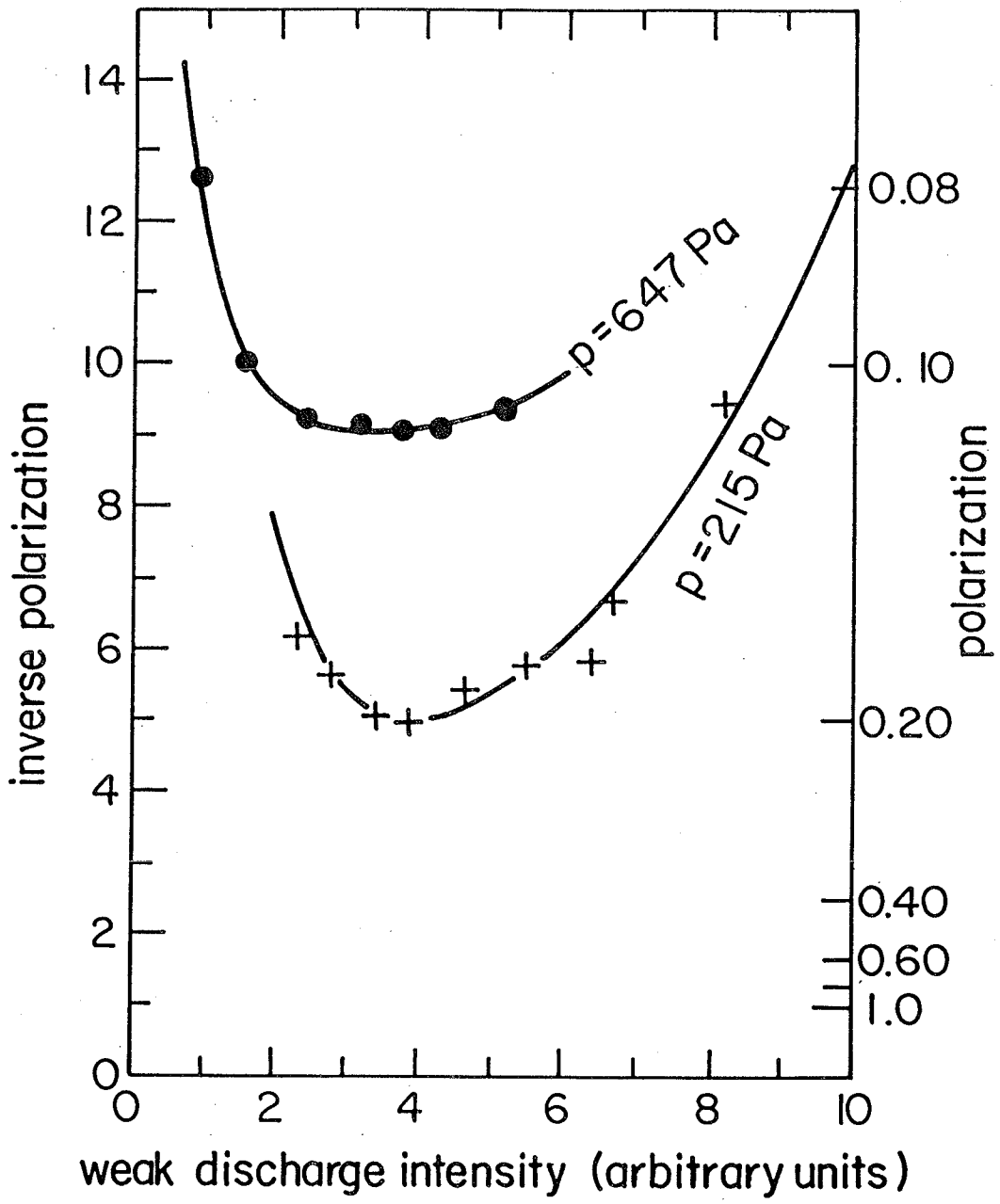


FIG. 2.10 Weak discharge intensity dependence of the polarization.

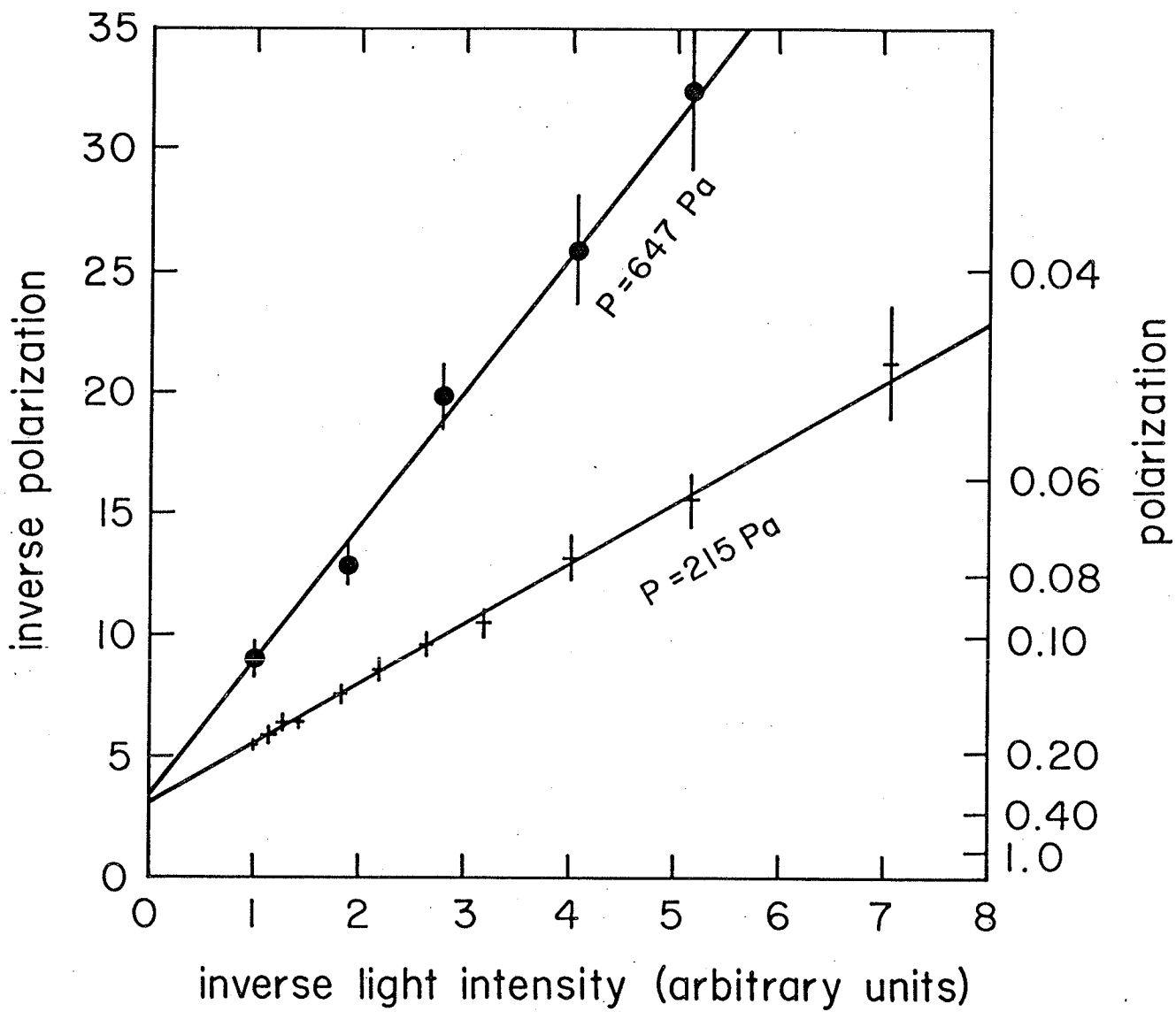


FIG. 2.11 Pumping light intensity dependence of the polarization.

found to be $a_n = 0.024 \pm 0.012$ and 0.05 ± 0.04 at the optimal weak discharge intensity for cells with respectively 215 Pa (1.61 Torr) and 647 Pa (4.85 Torr).

During nuclear scattering experiments the polarization is determined before and after each two-hour measurement period (Sec. III.C), and the average of the two is calculated. This is considered as the average polarization for the complete period. Comparison of repeated polarization measurements gave an estimate for the total measurement error, which was found to be 0.004. This is mainly attributed to discharge instabilities. Variations in the pumping light intensity and the reading error only accounted for a contribution of 0.002 to the error mentioned above.

It is possible to monitor the polarization continuously by a temporary polarization inversion rather than a depolarization. This is achieved by inverting the handedness of the pumping light (Bec77) or an adiabatic reversal of the magnetic field (Bak69). Attempts have been made to apply these methods to the present setup, but it was found that the measurement reliability would decrease unless the scattering chamber were to undergo major design changes. An alternative solution is the use of a separate measurement beam (Hub69, Pin74, Dan71b). Work is being carried out on this solution at present. A last possibility is the observation with a polarimeter of other lines in the spectrum of helium. This is based on the idea that the excited states are formed with a net orientation, and therefore are emitting photons along the magnetic field with a net circular polarization (Pav70). However, this method has to be calibrated with conventional optical techniques.

To conclude this section, several sources of systematic error will be investigated. The basis of all optical techniques is that an equilibrium exists between the spin system of the ground state and the spin system of the metastable state. Direct measurements of the ground state polarization have confirmed this using NMR techniques (Col63, Gam65, Gan73, Tim76) and through ^4He - ^3He nuclear scattering at an angle and energy where the analyzing power approaches unity (Phi62, Bak69, McS70, War75). Another direct measurement could be the detection of the external magnetic field caused by the magnetic dipoles of the ^3He atoms (Coh69).

The actual calculation of the polarization from Eq. (II.17) assumes that the fluorescence signal from the reemitted photons is proportional to the absorption rate per atom, i.e.

$$S_{\text{abs}}(P) \sim n\sigma \sum_{m=-1}^{+1} R_m I_m(P) I_s \quad (\text{II.18})$$

Firstly, it relies on a good estimate of the geometrical factors R_m , which describe the deviation of the pumping light from an ideal source of 100% circularly polarized light. This has been the subject of various estimations (Lee71, Bak69, Dan71a). Daniels and Timsit (Dan71b) have shown that their calculated values of R_m [Eq. (II.5)] give polarizations that compare well with those obtained with a separate, nearly ideal measurement beam. It is estimated from Timsit (Tim70, Table V) that the inaccuracy of this comparison is equivalent to a relative error of 0.03 in the polarization.

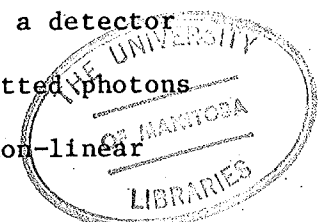
Secondly, Eq. (II.18) implies that the metastable atom density, n , does not depend on the polarization. But this is not the case for the electron density, where there is a reduction of electron production by triplet-triplet collisions (Sch70). Therefore, the triplet metastable atom density should also be affected. There are no reports that it is a significant effect. Finally, Eq. (II.18) should actually account for the exponential decrease of the light intensity as the beam passes through the cell (Che82). In the case that the detector only views a small volume at the center of the cell, Eq. (II.18) should be replaced by

$$\begin{aligned}
 S_{\text{abs}}(P) &\sim n\sigma_o \sum_{m=-1}^{+1} R_m I_m(P) I_s e^{-n\sigma_o R I_m(P)} \\
 &\sim a_n \sum_{m=-1}^{+1} R_m I_m(P) I_s e^{-a_n I_m(P)} \quad (\text{II.19})
 \end{aligned}$$

When the absorption is directly observed or the fluorescence is seen as an average over the complete cell, Eq. (II.18) becomes

$$\begin{aligned}
 S_{\text{abs}}(P) &\sim \sum_{m=-1}^{+1} R_m I_s [1 - e^{-n\sigma_o L I_m(P)}] \\
 &= \sum_{m=-1}^{+1} R_m I_s [1 - e^{-2a_n I_m(P)}] \quad (\text{II.20})
 \end{aligned}$$

The actual relationship should be more complicated, because a detector samples a finite element of the cell and secondly the reemitted photons undergo reabsorptions. However, both equations predict a non-linear



behaviour of $S_{\text{abs}}(0)$ with respect to the metastable atom density, which is confirmed especially for the higher pressure cell (Fig. 2.12).

By substitution of Eqs. (II.19) or (II.20) for $S_{\text{abs}}(P)$ in Eq. (II.17), another polarization dependence is obtained. Both approaches lead to polarizations that differ by no more than 0.0005 from each other and that are a factor

$$1 + a_n(1 - 1.6P) \quad \text{for } a_n < 0.20 \quad (\text{II.21})$$

larger than the polarization obtained conventionally [Eqs. (II.17) and (II.18)]. For the cell of 647 Pa (4.85 Torr) often used in this work, this factor is equal to 1.04 ± 0.04 at the optimal weak discharge intensity [Note, that all polarizations quoted in this thesis have been calculated according to Eqs. (II.17) and (II.18), so that they remain comparable to other data. However, the effect mentioned above has been taken into account in the interpretation of the extrapolated polarization, Eq. (II.16), and in the data reduction for the analyzing power determination (Sec. IV.B)].

The systematic error in the polarization is therefore mainly dependent on the uncertainties in the geometrical factors, R_m , and the uncertainty in a_n . Together they add to a normalization error of 0.05 in the polarization. A considerable improvement can be achieved by using earlier mentioned alternative measurement methods, and by an independent determination of the absorption factor.

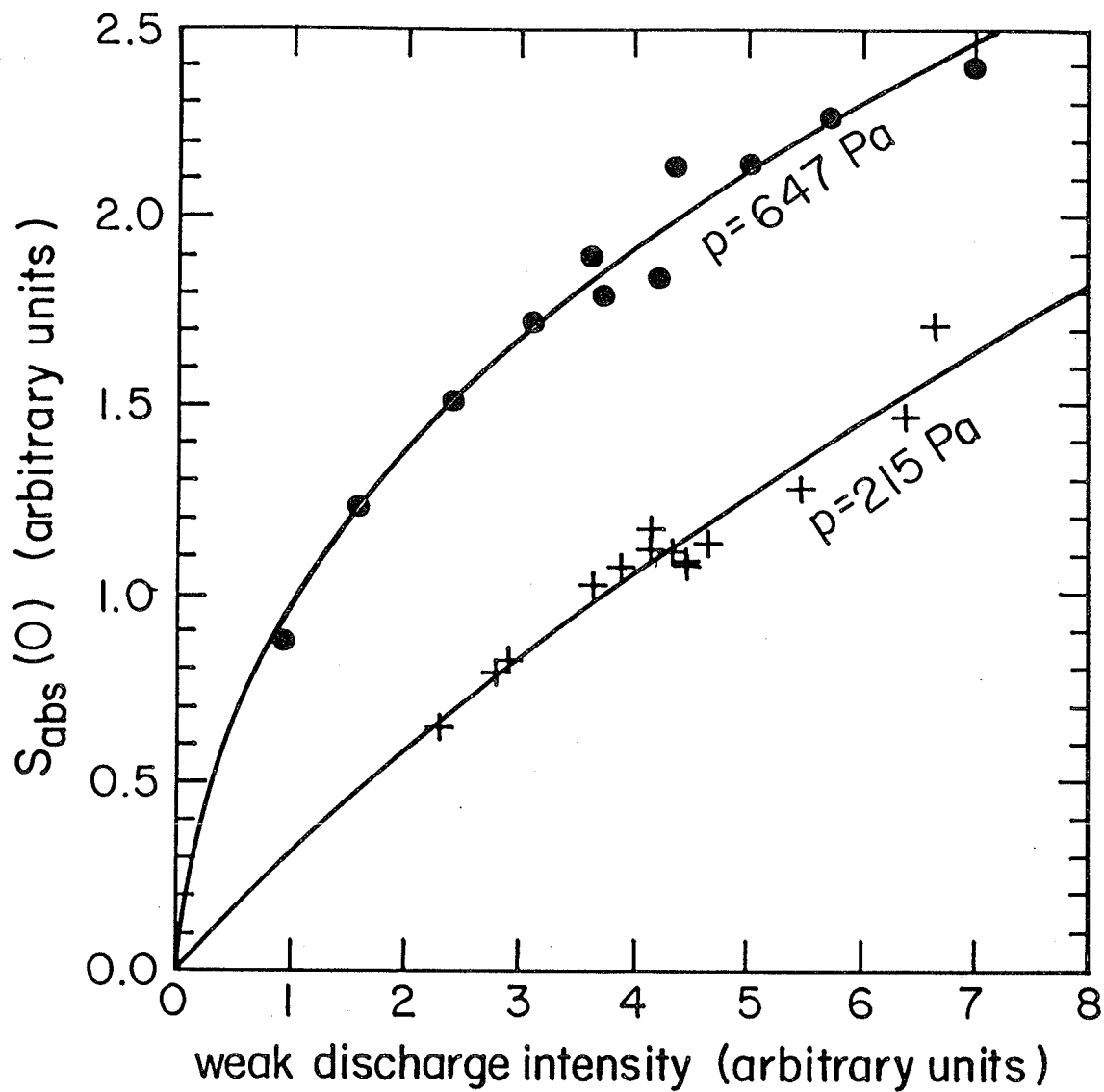


FIG. 2.12 Fluorescence signal at zero polarization as a function of the weak discharge intensity.

III. NUCLEAR SCATTERING EXPERIMENT

A. Instrumentation

The proton beam was extracted from the University of Manitoba Cyclotron and momentum analyzed by a switching magnet that deflected the beam by 30° (Fig. 3.1). A quadrupole magnet, Q4 in Fig. 3.1, focussed the beam onto image slits of dimensions 2.5 mm by 5 mm (width and height). Beam transport calculations and experimental beam tuning gave a quadrupole magnet current I_{Q4} of

$$I_{Q4} = \sqrt{E_p} (8.219 \pm 0.013), \quad (\text{III.1})$$

where E_p is the proton energy (in MeV). Subsequently, a quadrupole magnet doublet, Q5 and Q6 in Fig. 3.1, focussed the beam at the target position to a size of 4 mm by 10 mm (width and height), which was regularly inspected during a measurement cycle with a scintillator screen inserted in front of the target cell. The proton energy was variable from 20 to 48 MeV, and had an energy spread on the order of 0.2 MeV. The beam currents at the target were normally more than 50 nA and no more than 100 nA to limit count rates in the detectors.

Beam transport calculations had been performed prior to the reconstruction of this beam line. It was designed in such a way that it could also be utilized for polarized protons, in which case the scattering chamber could be moved upstream, and another quadrupole magnet doublet and a polarimeter could be placed between the chamber and

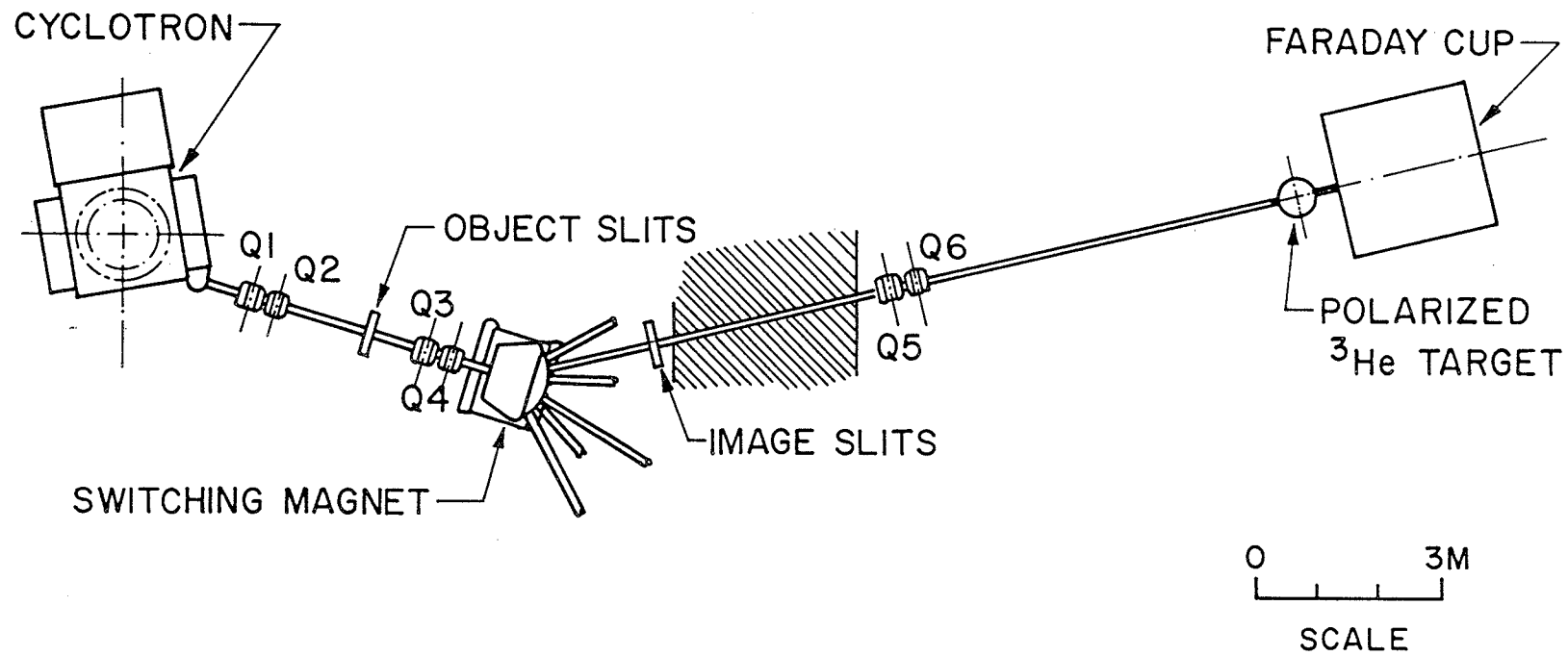


FIG. 3.1 Beamline configuration.

the Faraday cup. Fig. 3.1 illustrates the configuration as used in this work with unpolarized protons.

All elements of the scattering chamber (Fig. 3.2) were constructed of nonmagnetic materials such as aluminium. This minimized any magnetic field gradients at the target, as these might cause noticeable depolarization (Sec. II.C). The chamber had two aperture defining systems, which were independently rotatable and mounted on the lids of the chamber. The scattered protons were simultaneously detected at four angles each separated by 10° on either side of the beam. The slits had a width of 4.8 mm and a height of 12.7 mm. The front slits were made of thin tantalum to reduce slit edge scattering. Two sets of slits are available. One set of 2 mm thickness stops protons up to 35 MeV and one set of 3 mm thickness stops protons up to 45 MeV. The solid angle defining slits at the rear were made of brass. They were located 187 mm or 168 mm behind the front slits when one or two surface barrier detectors, respectively, were used. The angular resolution of the slit system is 2.0° , which should be added to the dispersion of the main beam (0.3°) and multiple scattering in the glass cell windows (0.5° to 4.3° depending on proton energy and scattering angle). The total angular resolution is therefore in the range of 2.1° to 4.7° .

The chamber was designed to detect scattered protons in a range of angles from 15° to 165° . This was made possible with a 19 mm wide slot on the outer ring of the chamber covered with 0.13 mm thick kapton. However, due to the size of the etched windows on the cell (Fig. 2.6) it was only feasible to measure from 30° to 150° .

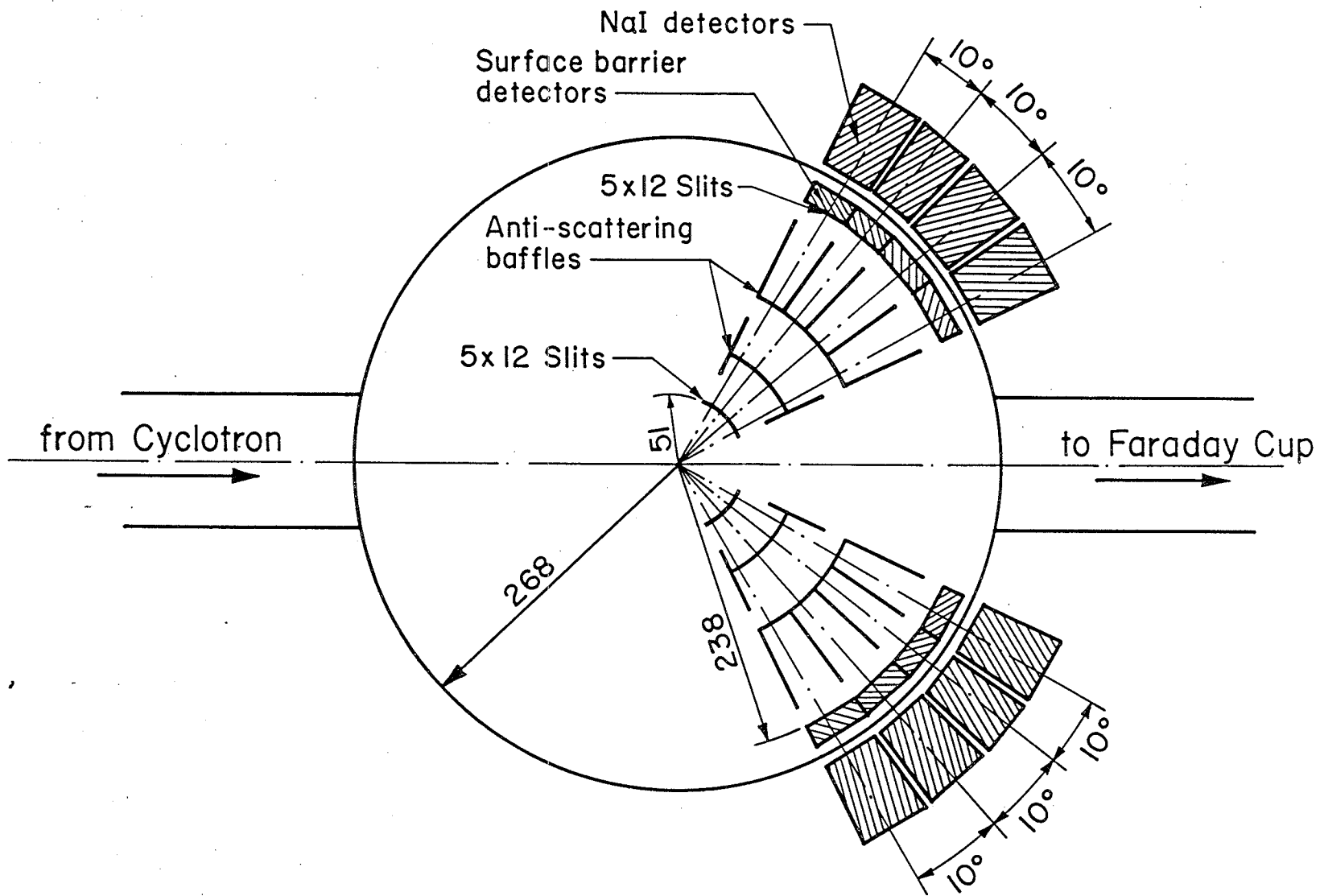


FIG. 3.2 Scattering chamber (dimensions in mm).

At forward angles (less than 90°) ΔE -E telescopes were used. These consisted of a surface barrier detector (typically 200 mm^2 in area, 0.2 mm thick) inside the chamber and a NaI-detector (38 mm diameter, 13 mm thick) outside the chamber (Fig. 3.2). Telescopes with two surface barrier detectors had to be employed at the back angles (greater than 90°), because the protons were considerably less energetic due to the kinematics of proton scattering from ^3He and due to increased energy loss in the glass cell windows at the lower proton energies. In that case the ΔE and E-detectors were respectively 200 mm^2 by 0.1 mm and 200 mm^2 by 1 mm.

The signals from the two detectors of one telescope were amplified and only those events with coincident signals were added and presented at the input of an ADC (Figs. 3.3 and 3.4). The ADC started the signal conversion when a strobe pulse was given, which was derived from the logic signal representing a coincidence at any telescope. A PDP-15 computer accumulated the coincidence spectra from the eight telescopes. The dead time correction was found by comparing the total number of counts in a coincidence spectrum with the actual number of coincidences presented to the ADC, separately recorded by a scaler for each telescope (Fig. 3.3).

Two monitoring NaI-detectors with small apertures detected the protons scattered from the rear window of the glass cell at an angle of 20° . In this way beam movement was monitored and corrected, if necessary. An automated beam location system (Pet72) is being constructed to use the output from these monitors in order to correct beam movement with a computer controlled steering magnet. For

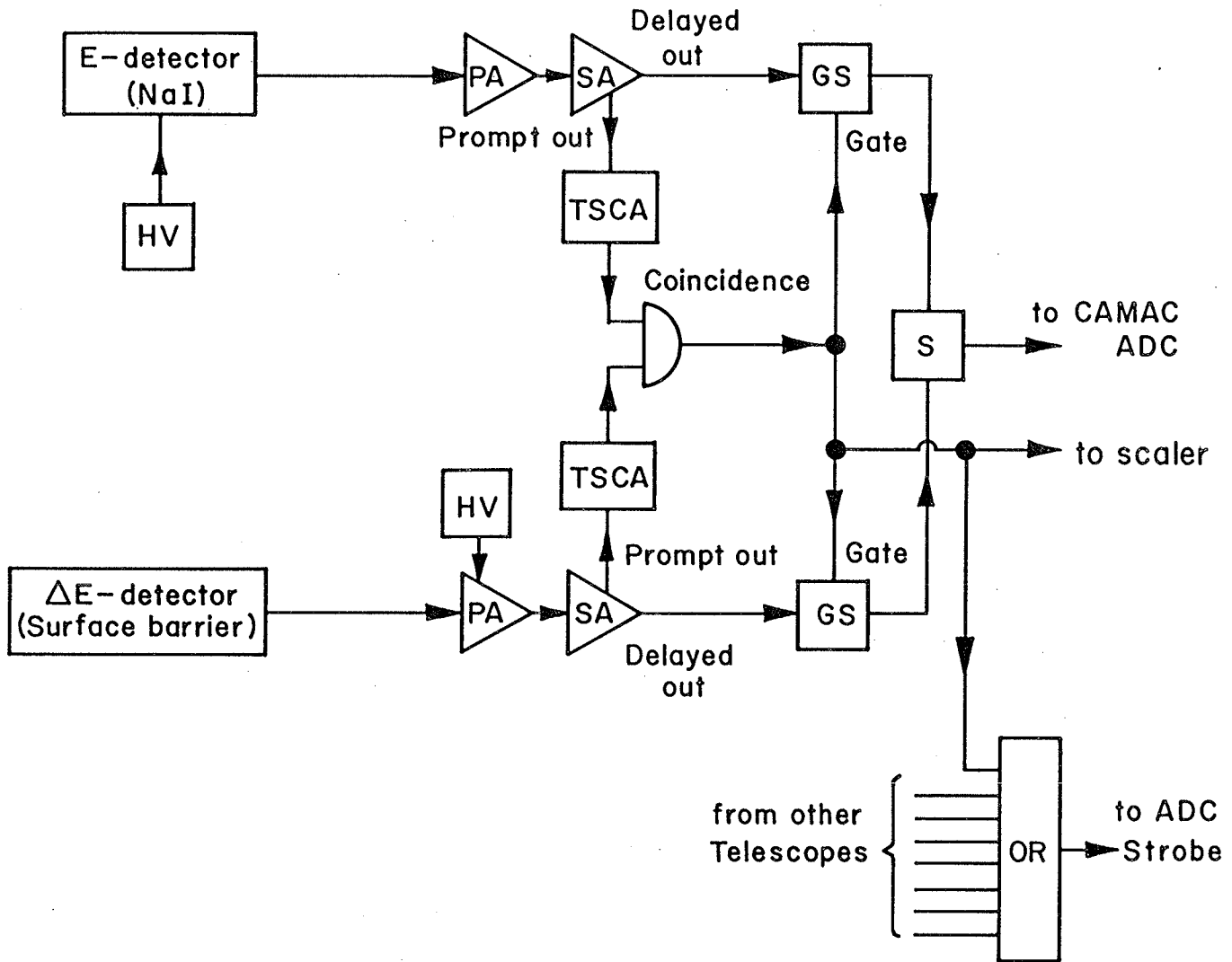


FIG. 3.3 Blockdiagram of the electronics for one telescope (PA = preamplifier, SA= spectroscopy amplifier, TSCA = timing single channel analyzer, HV = high voltage supply, C = coincidence unit, GS = gate and pulse stretcher, S = signal summation).

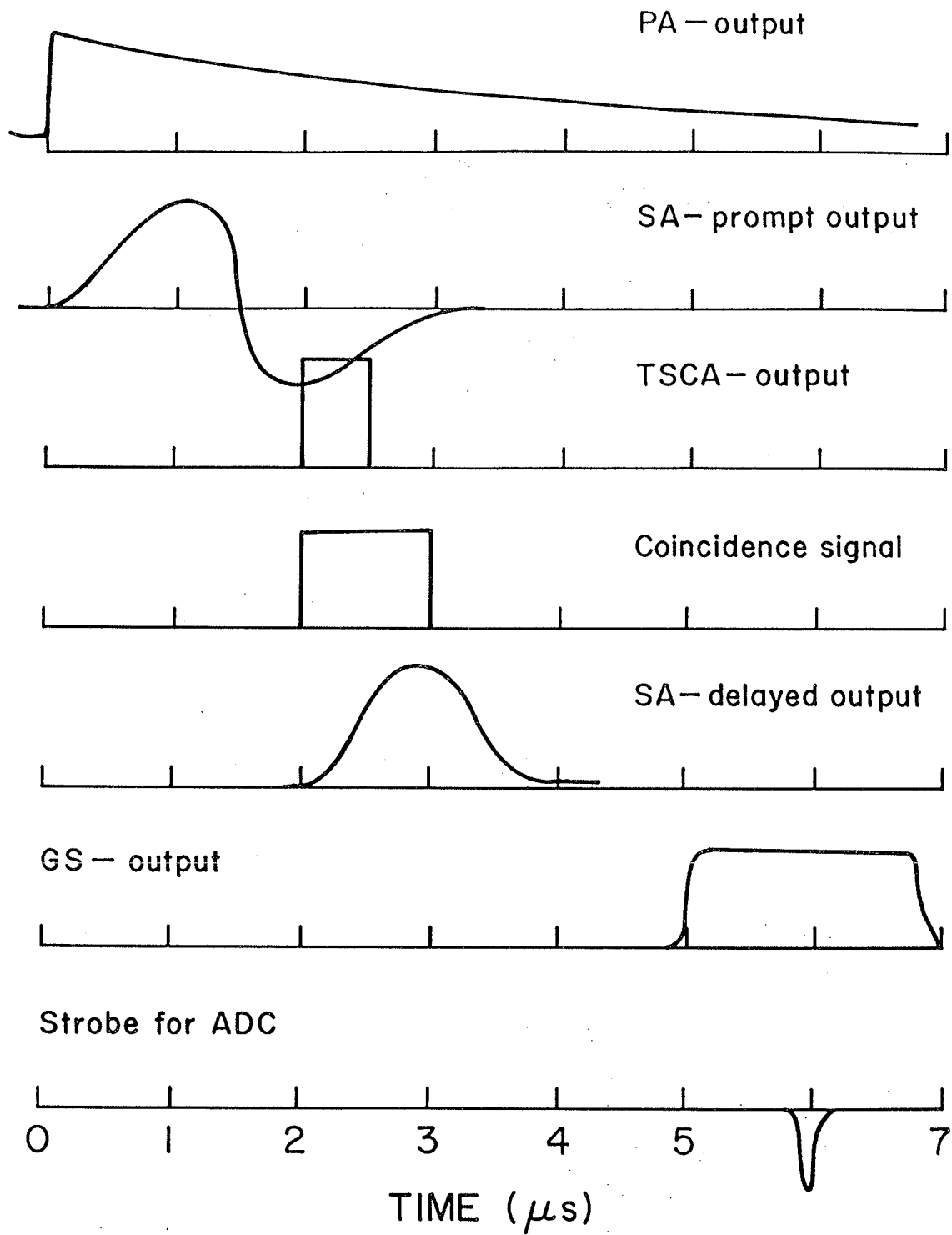


FIG. 3.4 Timing diagram.

normalization purposes, beam current was collected with a Faraday cup and integrated using a current integrator and digitizer.

B. Preparatory Experiments.

The energy of the proton beam was determined by the magnetic field strength of the switching magnet (Fig. 3.1). A measure for the field strength is the frequency, f , of an NMR-probe in this magnet that is related to the kinetic energy, E_p (in MeV), by

$$f = \frac{6.514 \sqrt{E_p (1876.5118 + E_p)}}{4.2577 \text{ G}}, \quad (\text{III.2})$$

where G is a constant. Because the beamline was reconstructed for this experiment, a recalibration of the constant G was needed. A cross-over technique (Smy64) was used whereby protons were scattered from a CD_2 foil at various proton energies. For each calibration energy, angles were found at which the peak for inelastic proton scattering from carbon coincides with the peak of the elastic scattering from deuterium. At each energy the cross-over angle was determined for two excited states. From these, two estimates of the energy were derived, and with Eq. (III.2) and the NMR frequency, the constant G was calculated (Table 3.1). The average of the constant is $G=63.823$ (± 0.12 %). With Eq. (III.2) the energies can then be determined with an accuracy of 0.24%.

Table 3.1. Data obtained for the calibration of the bending magnet with the cross-over technique using a CD₂-target.

Est. energy (MeV)	Exc. state	Cross-over angle (degrees)	Energy (MeV)	Average energy (MeV)	NMR (MHz)	G	New energy estimate (MeV)
22.7	no 1	41.881±0.066	22.788±0.061	22.788±0.061	4.9183	63.897±0.086	22.74±0.05
	no 2	73.05 ±0.62	21.56 ±0.22				
26.2	no 1	38.600±0.086	26.21 ±0.10	26.214±0.077	5.3561	63.794±0.095	26.24±0.06
	no 2	62.76 ±0.20	26.22 ±0.12				
31.0	no 1	34.905±0.071	31.28 ±0.11	31.170±0.081	5.8387	63.896±0.085	31.10±0.07
	no 2	55.79 ±0.14	31.04 ±0.12				
35.8	no 1	32.330±0.081	35.86 ±0.16	35.752±0.078	6.2751	63.749±0.071	35.83±0.09
	no 2	50.889±0.081	35.719±0.089				
43.0	no 1	29.284±0.081	42.89 ±0.22	43.07 ±0.15	6.8950	63.80 ±0.11	43.10±0.10
	no 2	45.18 ±0.13	43.21 ±0.20				
Average:					63.823±0.078		
(uncertainty includes systematic error in angle)							

Before the actual experimental runs were made, the setup was tested with empty target cells, whereby the background spectra were recorded. Initial trials with spherical cells showed that protons could be doubly scattered firstly from the cell wall at the beam entry point, secondly from the slits or the glass in front of the detectors, and subsequently enter the detector telescopes. The counting rates were such that peak-to-background ratios of 1:5 could be expected. Because of this, the cell design of Fig. 2.6 was developed, whereby the primary scattering point (the beam entry point) is made as thin as possible and put on an extension. Using this design, the background is reduced by 70% to 90% depending on energy and angle. The result was a peak-to-background ratio of 1:1 to 16:1 (Fig. 3.5).

C. False Asymmetries and Measurement Procedure

From the experimental results, asymmetries are calculated with the formula

$$\epsilon = \frac{Y_L - Y_R}{Y_L + Y_R}, \quad (\text{III.3})$$

where Y_L and Y_R are respectively the left and right detector yields. To a first approximation, the yield for a gas target is given by (Si159)

$$\frac{n_b NA_r w_f}{h R_r} \frac{\sigma(\theta, \psi)}{\sin(\theta)}, \quad (\text{III.4})$$

where

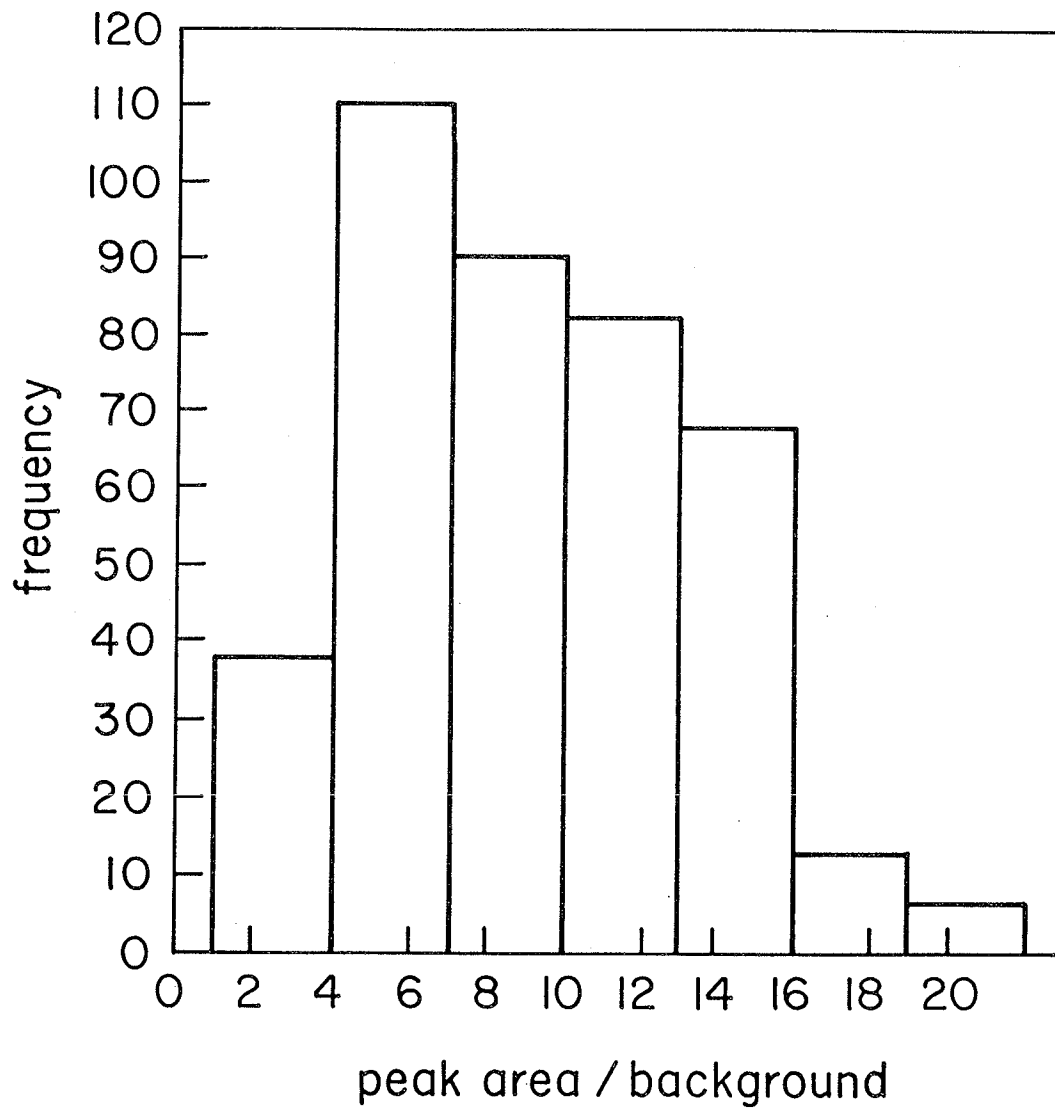


FIG. 3.5 Peak-to-background ratios for measurements taken at 30 and 32.5 MeV at the forward angles.

n_b = number of particles in the beam,

N = target density (in m^{-3}),

A_r = area of rear aperture (in m^2),

w_f = width of front aperture (in m),

h = distance from the front of the first slit to the back of the second slit (in m),

R_r = distance from the target center to the rear aperture (in m),

σ = differential cross section (in m^2),

Θ = scattering angle, and

ψ = azimuthal angle.

Asymmetries are introduced when any of the geometry parameters or the scattering angle in Eq. (III.4) differ for the left and right detectors in addition to any azimuthal dependence of the differential cross section.

For the present experiment, instrumental asymmetries are due to: a) uncertainties in the slit dimensions and aperture distances (Table 3.2), b) possible misalignment of the front and rear aperture for each scattering channel (less than 0.01°), c) inaccuracies in the angle read out for left and right aperture system (less than 0.1°), d) difference in rotation axis position of the left and right aperture system (about 0.5 mm apart), and e) beam position variation, which in future will be controlled by an automatic beam positioning system. After accounting for the aperture dimensions of Table 3.2 there still remained an instrumental asymmetry, as calculated with Eq. (IV.15), of around 0.04 at most angles and energies.

Table 3.2. Aperture dimensions and their contribution to the instrumental asymmetry (applies to the present measurements at forward angles, and $E \leq 35$ MeV).

Angle		Front aperture width height (mm) (mm)	Rear aperture width height (mm) (mm)	Front-rear distance (mm)	Asymmetry
first	Left	5.080 12.783	4.840 12.783	186.02	+0.0386
	Right	4.742 12.765	4.803 12.765	185.90	
+10	Left	4.734 12.747	4.747 12.747	185.62	-0.0014
	Right	4.736 12.751	4.757 12.751	185.63	
+20	Left	4.740 12.758	4.740 12.758	185.64	+0.0001
	Right	4.732 12.747	4.754 12.747	185.76	
+30	Left	4.736 12.753	4.744 12.753	185.57	-0.0035
	Right	4.732 12.748	4.792 12.748	185.91	
Error:		± 0.007 ± 0.010	± 0.005 ± 0.006	± 0.05	± 0.0013

Furthermore, an asymmetry is introduced because the protons are traversing a magnetic field, which changes the scattering angle by a small amount $\Delta\theta$. The change of angle was estimated knowing the momentum of the particle before and after scattering, and knowing the magnetic field configuration. Typically, it is on the order of 0.15° at 30 MeV, but it has to be calculated separately for each energy and scattering angle. From Eqs. (III.3) and (III.4) it is derived that its effect on the asymmetry is

$$\varepsilon_m = \frac{-\Delta\theta}{Y} \frac{dY}{d\theta} = \Delta\theta \left[\cot(\theta) - \frac{1}{\sigma} \frac{d\sigma}{d\theta} \right], \quad (\text{III.5})$$

where ε_m has the correct sign for the magnetic field pointing upwards and for $\Delta\theta$ positive. Estimates for ε_m from the above equation and the experimental determinations (see Sec. IV) are on the order of 0.01 and agree with each other within 30%.

Consequently, the instrumental and magnetic field induced asymmetries give a total asymmetry of 0.05, which should be compared with an asymmetry $\varepsilon_n = 0.04$ due to the nuclear scattering process at a maximum analyzing power of 0.4 and a typical target polarization of 0.1. The observed asymmetry, Eq. (III.3), consists approximately of the sum $\varepsilon_i \pm \varepsilon_m \pm \varepsilon_n$, where the signs depend on whether the magnetic field is up or down and the polarization is up or down.

In order to separate ε_n from the other asymmetries, the experiment cycle consisted of four runs with: a) B up, P up, b) B up, P down, c) B down, P down, and d) B down and P up. Each run lasted about two hours and a total cycle takes nine to ten hours. The length of time taken was a result of weighing long-term stability characteristics of the proton beam

and the target polarization, against the fraction of down time introduced by the necessity to measure the polarization after each run and to repolarize the target.

The above mentioned sequence of combinations of magnetic field, B, and polarization, P, was followed, because between runs a) and b), and between runs c) and d) only the polarization is changed, so that the count rate at the same detector can be compared at two pairs of sequential runs, where only the nuclear asymmetry changes sign. At the end of each run all spectra were stored on magnetic tape, and the left-right asymmetries together with their errors were determined using a subroutine especially written and incorporated to the data acquisition program. A measurement cycle at each angle was repeated as many times as was necessary to achieve an accuracy on the order of ± 0.03 in the analyzing power (ϵ_n/P).

IV. DATA PROCESSING

A. Procedure

The following stages of data analysis can be identified:

- 1) Each spectrum was inspected individually; two regions, one on each side of the elastic scattering peak, were selected for the determination of the background. All data relevant for the subsequent analysis were stored with the spectra, so that later stages could be done without operator interference.
- 2) Peak areas were calculated, corrected for dead time and normalized with respect to the integrated beam current.
- 3) Yields at one angle from left and right detectors in four consecutive runs, i.e. 8 peak areas, were taken together to obtain the analyzing power, magnetic field related asymmetry and instrumental asymmetry.
- 4) The results at a certain angle of all cycles were combined and a weighted average was calculated for the analyzing power.

In this section the details of the above procedure will be discussed. Tests for internal consistency are described in the next section. It should be noted that asymmetries of a few percent only are to be determined.

In the first stages the background was obtained from two regions around the peak (Fig. 4.1). The choice of regions required careful judgement. A comparison between the analyzing powers as obtained by two observers interpreting the same cycle, gave differences in the order of

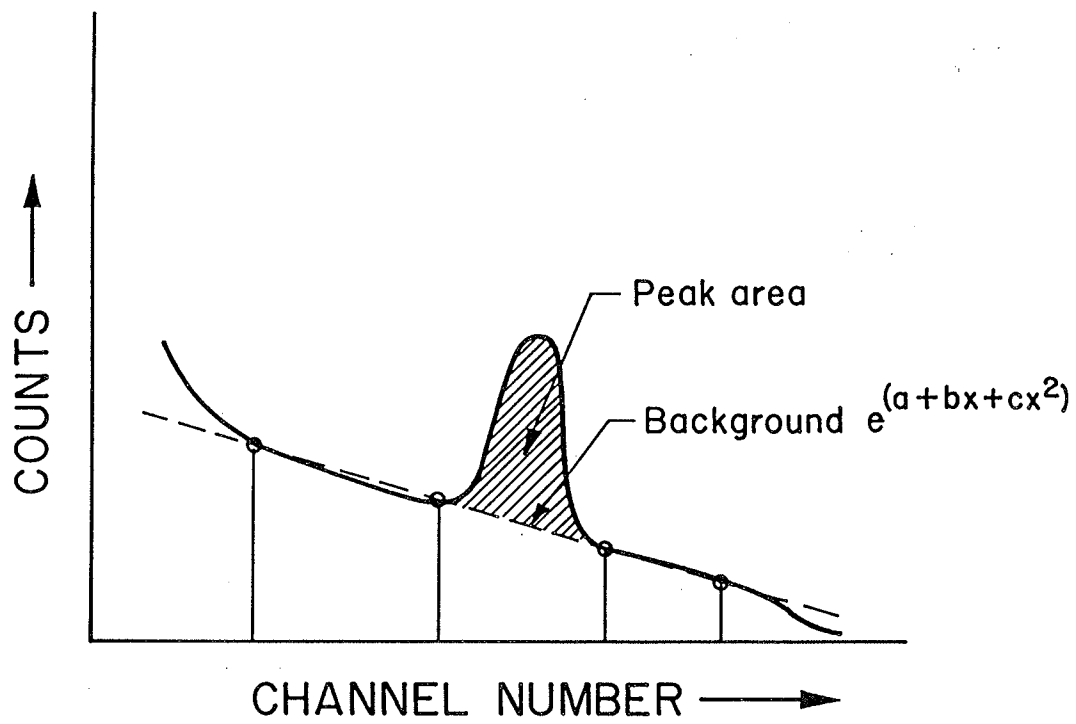


FIG. 4.1 Spectrum illustrating the method of defining the background and determining the peak area.

0.15 times the error evaluated from counting statistics. This is within acceptable limits.

The functional form of the background in all cases was chosen to be a second order polynomial fitted to the logarithm of the channel counts. This proved to give the lowest chi-square value in trials where polynomials of different order were fitted to the channel counts or to the logarithm of the channel counts. Only a straight line fit to the logarithm of the channel counts occasionally gave a better chi-square fit.

The background was fitted simultaneously to two spectra, taken with the same detector telescope in consecutive runs which had opposite target polarization but the same magnetic field. Under these circumstances the background should be essentially the same. This is confirmed by the chi-square criterion for the fitting procedure which was independent of whether one or two spectra were included in the fitting procedure (Fig. 4.2). The advantage of this approach is that it minimizes the effect of a possible systematic error due to the approximation of the background by a simple mathematical function.

The peak areas were obtained by summation of all channel counts in the region between the two inner channels defining the peak and correcting this summation for the background (Fig. 4.1). Also the statistical error was evaluated and the dead time correction applied.

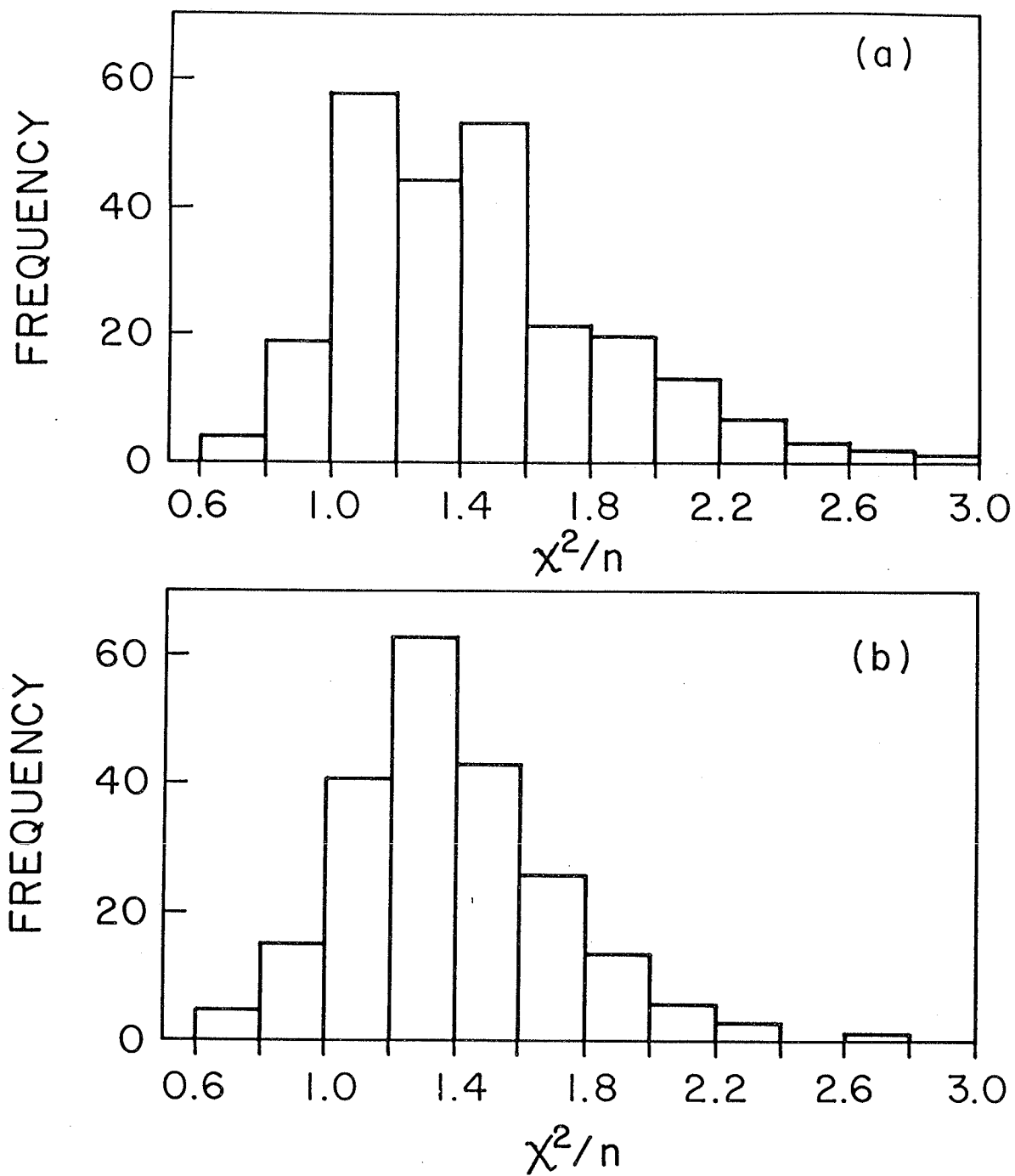


FIG. 4.2 Histogram of the reduced chi-square value (chi-square per degree of freedom) calculated from the background fit to (a) one spectrum each time, and (b) two spectra simultaneously.

At one angle a total of 8 peak areas were deduced from one cycle of four runs as described in Sec. III.C. Table 4.1 represents these in a general formulation derived from Eq. (III.4) as also used by Szaloky (Sza75). The magnetic field related asymmetry is given by a shift in angle, $\Delta\theta$, and the instrumental asymmetry is included by the use of different geometry factors and angles for the left and right detectors. By taking pairs of these yields together four estimates of the analyzing power are found:

$$A_y(\theta_L + \Delta\theta) = \frac{Y_1/n_a - Y_2/n_b}{P_b Y_1/n_a + P_a Y_2/n_b} \quad (\text{IV.1})$$

$$A_y(\theta_L - \Delta\theta) = \frac{Y_4/n_d - Y_3/n_c}{P_c Y_4/n_d + P_d Y_3/n_c} \quad (\text{IV.2})$$

$$A_y(\theta_R - \Delta\theta) = \frac{Y_6/n_b - Y_5/n_a}{P_a Y_6/n_b + P_b Y_5/n_a} \quad (\text{IV.3})$$

$$A_y(\theta_R + \Delta\theta) = \frac{Y_7/n_c - Y_8/n_d}{P_d Y_7/n_c + P_c Y_8/n_d} \quad (\text{IV.4})$$

The simple average of the first pair and last pair of Eqs. (IV.1)-(IV.4) gives the analyzing power at the angles θ_L and θ_R :

$$A_y(\theta_L) = [A_y(\theta_L + \Delta\theta) + A_y(\theta_L - \Delta\theta)] / 2 \pm \sigma_L \quad (\text{IV.5})$$

Table 4.1. Formulas defining the yields in the determination of nuclear scattering asymmetries [see Eq. (III.4) for explanation of the symbols].

Run	spin	magn. field	yield
Left detector			
a	up	up	$Y_1 = n_a N G_L(\theta_L + \Delta\theta) \sigma(\theta_L + \Delta\theta) (1 + P_{a y} A_L(\theta_L + \Delta\theta))$
b	down	up	$Y_2 = n_b N G_L(\theta_L + \Delta\theta) \sigma(\theta_L + \Delta\theta) (1 - P_{b y} A_L(\theta_L + \Delta\theta))$
c	down	down	$Y_3 = n_c N G_L(\theta_L - \Delta\theta) \sigma(\theta_L - \Delta\theta) (1 - P_{c y} A_L(\theta_L - \Delta\theta))$
d	up	down	$Y_4 = n_d N G_L(\theta_L - \Delta\theta) \sigma(\theta_L - \Delta\theta) (1 + P_{d y} A_L(\theta_L - \Delta\theta))$
Right detector			
a	up	up	$Y_5 = n_a N G_R(\theta_R - \Delta\theta) \sigma(\theta_R - \Delta\theta) (1 - P_{a y} A_R(\theta_R - \Delta\theta))$
b	down	up	$Y_6 = n_b N G_R(\theta_R - \Delta\theta) \sigma(\theta_R - \Delta\theta) (1 + P_{b y} A_R(\theta_R - \Delta\theta))$
c	down	down	$Y_7 = n_c N G_R(\theta_R + \Delta\theta) \sigma(\theta_R + \Delta\theta) (1 + P_{c y} A_R(\theta_R + \Delta\theta))$
d	up	down	$Y_8 = n_d N G_R(\theta_R + \Delta\theta) \sigma(\theta_R + \Delta\theta) (1 - P_{d y} A_R(\theta_R + \Delta\theta))$

$$A_y(\theta_R) = [A_y(\theta_R + \Delta\theta) + A_y(\theta_R - \Delta\theta)]/2 \pm \sigma_R \quad (IV.6)$$

where σ_L and σ_R are the error in A_y as derived from the uncertainty in the yields. Eqs. (IV.5) and (IV.6) are no more than interpolations, which cause a negligible error of less than 3×10^{-5} in A_y .

Finally a weighted average of Eqs. (IV.5) and (IV.6) gives

$$A_y(\theta) = [A_y(\theta_L)/\sigma_L^2 + A_y(\theta_R)/\sigma_R^2] / (\frac{1}{\sigma_L^2} + \frac{1}{\sigma_R^2}). \quad (IV.7)$$

The reason for using a weighted average is the possibility that the errors in the peak areas are different for the left and right detectors. The total error in the result of Eq. (IV.7) is composed of the errors in Eqs. (IV.5) and (IV.6), and the effect on Eq. (IV.7) of errors in the four polarizations measured during each cycle. A small contribution to the error, less than 0.001, originates from the inaccuracy in the angles θ_L and θ_R in Eq. (IV.7).

Finally, the finite absorption correction for the polarization [Eq. (II.21)] was included by dividing all analyzing powers with the factor 1.04. This could be done with a single factor because all data reported here were taken with the same cell operating at the optimal discharge level.

In order to find the magnetic field related and instrumental asymmetry a linearization in $\Delta\theta$ of Eq. (III.4) is used. Table 4.1 could be written in terms of ϵ_i , ϵ_m , and PA_y with each formula replaced by

$$Y = nNG_o(1 \pm \epsilon_i)(1 \pm \epsilon_m)(1 \pm PA_y), \quad (\text{IV.8})$$

where the signs are determined by the choice of detector (left or right), the direction of the magnetic field and the direction of the polarization. Knowing the polarization in each run and the analyzing power, the effect of the nuclear asymmetry was removed by calculating

$$Y' \equiv \frac{Y}{nN(1 \pm PA_y)} = G_o(1 \pm \epsilon_i)(1 \pm \epsilon_m), \quad (\text{IV.9})$$

and taking the average derived from each subsequent pair in Table 4.1

$$Y'_{12} = (Y'_1 + Y'_2)/2 = G_o(1 + \epsilon_i)(1 + \epsilon_m) \quad (\text{IV.10})$$

$$Y'_{34} = (Y'_3 + Y'_4)/2 = G_o(1 + \epsilon_i)(1 - \epsilon_m) \quad (\text{IV.11})$$

$$Y'_{56} = (Y'_5 + Y'_6)/2 = G_o(1 - \epsilon_i)(1 - \epsilon_m) \quad (\text{IV.12})$$

$$Y'_{78} = (Y'_7 + Y'_8)/2 = G_o(1 - \epsilon_i)(1 + \epsilon_m). \quad (\text{IV.13})$$

The magnetic and instrumental asymmetry are calculated from Eqs. (IV.10)-(IV.13)

$$\epsilon_m = \frac{Y'_{12} - Y'_{34} - Y'_{56} + Y'_{78}}{Y'_{12} + Y'_{34} + Y'_{56} + Y'_{78}} \quad (\text{IV.14})$$

and

$$\epsilon_1 = \frac{Y'_{12} + Y'_{34} - Y'_{56} - Y'_{78}}{Y'_{12} + Y'_{34} + Y'_{56} + Y'_{78}} \quad (\text{IV.15})$$

Although these asymmetries do not affect the determination of the analyzing powers, they were nevertheless determined in order to compare them with estimated asymmetries [Table 3.2 and Eq. (III.5)].

B. Consistency Tests

The basic criterion for the internal consistency of the measurements from one cycle has been (Bak69, Sza78b) the evaluation of a constant

$$K = \frac{r^{1/4} - 1}{r^{1/4} + 1} \quad (\text{IV.16})$$

where

$$r = \frac{Y_1 Y_3 Y_6 Y_8}{Y_2 Y_4 Y_5 Y_7} \quad (\text{IV.17})$$

It has been shown that when the polarization during the four runs of a cycle is constant ($P_a=P_b=P_c=P_d$) K should be zero (Sza75). The procedure was to evaluate K and its error, ΔK , and, for example, to reject a cycle when K was more than three times its error (Sza78b).

A better understanding of the use of K is obtained when Eq. (IV.16) is worked out by substitution of Eq. (IV.8). All detector and magnetic field dependence is eliminated and, up to the first order in the polarization, the constant K approaches

$$(P_a + P_b - P_c - P_d) A_y / 4 . \quad (IV.18)$$

Therefore K should be considered a measure for the constancy of the polarization during a cycle. For convenience this measure is redefined here by

$$K_p = [K - (P_a + P_b - P_c - P_d) A_y / 4] / \Delta K , \quad (IV.19)$$

which should have approximately a standard normal distribution.

A further measure was developed after Rad et al. (Rad81), who compared the analyzing powers obtained from left and right detectors by evaluating their difference in terms of its error

$$K_i = \frac{A_y(\theta_L) - A_y(\theta_R)}{\sqrt{\sigma_L^2 + \sigma_R^2}} , \quad (IV.20)$$

which is derived from Eqs. (IV.5) and (IV.6). This measure is sensitive to any appreciable effects of instrumental asymmetries on the analyzing power.

Similarly a measure for the influence of magnetic field variations on A_y is obtained by comparing the difference in analyzing power obtained from the runs with magnetic fields up and down

$$K_m = \frac{A_y(+)-A_y(-)}{\sqrt{\sigma_+^2 + \sigma_-^2}}, \quad (\text{IV.21})$$

where $A_y(+)$ is derived from the weighted average of Eqs. (IV.1) and (IV.3), and $A_y(-)$ is derived from Eqs. (IV.2) and (IV.4).

Finally the overall fit of Eq. (IV.8) to the data was tested by evaluating the sum of squares

$$\chi_Y^2 = \sum_{i=1}^8 \left(\frac{Y_{\text{exp},i} - Y_{\text{cal},i}}{\Delta Y_{\text{exp},i}} \right)^2, \quad (\text{IV.22})$$

where Y_{exp} and Y_{cal} are, respectively, the experimental and calculated yield.

Each of the consistency measures defined in Eqs. (IV.19) to (IV.22), test a different aspect of the stability during the experiment. Ideally the magnitude of the K-factors should be less than two and the chi-square value of Eq. (IV.22) should lie within an appropriate confidence interval of a chi-square distribution with four degrees of freedom. Most of the cases where some or all of the criteria could not be fulfilled, could be traced to specific malfunctioning during the experiment, such as beam wandering or detector breakdown. Such measurements were rejected. A few cases were identified in which the peaks in the spectra of two consecutive runs had shifted or the goodness of fit of the background to two spectra simultaneously was significantly

worse than the fits of the background to the spectra separately. Then the peak areas from the latter results were substituted.

With these modifications the final analyzing powers were compiled. The quality of the results can also be judged from the distribution of the consistency measures. After Rad et al. (Rad81) the distribution of K^2 was plotted as obtained from the experimental data. Added to this is the reduced chi-square from Eq. (IV.22). The four histograms should have a chi-square distribution with one (for K_p), two (for K_m and K_i) or four (for χ_y^2) degrees of freedom. A comparison of these expected distributions and the actual distributions shows satisfactory agreement (Fig. 4.3).

C. Results and Error Analysis

A total of 24 measurement cycles of four angles each, were completed and four more measurement cycles have been attempted. Counting each angle separately, the actual number of accepted cycles was 83 out of 112. The data cover angles from 30° to 100° and were taken at energies of 25.0, 30.0, 32.5 and 35.0 MeV (Table 4.2, Figs. 4.4 and 4.5).

The errors quoted in Table 4.2 are compounded from (a) counting statistics, (b) polarization uncertainties, (c) beam current integration errors and (d) the uncertainties in the angle. For example at an energy of 30 MeV and an angle of 60° these components are 0.0269, 0.0022, 0.0005 and < 0.0005 respectively, adding up to a total error of 0.027. Obviously, counting statistics is the determining error. At most other

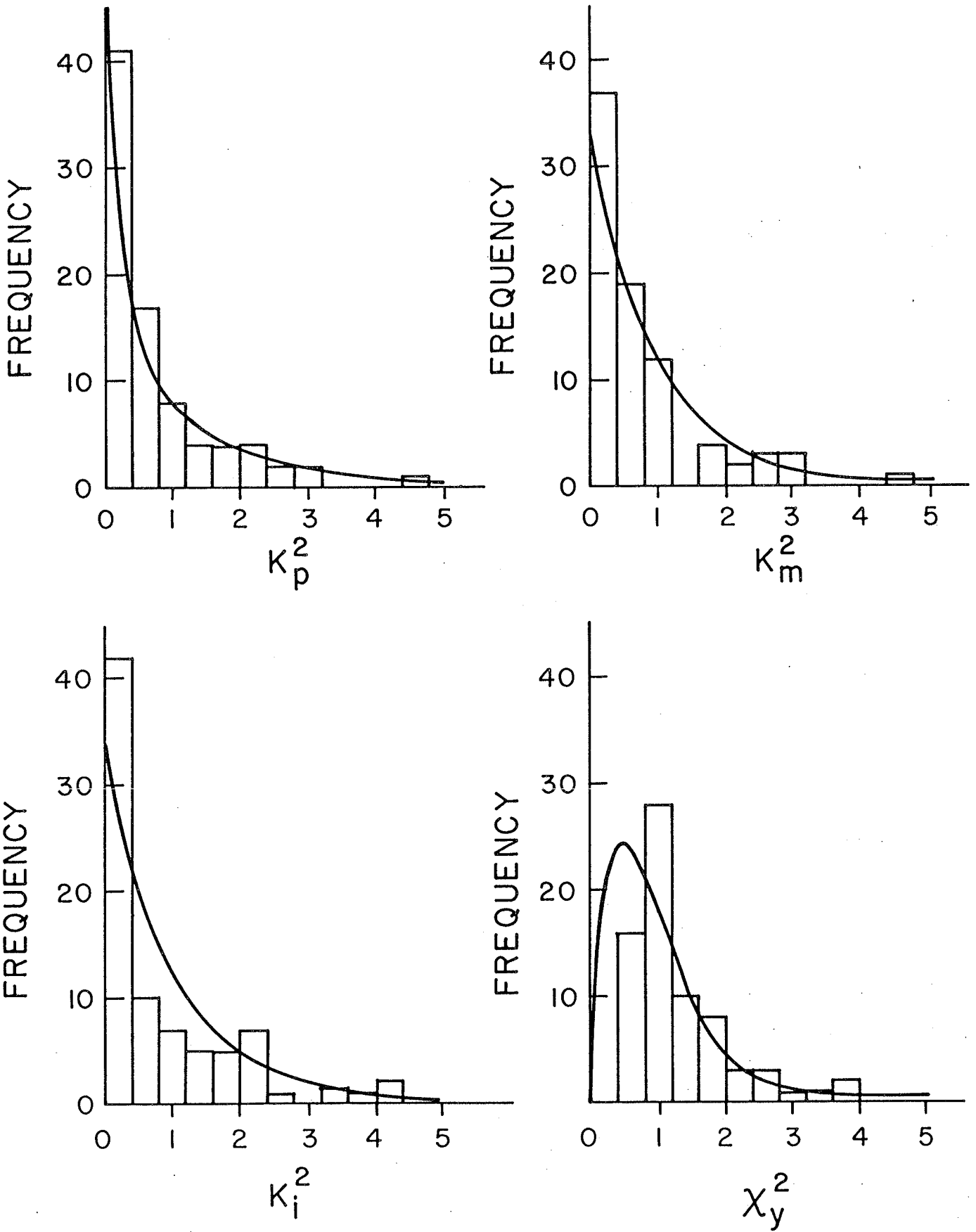


FIG. 4.3 The distribution of consistency measures defined in the text [Eqs. (IV.19) to (IV.22)]. Smooth curves are the expected distributions.

Table 4.2. ^3He analyzing powers from 25 MeV to 35 MeV at angles less than 100 degrees (normalization error is 5 %).

Lab angle (deg)	c.m. angle (deg)	Analyzing power at 25.0 MeV	c.m. angle (deg)	Analyzing power at 30.0 MeV
30.0			39.8	-0.073 ± 0.042
40.0	52.6	-0.094 ± 0.026	52.7	-0.064 ± 0.018
50.0	65.1	-0.136 ± 0.024	65.1	-0.185 ± 0.024
60.0	77.1	-0.187 ± 0.026	77.1	-0.249 ± 0.027
70.0	88.6	-0.239 ± 0.044	88.6	-0.231 ± 0.039
80.0	99.5	-0.262 ± 0.097	99.5	-0.356 ± 0.092
90.0	109.8	-0.11 ± 0.16	109.8	-0.09 ± 0.14

Table 4.2. Continued.

Lab angle (deg)	c.m. angle (deg)	Analyzing power at 32.5 MeV	c.m. angle (deg)	Analyzing power at 35.0 MeV
30.0	39.8	-0.057 ± 0.025	39.9	-0.036 ± 0.019
40.0	52.7	-0.066 ± 0.021	52.7	-0.090 ± 0.019
50.0	65.2	-0.142 ± 0.025	65.2	-0.142 ± 0.027
60.0	77.2	-0.209 ± 0.026	77.2	-0.229 ± 0.030
70.0	88.7	-0.246 ± 0.027	88.7	-0.252 ± 0.033
80.0	99.6	-0.232 ± 0.043	99.6	-0.286 ± 0.052
90.0	109.9	-0.144 ± 0.067	109.9	-0.161 ± 0.076
100.0	119.5	$+0.26 \pm 0.11$	119.5	$+0.05 \pm 0.14$

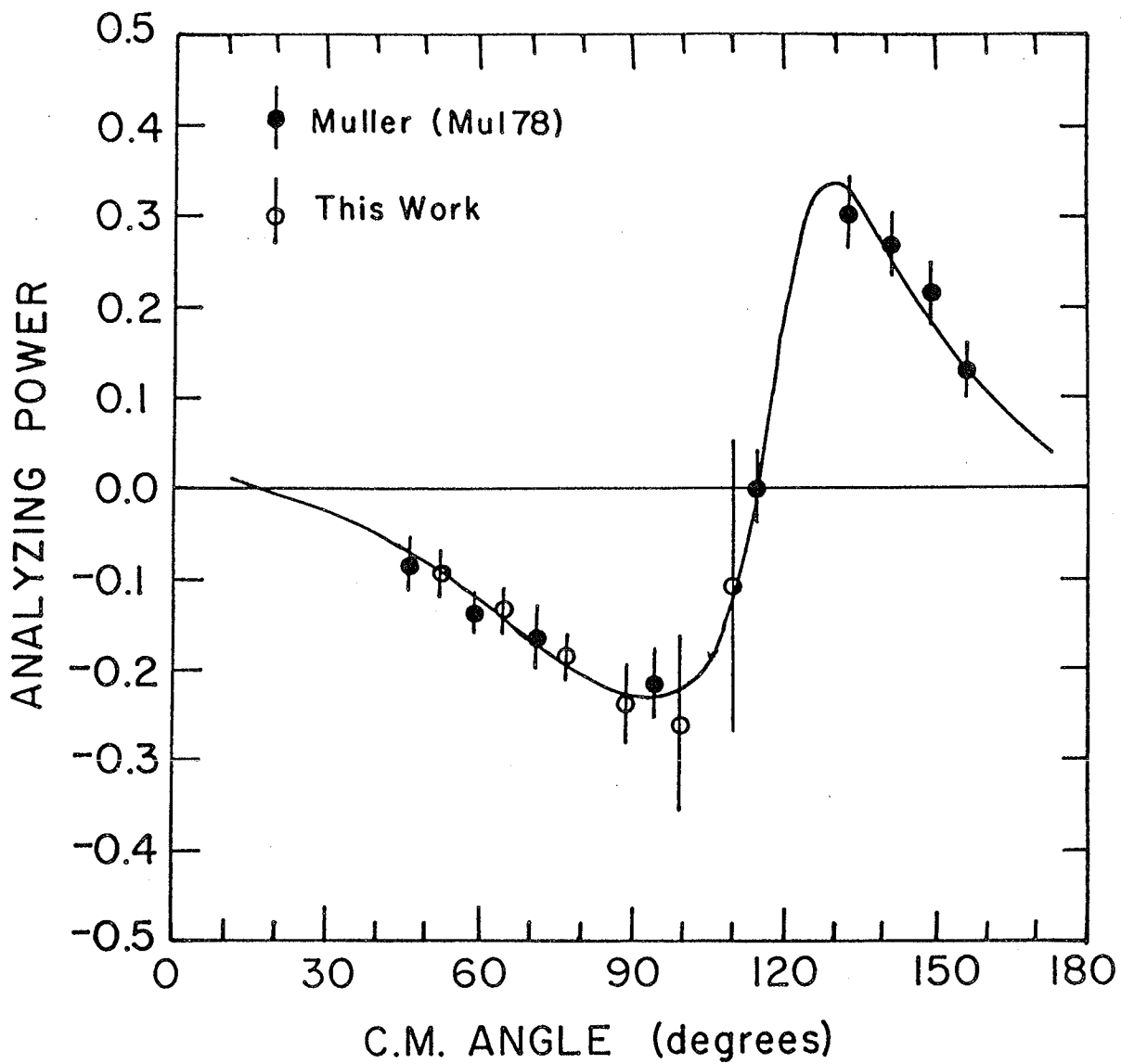


FIG. 4.4 A comparison of analyzing power data at 25 MeV with those of Muller et al. (Mul78). The smooth curve is calculated from the phase shift analysis in Sec. V.

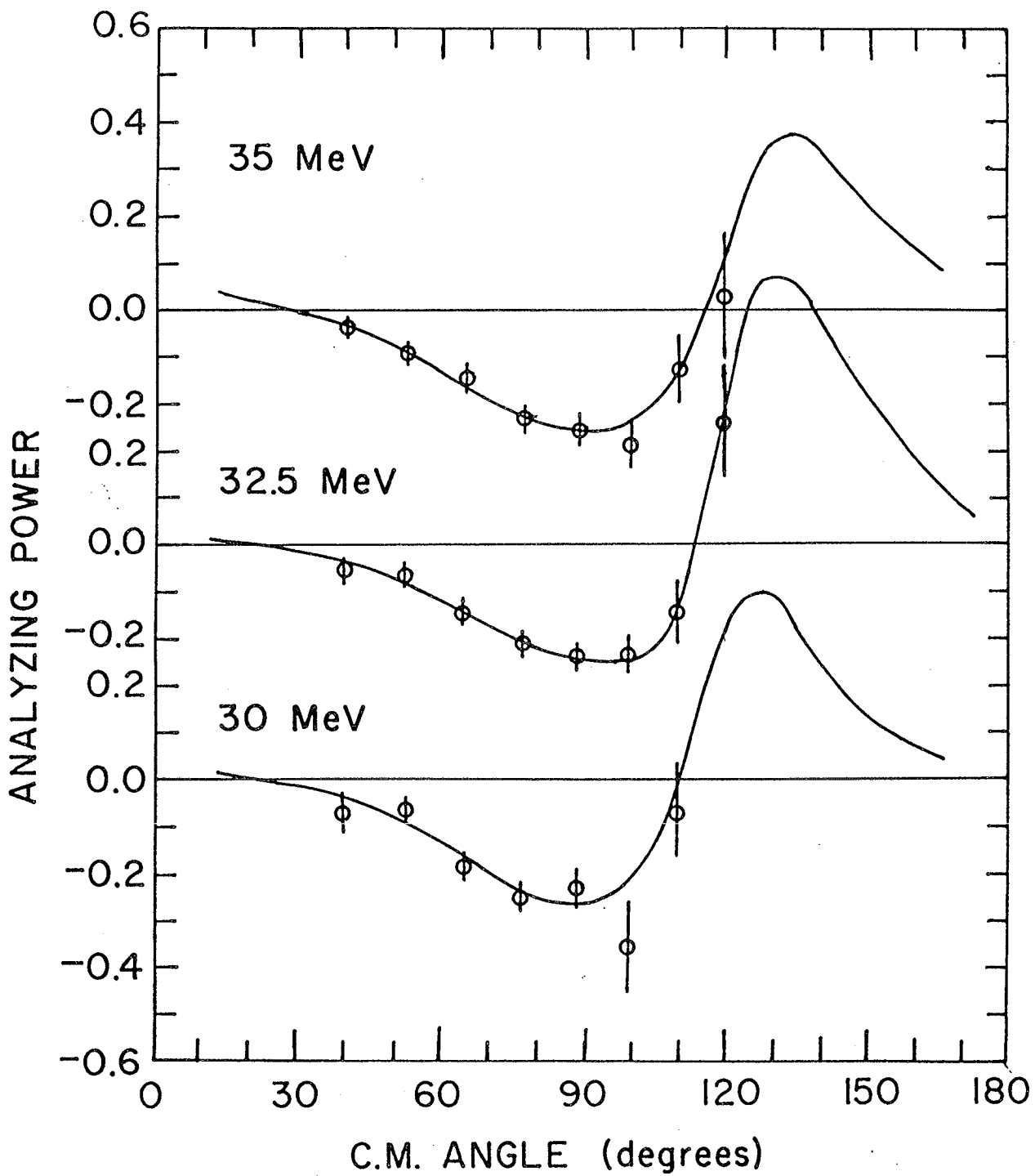


FIG. 4.5 ^3He Analyzing powers at 30, 32.5, 35 MeV. The smooth curve is calculated from the phase shift analysis in Sec. V.

angles and energies this is also the case.

Further a normalization error has to be taken into account, which is mainly determined by the systematic error of 5% in the polarization determination (Sec. II.F). The measurement method is such that all magnetic field related and instrumental asymmetries are effectively eliminated up to at least the first order in their magnitudes [Eq. (IV.8)]. Any second order effect would be on the order of 0.05^2 , the square of a typical value for these asymmetries. Therefore, these effects are negligible compared with the polarization related error. This also applied to the finite detector geometry correction which was estimated to be approximately 0.001 or less.

A comparison with previously measured data at 25 MeV (Mul78) shows good agreement (Fig. 4.4). Data at the remaining energies are presented in Fig. 4.5. The solid line drawn in each figure is the result of the phase shift analysis of Sec. V. These data alone do not show a significant change over the interval under consideration, except that the analyzing powers become slightly more negative at the minimum with increasing energy.

V. PHASE SHIFT ANALYSIS

A. Introduction

The collision process of two distinguishable particles with spin $1/2$ can be fully described with a set of phase shifts and coupling parameters. For each partial wave there are generally three triplet phase shifts, one singlet phase shift, and a coupling parameter describing the mixing between the singlet and triplet states with $J=L$. Coupling is also possible between the triplet states of two partial waves, that have a difference in L of two and that have the same angular momentum and parity. In the S-wave only one singlet and one triplet state exist.

The formalism used here, is that of Tombrello et al. (Tom62), which is referred to by most authors who had performed phase shift analyses in the energy region under consideration (Table 5.1). The diagonal S-matrix elements are described by

$$S_{SLJ} = \eta_{SLJ} e^{2i\delta_{SLJ}}, \quad (V.1)$$

where δ_{SLJ} is the phase shift and η_{SLJ} is the inelasticity parameter. Both are real numbers and $0 \leq \eta \leq 1$. Coulomb phase shifts are included as described by Tombrello et al. (Tom62).

Table 5.1. Previous reports on single energy phase shift analyses for energies less than 50 Mev.

Energy (MeV)	Reference
<1.0	Ber80
1.0	Tom65
1.6	Tom65
2.0	Tom65
2.3	Tom65, Sza78
2.4	Dri67
2.6	Dri67
2.9	Dri67
3.0	Tom65, Sza78
3.2	Dri67
3.5	Dri67, Tom65
3.8	Dri67
4.0	Tom65, Mor69, McS70, Sza78
4.2	Dri67
4.5	Tom65, Dri67, Mor69, Sza78
5.5	Tom65, Dri67, Mor69, McS70, Sza78
6.5	Tom65
6.8	Tom65, Dri67, Mor69, McS70, Sza78
7.5	Tom65
8.5	Tom65
8.8	Tom65, Mor69, McS70, Sza78
9.5	Tom65
10.4	Tom65
10.8	Tom65, Mor69, McS70
11.5	Tom65
13.6	Sza78
18.0	Mor75
19.4	Bak71, Dar72
20.0	Mor75
22.5	Mor75
25.0	Mor75, Mul78
27.5	Mor75
30.0	Mor75
30.5	Har70, Dar72, Mul78
35.0	Mor75
49.5	Har70

Coupling parameters are given by the angle, ϵ , used in the unitary transformation of the diagonal S-matrix

$$\begin{pmatrix} \cos\epsilon & -\sin\epsilon \\ \sin\epsilon & +\cos\epsilon \end{pmatrix} \begin{pmatrix} S_{S_1 L_1 J_1} & 0 \\ 0 & S_{S_2 L_2 J_2} \end{pmatrix} \begin{pmatrix} \cos\epsilon & \sin\epsilon \\ -\sin\epsilon & \cos\epsilon \end{pmatrix}, \quad (\text{V.2})$$

where for singlet-triplet coupling within a partial wave

$$S_1 = 0, S_2 = 1, \text{ and } L_1 = L_2 = J, \quad (\text{V.3})$$

and for the tensor coupling

$$S_1 = S_2 = 1, L_1 = J-1, \text{ and } L_2 = J + 1. \quad (\text{V.4})$$

Mixing angles, ϵ , are listed according to the total angular momentum and parity of the states that they are affecting i.e. $\epsilon(1^+)$, $\epsilon(2^-)$, etc.

The above definition, concerning the tensor coupling, is that followed by McSherry and Baker (McS70, footnote 10), which implements the notes made by Tombrello et al. on the formulas for scattering amplitudes (Tom62). This was the opposite of the convention used by Szaloky and Seiler (Sza78b), whose computer program, SHOSH, was modified here.

At energies less than 13 MeV, extensive single energy phase shift analyses exist (Table 5.1) based on an interpretation of differential cross sections, proton analyzing powers, ^3He analyzing powers, and a few

spin-correlation parameters. Normally, real phase shifts for S-, P-, and D-waves were determined as well as $\epsilon(1^+)$ and $\epsilon(1^-)$. The analyses at higher energies included phase shifts for F-waves and the mixing angles $\epsilon(2^+)$ and $\epsilon(2^-)$. However, in the latter case, the input data were often limited to differential cross sections, and interpolated proton analyzing powers. The major exception is the analysis of Baker et al. (Bak71), which is based on five different data sets: differential cross sections, proton and ^3He analyzing powers, and the spin-correlation parameters A_{xx} and A_{yy} . Their set of phase shifts has been used by later authors (Table 5.1) as a starting point for phase shift determinations at higher energies. Morales et al. (Mor75) included only a singlet G wave term in the search, because it was found that L=4 waves were small.

So far, most authors excluded inelasticity, due to a lack of data on reaction cross sections, limitations on the size of the parameter space (Mul78), or because reactions were considered negligible (Bak71). In fact, the reaction channel is open for two-body breakup, $^3\text{He}+p \rightarrow d+2p$ above 5.5 MeV, and it is open for three-body breakup, $^3\text{He}+p \rightarrow n+3p$, above 7.7 MeV. Reaction cross sections are now available (Sou76), and it was found that between 5% and 25% of the total cross section is attributable to the reaction channels in the energy range from 20 to 35 MeV

Besides the single energy phase shift analysis (Table 5.1), there are two studies using the R-matrix parametrization of the phase shifts (Lan58). Hale et al. (Hal74) analyzed all data up to 19 MeV and Brown (Bro78) presented a preliminary analysis for the region from 20 MeV to

50 MeV. The latter study used accurate data of differential cross sections (Mur79), reaction cross sections (Sou76), and proton analyzing powers (Wat77). Other spin-dependent observations such as ^3He analyzing powers were not included.

With the added ^3He analyzing powers above 20 MeV (Tables 1.2 and 4.2) new single energy phase shift analyses were done. The next section describes the computer program, that was adapted for this, and it is followed by the results and a discussion of these, in relation to the previous phase shift analysis, and the R-matrix analysis of Brown (Bro78).

B. Computer Program SHOSH2

The original FORTRAN program, SHOSH (acronym for Spin Half On Spin Half), was written at the University of Wisconsin and obtained from Szaloky (Sza78a; and J. Birchall, private communication). It had been used with four partial waves to interpret low energy data of the proton- ^3He scattering system. For the interpretation of the present data, it was modified to allow any number of partial waves by adjustment of array sizes only. Also the coding was optimized, resulting in a fourfold increase of the computation speed. One iteration for 90 data points, 5 partial waves, and 33 adjustable parameters, takes about 20 seconds CPU on the VAX 11/750 computer of the Cyclotron Laboratory. This is equivalent to 1.5 seconds CPU on the University of Manitoba Amdahl computer. Storage requirements depend mainly on the number of angles at which data were taken and the number of partial waves, because

these determine the array sizes.

Input to the program are differential cross sections, proton analyzing powers, ^3He analyzing powers, and the spin correlation parameters, A_{xz} , A_{xx} , and A_{yy} . A normalization error can be given for each set. Added to this, in SHOSH2, was the reaction cross section, that is calculated with

$$\sigma_R = \frac{\pi}{k^2 (2S_1+1)(2S_2+1)} \sum_{L,S} (2J+1) (1-\eta_{SLJ}^2), \quad (\text{V.5})$$

where

k = wavenumber,

J = angular momentum, associated with each partial wave, and

S_1, S_2 = spins of the two particles, here both 1/2.

For a set of complex phase shifts chi-square is evaluated from

$$\chi^2 = \sum_{\substack{\text{all data} \\ \text{sets, } k}} \left(N_k \left[\frac{f_k - 1}{\Delta f_k} \right]^2 + \sum_{i=1}^{N_k} \left[\frac{y_{\text{exp},ki} - y_{\text{cal},ki} f_k}{\Delta y_{\text{exp},ki}} \right]^2 \right), \quad (\text{V.6})$$

where

N_k = number of data points in data set k ,

f_k = normalization, if applicable,

Δf_k = normalization error, if applicable,

y_{exp} = experimental value,

y_{cal} = calculated value from a set of phase shifts,

Δy_{exp} = error in the experimental value, and

i = index for a data point in each data set.

In the parameter search, the inelasticity was more easily included

through the use of complex phase shifts. To ensure that all η_{SLJ} are less than unity, it sufficed to limit the search to that part of the parameter space where the complex phase shifts have positive imaginary parts.

Once a set of phase shifts is given, the normalization parameters are found at the minimum of chi-square by equating the first derivative of Eq. (V.6) with respect to f_k , to zero

$$f_k = \frac{\frac{N_k}{(\Delta f_k)^2} + \sum_{i=1}^{N_k} \frac{y_{\text{exp,ki}} y_{\text{cal,ki}}}{(\Delta y_{\text{exp,ki}})^2}}{\frac{N_k}{(\Delta f_k)^2} + \sum_{i=1}^{N_k} \left(\frac{y_{\text{cal,ki}}}{\Delta y_{\text{exp,ki}}} \right)^2} \quad (\text{V.7})$$

Experience has shown that at the end of each search the normalization constants were all close to unity and well within error bars.

Chi-square was minimized with the gradient search technique, which, in SHOSH2, was supplemented by a variable metric method (Arn66). This combination proved to give a significantly faster convergence than with the gradient search alone.

After the search had converged, a further evaluation was done, in SHOSH2, using the second-order expansion matrix or curvature matrix (Arn66) defined by

$$A_{ij} = \frac{1}{2} \frac{\partial^2 \chi^2}{\partial p_i \partial p_j}, \quad (\text{V.8})$$

and the gradient vector defined by

$$B_i = \frac{1}{2} \frac{\partial \chi^2}{\partial p_i}, \quad (V.9)$$

where p represents any of the adjustable parameters. The changes in the parameters are obtained by evaluating the vector

$$\vec{\Delta p} = \overline{A}^{-1} \vec{B} \quad (V.10)$$

followed by a search along this vector for a minimum in chi-square. The matrix, \overline{A} , is often nearly singular, when the number of adjustable parameters is large (>20) and the "real" minimum is not near enough. Therefore, large changes in the parameters calculated from Eq. (V.10), were considered an indication of such a situation, and the gradient search was resumed from the parameter set found with Eq. (V.10).

The evaluation of the matrix elements A_{ij} [Eq. (V.8)] is subject to errors, because numerical differentiation is susceptible to rounding off errors and higher order terms in the expansion of chi-square around the minimum. To minimize this effect the final steps were verified with another version of the program, SHOSH2DP, whereby Eqs. (V.1), (V.2), and (V.6) to (V.10) were evaluated with double precision accuracy. This version had only 1/3 the speed of the regular version, and was therefore not used for the routine gradient search.

Errors in the parameters are determined from the diagonal elements of the inverse curvature matrix, \bar{A}^{-1} , using

$$\sigma_k = \left(A_{kk}^{-1} \frac{\chi^2}{n_f} \right)^{1/2}, \quad (\text{V.11})$$

where n_f is the number of degrees of freedom. An alternative to this is the evaluation of the change, s_k , of the parameter, p_k , that increases chi-square by n_f , which is similar to a method used in the analysis of the proton- ^4He elastic scattering system (Hou78). An approximation for this is given by

$$s_k = \left(\frac{n_f}{A_{kk}} \right)^{1/2}. \quad (\text{V.12})$$

Eq. (V.11) is an expression derived from the variance calculation in the linear least squares method. It applies here as long as one can assume that y_{cal} is nearly linear with respect to the parameters, and that the statistical errors, Δy_{exp} , are normally distributed and uncorrelated. Therefore, the results of Eq. (V.11) were quoted, whenever the curvature matrix could be evaluated satisfactorily. Otherwise, the result of Eq. (V.12) is quoted.

C. Procedure and Results

A single energy phase shift analysis was performed at seven energies between 19.5 and 35 MeV. The data base was selected from Tables 1.1 and 1.2, and consisted of

- a) the differential cross sections obtained at the University of

Manitoba (Mur79), and at 19.5 MeV from Hutson et al. (Hut71),
b) the proton analyzing powers obtained at LBL (Wat77, Bir81), and at
19.5 MeV from Baker et al. (Bak71),
c) the ^3He analyzing powers obtained from the Manitoba group (Table
4.2), and from Baker et al. (Bak71), Muller et al. (Mul78), and Ware
et al. (War75), and
d) the total reaction cross sections obtained at the University of
Manitoba (Sou76, and interpolated values when necessary).

The experience has been that several sets of phase shifts can fit
the same data producing a similar chi-square. With a maximum of 43
possible parameters for 5 partial waves, it is evident that a random
search of all possible minima on the chi-square surface is not feasible.
The original selection was therefore limited to the real phases up to
 $L=4$, the imaginary phases up to $L=3$, and the coupling parameters up to
 $J=3$. A preliminary analysis of the data showed that at all energies the
inelasticity parameters in the 1S_0 -, 1F_3 - and 3F_2 , and the mixing angles
at $J=3$ were negligible. The R-matrix analysis (Bro78) yielded a similar
result. These parameters were therefore excluded from the original set.
There remained: 18 real phases, 11 imaginary phases, and 4 mixing
angles.

A further restriction is that the phases should be continuous
throughout the energy range. The starting point was at 19.5 MeV. Here
exists the least incomplete set of observables: five data sets and one
total reaction cross section. Besides the availability of a reaction
cross section, the data differ from those used in previous analyses
(Bak71, Dar72), because the differential cross sections were replaced by

a weighted average of the data from Hutson et al. (Hut71) and Murdoch et al. (Mur79). Starting from the real phases of Baker et al. (Bak71) a new set of complex phase shifts was arrived at (Table 5.2).

At higher energies the gradient search was started with the phase shifts obtained at the next lower energy. In the initial stage of the search a virtual data set was used that contained all experimentally determined quantities at a particular energy and spin-correlation parameters extrapolated from the calculated results at lower energy. Thus new phase shifts were obtained that provided a starting point for the gradient search with the experimental data only. The above ensured a measure of continuity in energy of the phase shifts.

It became clear that the imaginary phases could not be determined completely without ambiguity. The approach adopted finally was to use a single constant for all imaginary phases, such that the calculated total cross section equaled the experimental value. Subsequently, the imaginary phases were allowed to vary and it was hoped that the direction of the deviations from the single constant, would give at least an indication of the relative contribution of each partial wave to the reaction channel.

Whenever chi-square reached a minimum, it was observed that the normalization constants calculated with Eq. (V.7) were close to unity, and well within error bars. This implied that any error in the normalization can be compensated by an appropriate variation in the complex phases. Therefore, to reduce the number of computations per iteration, the normalization constants were kept at unity in the early

Table 5.2. Sets of real phase shifts and coupling parameters at 19.5 MeV by various authors.

	Baker et al. (Bak71)	Darves-Blanc et al.(Dar72)	Brown (Bro78; R-matrix)	Present work
1S_0	-120.8	-109.3	-129.0	-116.2 \pm 1.1
3S_1	-111.2	-105.9	-105.3	-97.8 \pm 0.4
1P_1	26.1	31.8	33.6	23.2 \pm 0.6
3P_0	41.6	45.8	49.5	46.5 \pm 1.2
3P_1	46.9	48.4	42.4	52.4 \pm 0.6
3P_2	63.1	68.1	61.2	70.3 \pm 0.3
$\epsilon(1^-)$	-40	-30		-25.8 \pm 1.0
$\epsilon(1^+)$	-4.2	-2.92		-3.8 \pm 0.5
1D_2	-2.3	-4.78	-10.8	-4.0 \pm 0.6
3D_1	3.4	3.31	-19.4	1.5 \pm 0.5
3D_2	3.1	2.71	14.2	-0.4 \pm 0.5
3D_3	5.6	6.08	-1.2	2.3 \pm 0.2
$\epsilon(2^+)$	-9.5	-2.16		-17.3 \pm 6.8
$\epsilon(2^-)$	-4.6	-6.60		-1.0 \pm 0.8
1F_3	3.1	4.25	3.2	-1.4 \pm 0.5
3F_2	1.7	3.87	-3.6	2.7 \pm 0.3
3F_3	0.8	-0.32	7.0	3.9 \pm 0.6
3F_4	3.9	3.91	-1.8	4.0 \pm 0.2
1G_4			-0.1	-0.6 \pm 0.4
3G_3			-0.8	-0.7 \pm 0.3
3G_4			-1.3	0.6 \pm 0.4
3G_5			0.2	-0.3 \pm 0.2
no of data points	97			92
chi-square per point	1.49	?	?	0.72

stages of the analysis at each energy.

Errors in the parameters were calculated with Eqs. (V.11) and (V.12) using a double precision version of the program SHOSH2. When all 33 parameters were searched, the curvature matrix was nearly singular. The matrix normally became non-singular, when the imaginary phases were excluded. The errors calculated with Eq. (V.11) using this smaller matrix, are quoted in Table 5.3. They form a good basis for comparison with other analyses (Table 5.1), because these mostly exclude imaginary phases.

In summary, the procedure for the determination of the phase shifts with 33 adjustable parameters consisted of the following steps

- a) extrapolated polarization data were added, real phases and coupling parameters were varied, imaginary phases were set at a constant, the normalization factors were kept at unity, and the variable parameters were started from the results at the next lower energy,
- b) the extrapolated data were removed, all complex phases and coupling parameters were allowed to vary, and the variable parameters started from the results of step a),
- c) the normalization factors were included through Eq. (V.7), and the double precision version of the program was used starting from the result of stage b).

This gives the final results of all parameters, and

- d) the program was run once more to find the errors in the real phases and coupling parameters.

An example of the fit to the data at 27.5 MeV is given in Fig. 5.1, and

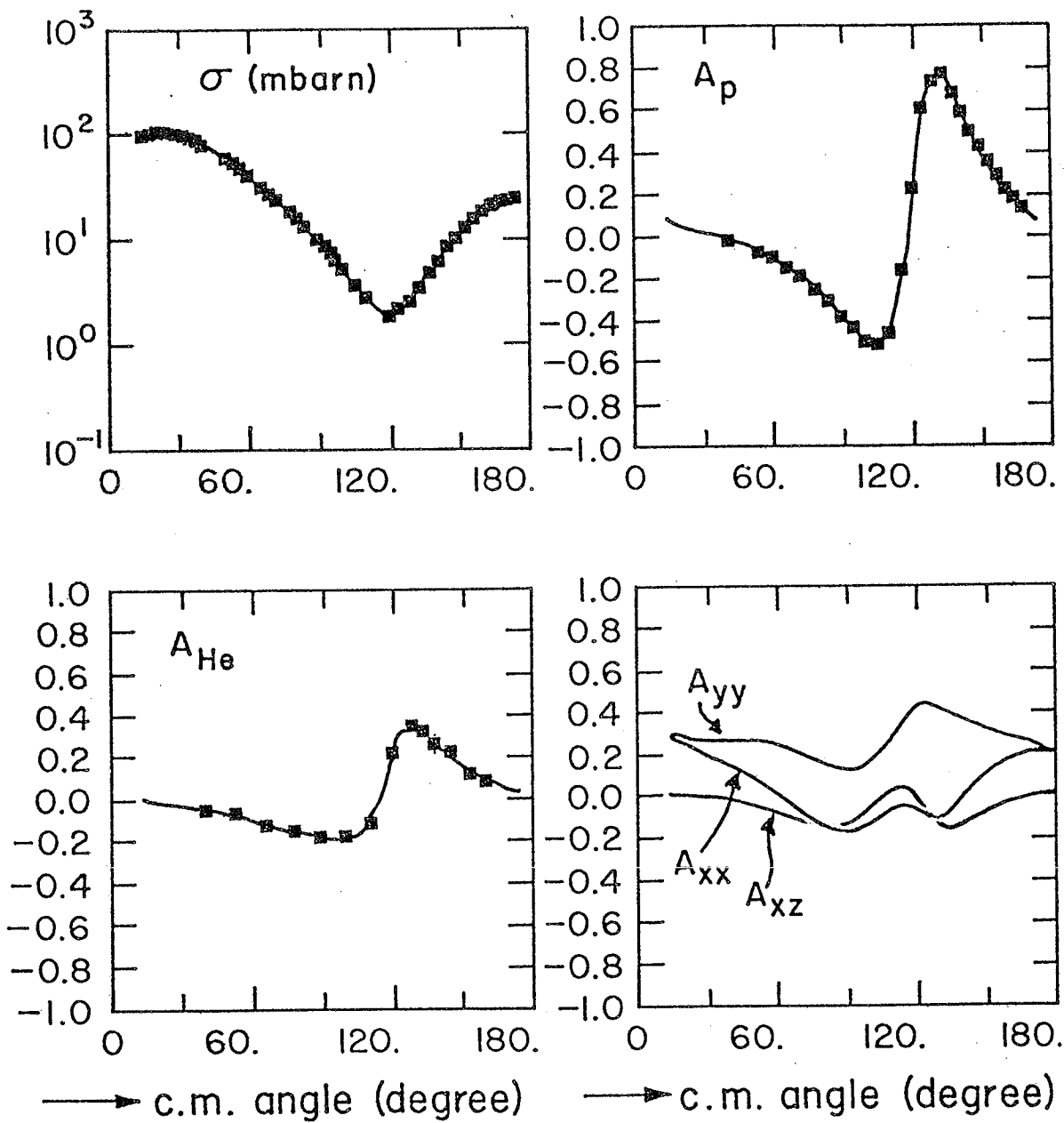


FIG. 5.1 Comparison of the data at 27.5 MeV and the observables calculated from the phase shift analysis.

the calculated ^3He analyzing powers at 25, 30, 32.5 and 35 MeV are displayed as the solid lines in Figs. 4.4 and 4.5.

The parameters, excluding the imaginary phases, are listed in Table 5.3 and illustrated in Figs. 5.2-5.8. The inelasticity parameters did not differ substantially from their starting values, which ranged from 0.970 at 19.5 MeV to 0.865 at 35.0 MeV, and had an error of approximately 0.04 [from Eq. (V.12)].

At 32.4 MeV a very poor fit was recorded. The results listed for this energy (Table 5.3) were obtained with the procedure described before. The poor fit remained despite deleting apparent outliers, and trying several different sets of starting values for the parameters. Chi-square was particularly large for the differential cross sections at the back angles ($\theta_{\text{cm}} > 105^\circ$ or $\theta_{\text{lab}} > 85^\circ$). Two explanations appear possible: a) there has been an error in the evaluation of the differential cross sections at the back angles, and b) there exist unexpected excursions in the phase shifts. The first hypothesis is supported by an inspection of the smoothness of the differential cross sections with respect to energy and angle. The back angle data at 32.4 (and 37.5) MeV appear to deviate from the trend. In support of the second hypothesis is the fact that relatively large variations of some parameters ($\epsilon(2^+)$, δ_{044} , δ_{144} , and maybe δ_{122} , see Figs. 5.2 to 5.8) are apparent between 30 and 35 MeV.

A redetermination of the differential cross sections in this region should resolve which explanation is valid. The results of the phases at 32.4 MeV should be seen as the outcome of a preliminary analysis.

Table 5.3. Sets of real phase shifts and coupling parameters between 19.5 and 35 MeV.

Energy (MeV):	19.5	21.3	25.0	27.5	30.0	32.4*	35.0
1S_0	-116.2±1.1	-121.4±2.3	-127.9±3.9	-125.0±2.5	-125.0±2.7	-129.2	-135.0±5.1
3S_1	-97.8±0.4	-99.2±0.7	-106.4±0.9	-108.5±1.2	-110.6±0.7	-114.1	-117.1±1.3
1P_1	23.2±0.6	21.0±1.2	21.5±1.2	25.0±2.0	24.8±1.0	24.2	22.3±1.0
3P_0	46.5±1.2	44.7±2.5	40.0±3.3	39.4±5.5	37.2±2.3	34.6	28.2±3.5
3P_1	52.4±0.6	52.8±1.4	52.1±1.8	47.9±1.8	49.2±1.0	46.5	43.9±1.6
3P_2	70.3±0.3	70.7±0.7	67.3±0.8	64.9±1.0	63.6±0.6	61.5	58.3±0.8
$\epsilon(1^-)$	-25.8±1.0	-26.7±1.6	-30.5±1.6	-38.0±6.8	-43.2±3.6	-41.8	-46.4±5.8
$\epsilon(1^+)$	-3.8±0.5	-2.8±1.5	-0.5±2.0	-4.7±4.4	-4.7±2.9	-5.9	-4.2±2.7
1D_2	-4.0±0.6	-3.0±0.8	-0.5±0.9	-3.1±2.0	0.0±0.6	-2.5	-3.0±1.1
3D_1	1.5±0.5	0.0±0.8	-3.7±0.9	-0.6±1.0	-2.0±0.7	-2.9	-3.8±1.1
3D_2	-0.4±0.5	-0.3±1.2	4.4±1.1	7.4±1.1	7.8±0.7	11.7	14.7±2.2
3D_3	2.3±0.2	3.0±0.5	1.9±0.5	3.5±1.0	3.5±0.6	5.3	7.4±1.0
$\epsilon(2^+)$	-17.3±6.8	-18.3±9.8	-25.0±7.2	-31.1±3.7	-30.9±3.7	-19.5	-16.6±2.5
$\epsilon(2^-)$	-1.0±0.8	0.4±2.0	2.8±2.0	-0.7±4.4	-2.9±2.5	-6.8	-2.4±3.7
1F_3	-1.4±0.5	-2.3±0.7	-1.0±0.9	-0.8±0.6	1.9±0.4	-0.8	0.3±0.8
3F_2	2.7±0.3	2.3±0.5	-0.2±0.6	0.4±0.4	-0.6±0.4	-0.8	-2.6±0.5
3F_3	3.9±0.6	4.5±0.7	7.4±0.7	6.1±0.8	7.8±0.6	11.1	11.9±0.7
3F_4	4.0±0.2	4.7±0.3	3.5±0.4	4.5±0.4	4.4±0.3	5.0	6.4±0.5
1G_4	-0.6±0.4	0.3±0.9	1.4±1.1	1.8±1.1	1.8±0.3	1.2	0.3±0.5
3G_3	-0.7±0.3	-1.1±0.5	-0.9±0.4	-0.5±0.6	-0.1±0.3	-0.2	-1.0±0.2
3G_4	0.6±0.4	0.4±0.7	-0.1±0.6	-1.3±1.1	-1.6±0.4	0.4	0.7±0.3
3G_5	-0.3±0.2	-0.7±0.4	-0.4±0.4	-0.2±0.5	-0.1±0.2	0.4	0.0±0.3
no of data points	92	70	90	82	82	83	80
reduced chi-square	1.12	1.15	0.97	0.92	0.97	3.26	0.87

* Preliminary results, see text.

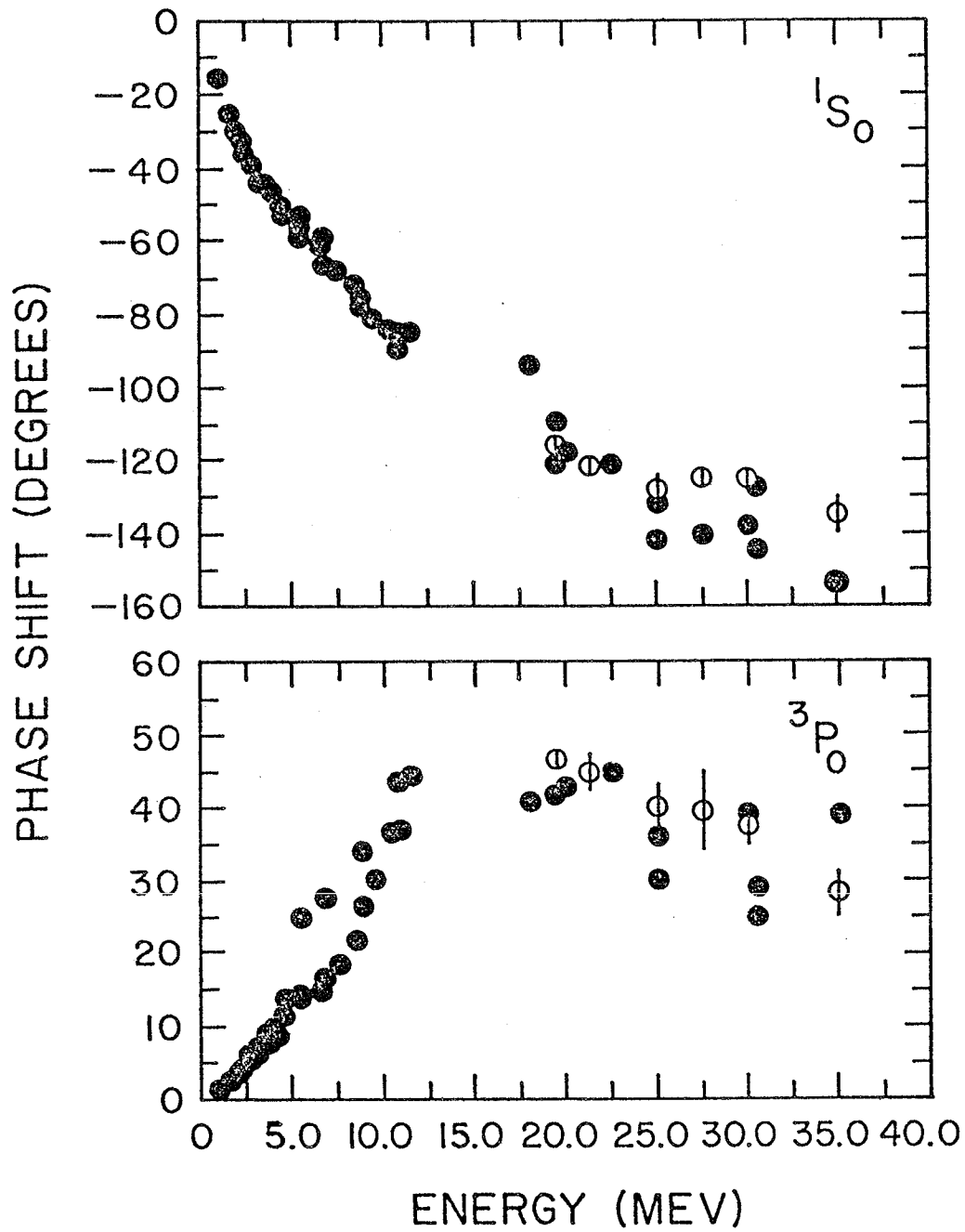


FIG. 5.2 Phase shifts for partial waves with $J = 0^\pm$ (closed circles are from previous analyses, open circles from the present analysis).

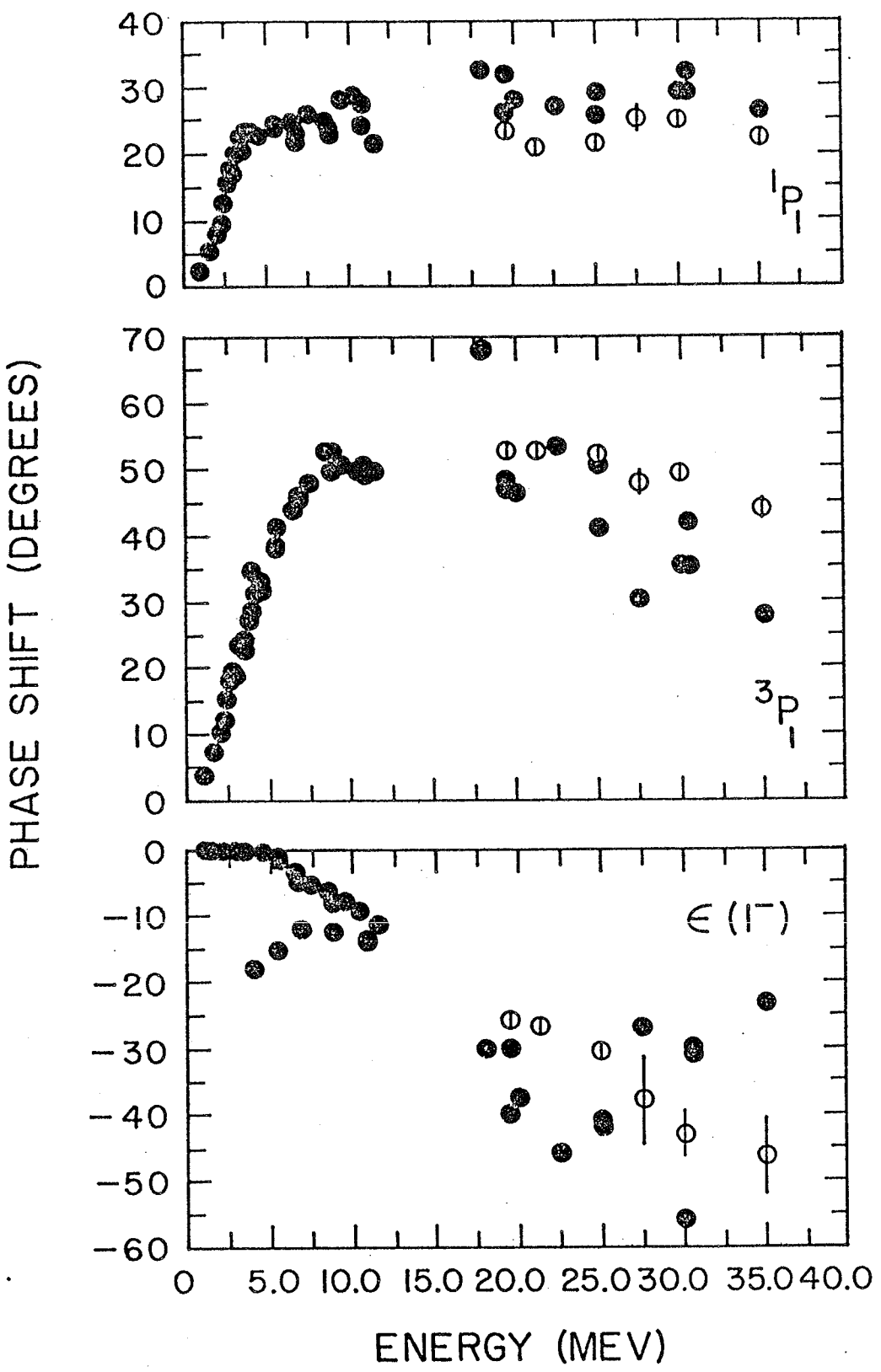


FIG. 5.3 Phase shifts and mixing angle for partial waves with $J = 1^-$ (closed circles are from previous analyses, open circles from the present analysis).

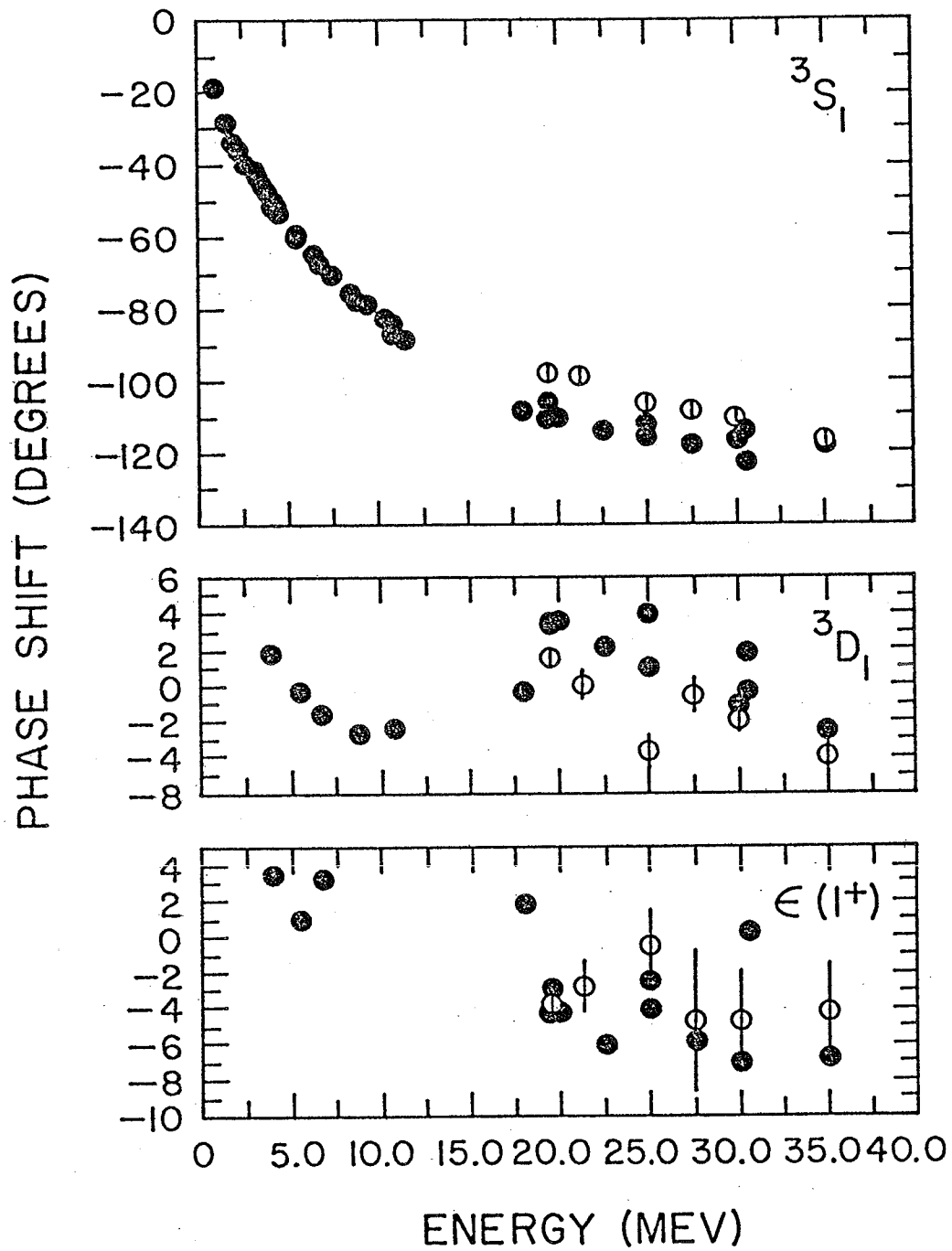


FIG. 5.4 Phase shifts and mixing angle for partial waves with $J = 1^+$ (closed circles are from previous analyses, open circles from the present analysis).

PHASE SHIFT (DEGREES)

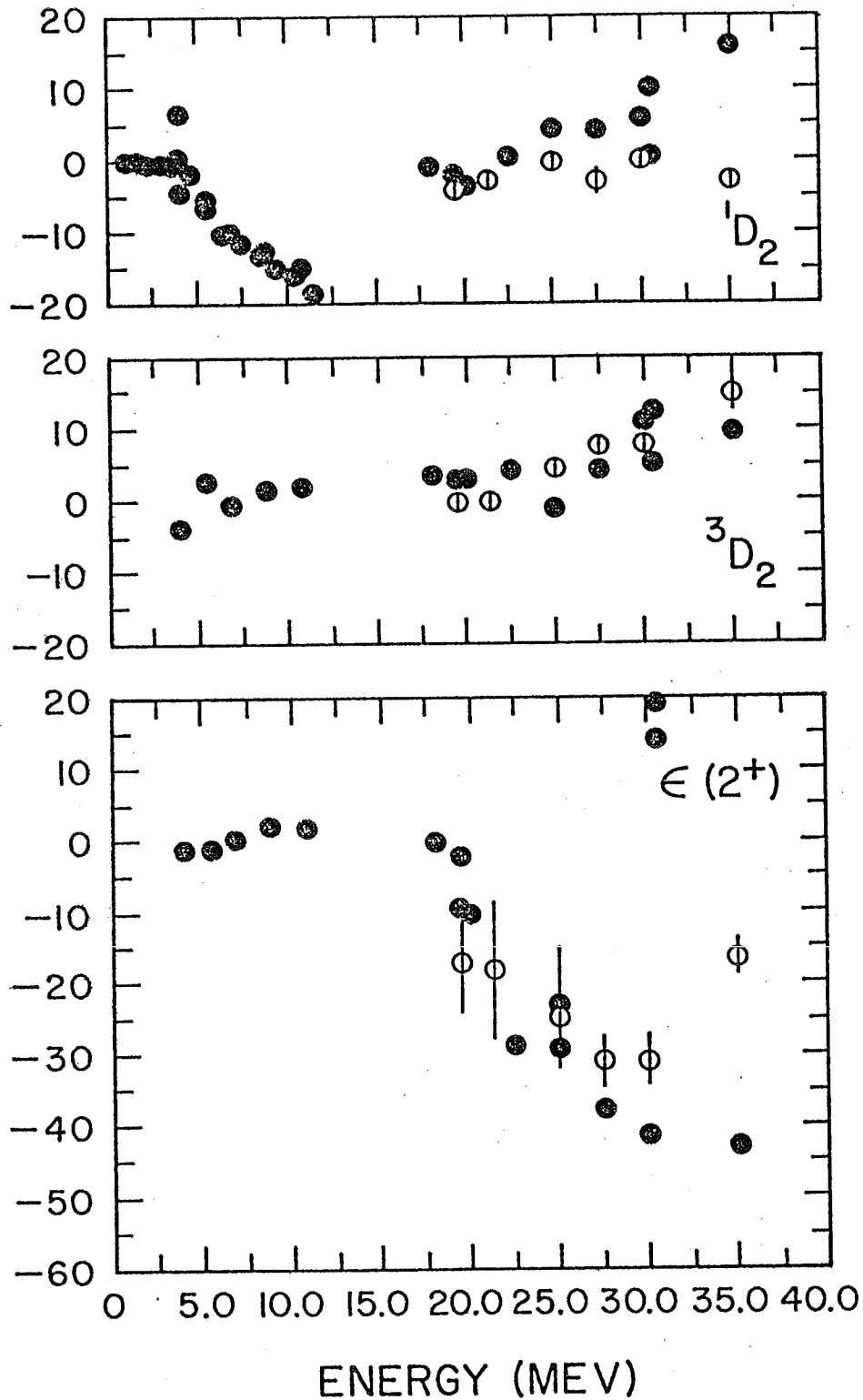


FIG. 5.5 Phase shifts and mixing angle for partial waves with $J = 2^+$ (closed circles are from previous analyses, open circles from the present analysis).

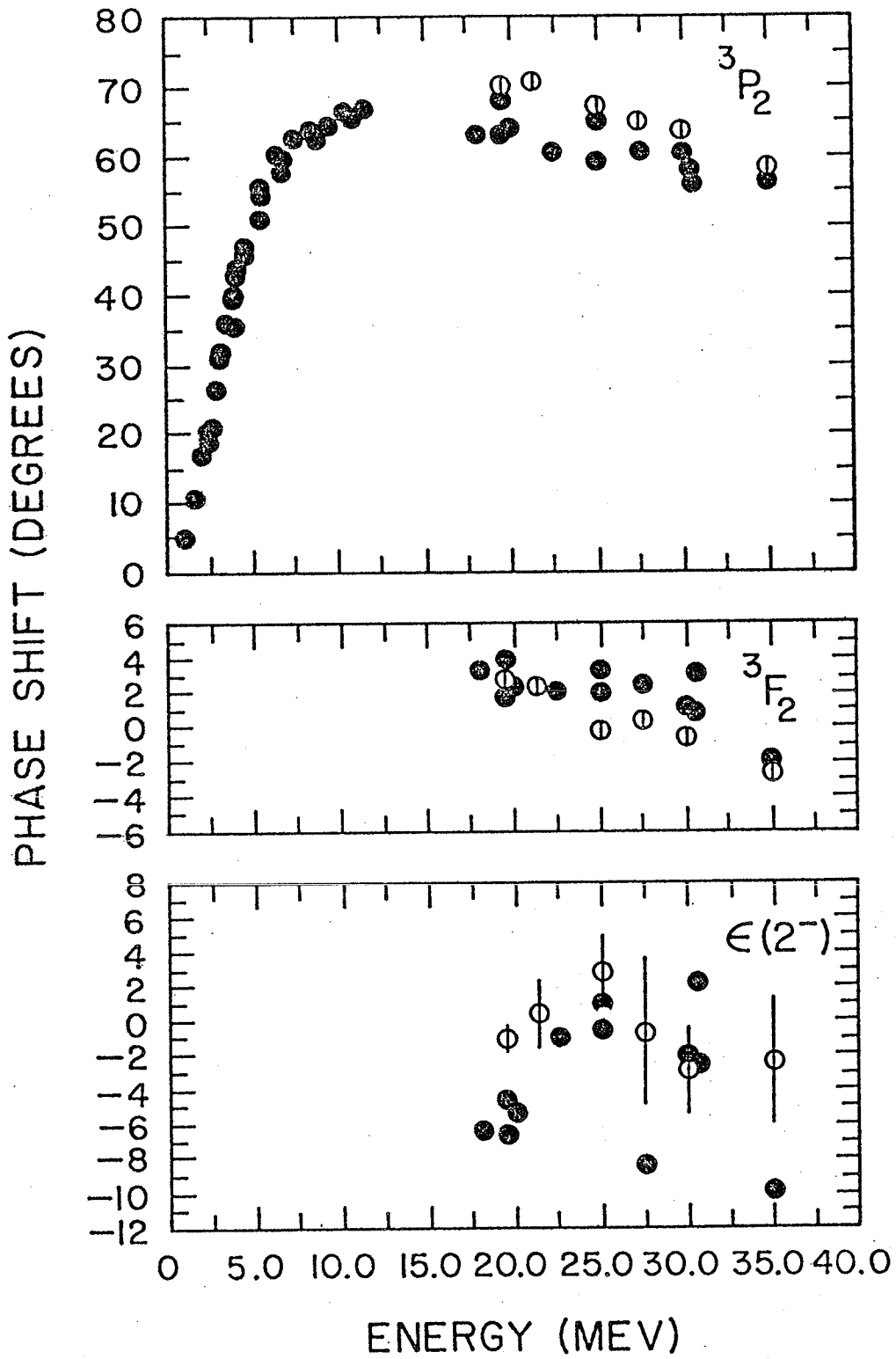


FIG. 5.6 Phase shifts and mixing angle for partial waves with $J = 2^-$ (closed circles are from previous analyses, open circles from the present analysis).

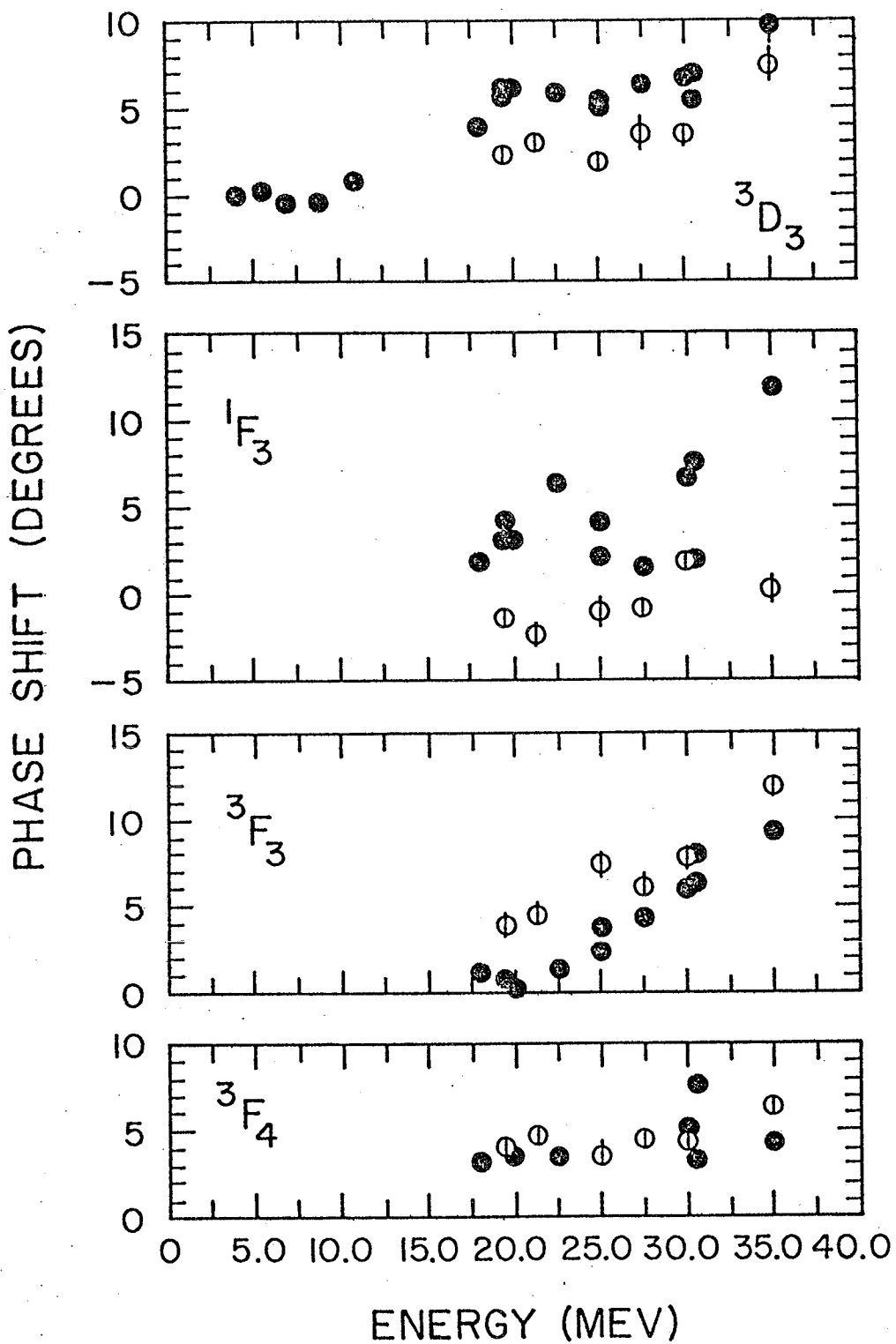


FIG. 5.7 Phase shifts for the 3D_3 -, 1F_3 -, 3F_3 -, and 3F_4 -waves (closed circles are from previous analyses, open circles from the present analysis).

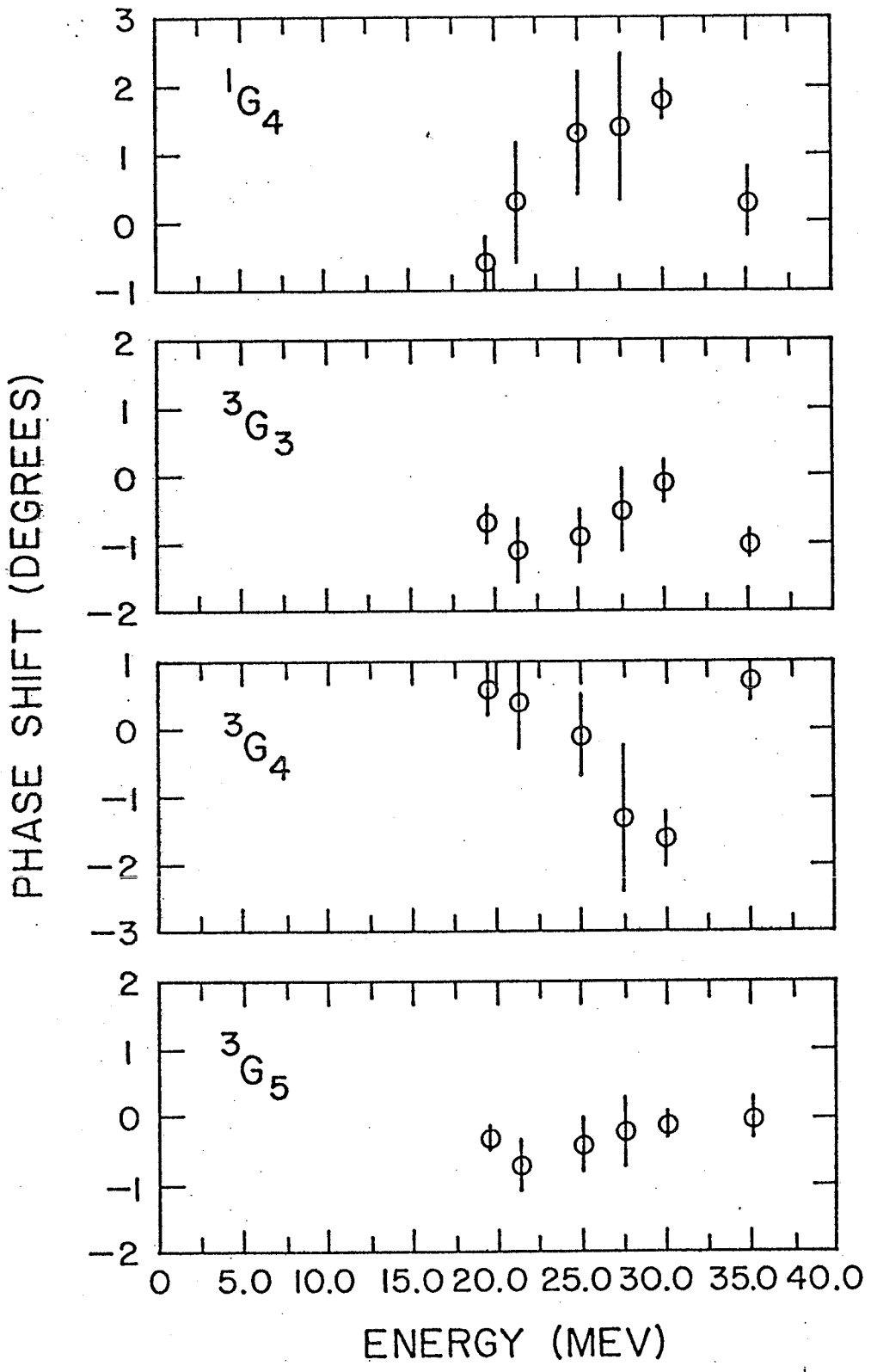


FIG. 5.8 Phase shifts for the G-waves.

In the interpretation of the real phases it should be taken into account that they are determined up to a multiple of 180° . With the present values, the real phases are continuous with those at lower energies where they converge to zero.

Another redundant solution exists for each pair of phases that are subject to the coupling described by Eq. (V.2). Interchanging the two complex phases, and, at the same time, changing the mixing angle by 90° gives an identical result for all observables. Also here, the real phases and mixing angles should be continuous with low energy data eventually converging to zero. In this context the phase shifts of Baker et al. (Bak71) at 19.4 MeV were reexamined and it was found that their result for singlet-triplet mixing of the P-waves should undergo the above mentioned transformation to retain continuity (Table 5.2).

D. Discussion

As mentioned before, the number of observables are limited and there are several phase shift solutions possible. The phase shifts of Figs. 5.2-5.8 have been determined with the requirement that a) they are continuous with energy, and b) they start from the real phases already determined at 19.4 MeV (Bak71).

Generally, the smooth continuation from phase shifts below 11 MeV to those above 19 MeV is satisfactory except for the 1D_2 phase shift, which will be discussed below. Unfortunately, phase shift analyses between 13.6 and 19.4 MeV have not been performed on large data sets. [The results at 13.6 MeV (Sza78a) are not presented in the figures here,

because they could not be recovered reliably from the original publication]. Further work in this region is necessary to ascertain continuity of the phases.

Above 19 MeV, the real phases vary smoothly with energy showing no sudden excursions (Figs. 5.2-5.8). The continuity is also displayed in the data. Major excursions with energy do not occur in the differential cross sections (Mur79), proton analyzing powers (Wat77, Bir81), and ^3He analyzing powers (Mul78, and present work). The phase shift analyses also yielded the spin correlation parameters. A smooth behaviour with respect to energy was obtained for A_{yy} and, to a lesser extent, A_{xx} . The third parameter, A_{xz} , appears to vary more significantly with energy, but there are no data to verify this. An example of each observable is shown in Fig. 5.1. The smooth energy dependence of the parameters and data implies that continuity has been achieved. It is recommended that this be verified by measurement of spin correlation parameters at higher energies.

The starting point of the phase shift search at 19.5 MeV was the result of Baker et al. (Bak71). These authors had found that various arbitrary choices of starting values for the phases always led to a solution close to the one that they reported. There was no evidence of more than one distinct family of phase shifts. The present solution is based on more accurate differential cross sections and gives a better fit on the basis of the chi-square criterion for all the data (Table 5.2). This solution is therefore a better estimate for the phase shifts at 19.5 MeV.

A comparison between former phase shift analyses and the present analysis in the energy range under consideration shows the existence of systematic differences in the results for most partial waves (Figs. 5.2-5.8). This difference is explained by the fact that in the present analysis more inelasticity parameters were allowed and a set of real phases for the G-waves was included. Exclusion of these parameters from the search resulted in real phases that were closer to those of former analyses, but it also resulted in a significant increase in chi-square. In the following, each of the partial waves is discussed separately, and compared with the findings of other authors, who worked in this energy region (Table 5.1). The analyses of Harbison et al. (Har70) are excluded, because they used a limited data set.

1. $J^\pi = 0^\pm$ (Fig. 5.2)

As noted by other authors (Mor75) the hard sphere behaviour of the 1S_0 wave found at lower energies continues to higher energies. The inelasticity parameter for this wave could be set to unity. This indicates that little or no reaction takes place through this channel.

The 3P_0 phase shift behaviour extrapolated back to low energies, intercepts the low energy results at 12 MeV. This has been correlated with the 0^- level in ^4Li (Fig. 1.1, and Mor75). The phase shift decrease with energy appears more consistent in comparison with other analyses.

2. $J^\pi = 1^-$ (Fig. 5.3)

Muller et al. (Mul78) reported that the convention used by Morales et al. (Mor75) was internally inconsistent for singlet-triplet mixing. Our convention [Eqs. (V.2) and (V.3)] is the same as that of Muller et al. (Mul78) and Darves-Blanc et al. (Dar72). The results of Morales et al. (Mor75) could be made to agree with our convention by a transformation similar to one discussed at the end of Sec. V.C.

Morales et al. (Mor75) had noted an anomalous behaviour of the 3P_1 phase shift (e.g. at 18 MeV, Fig. 5.3) and of the mixing angle. Darves-Blanc et al. (Dar72) could not constrain the mixing angle and set it to a constant, -30° , the same result as found by Baker et al. (Bak71). In this analysis, these anomalies have been removed. The mixing angle decreases steadily with energy starting at 5 MeV, which corresponds with the 1^- level in ^4Li (Fig. 1.1). The point of complete mixing, $\epsilon = 45^\circ$, is at about 31 MeV.

3. $J^\pi = 1^+$ (Fig. 5.4)

This exhibits tensor coupling between the triplet S- and D-waves. The 3S_1 phase shift deviates slightly from the hard sphere behaviour above about 15 MeV, showing an interaction that is slightly less repulsive than a hard sphere. Morales et al. (Mor75) attributed this to the importance of inelastic channels drawing on the S-wave strength. Their most important complex terms were in the S-waves. However, this should be considered with care as is discussed in section 8. below.

The mixing angle is negative but small. It was found that the spin correlation parameters were seriously affected by small changes in this parameter. Therefore, its error is relatively small at the energy, 19.5 MeV, where the spin correlation parameters were measured.

4. $J^\pi = 2^+$ (Fig. 5.5)

It is not clear whether Morales et al. (Mor75) had a convention inconsistency for this case of singlet-triplet coupling as with the case $J^\pi = 1^-$. Their tabulated values are displayed in Fig. 5.5. If the inconsistency is present, the 1D_2 - and 3D_2 -phases should be interchanged.

There is an apparent discontinuity in the 1D_2 phase shift between 13 and 20 MeV. The low energy results are well established (Tom65, McS70, Sza78), although the R-matrix analysis at low energies (Hal74; and Brown, private communication) predicts only minor excursions from zero. The analysis of data between 13 and 20 MeV should resolve this issue.

At about 13 MeV the 1D_2 phase shift appears to go through a minimum. The linear extrapolation to lower energies of the trend in $\epsilon(2^+)$ existing between 20 and 30 MeV reaches zero at 13 MeV as well. This is similar to the trends in the 1^- case at 5 MeV. If the analogy is valid, there should be a 2^+ state in ^4Li at 13 MeV (or 33 MeV above the ground state of ^4He , Fig. 1.1).

The 3D_2 phase shift becomes significantly different from zero beyond 25 MeV. The mixing angle goes through a minimum at 28 MeV. These trends should be confirmed when more polarization data are available above 35 MeV.

The present results suggest that the previously found positive mixing angles at 30.5 MeV (Dar72, Mul78), are probably incorrect.

5. $J^\pi = 2^-$ (Fig. 5.6)

Trends observed by previous authors (Dar72, Mor75, Mul78) have been confirmed. The tensor coupling here is apparently negligible as indicated by the size of $\epsilon(2^-)$ with respect to its error (Table 5.3).

6. Remaining D- and F-waves (Fig. 5.7)

The singlet F-wave remains unperturbed. The 3D_3 -wave and the triplet F-waves are increasing functions of the energy. The 3F_3 -wave appears to be the most pronounced of this set.

7. G-waves (Fig. 5.8)

Only Morales et al. (Mor75) included the singlet G-wave in their parameter search. Its behaviour was not discussed by the authors. Fig. 5.8 shows that the 3G_3 and 3G_4 phase shifts are also possibly significant, but not the 3G_5 phase shift. Exclusion of the G-waves from the search process caused a distinct increase in the reduced chi-square at higher energies, and a marginal increase at the lower energies. In order to be consistent throughout the whole energy range, the G-waves

were included in the analysis.

8. Inelasticity parameters

Using only real phases resulted in a chi-square that was sometimes a factor of two above that obtained for complex phases. The presence of inelasticity parameters is therefore essential. However, the distribution of the inelasticity over the partial waves was not constrained by the present data. It depended strongly on the starting values in the parameter search. Therefore it is not surprising that Morales et al. (Mor75) arrived at large inelasticity in the S-waves, because their grid search probably started with the S-waves.

In the present work no clear trends have been found that would indicate an increased inelasticity in particular partial waves.

9. Errors

The errors quoted in Table 5.3 are clearly underestimates as observed from the scatter of the results with respect to apparent smooth trends. Nevertheless, these errors proved useful in assessing the relative sensitivity of each parameter with respect to the data (e.g. in section 3. above), and in deciding on phases that are close to zero.

The above discussion refers to single-energy phase shift analyses only. In order to assure better continuity in energy the R-matrix parametrization of the phase shifts had been employed. Brown (Bro78) did such an analysis in the energy range under consideration. His results are not directly comparable with those of Table 5.3 however. Firstly, the reaction channels are explicitly included in the R-matrix formalism through a 3 x 3 unitary S-matrix, rather than the 2 x 2 S-matrix with complex phases used in Eqs. (V.1) and (V.2). Secondly, the phases presented by Brown (Bro78) are derived from diagonal S-matrix elements of the above mentioned unitary matrix. This is equivalent to using the definition of Eq. (V.1) on the diagonal S-matrix elements, that are the results of the unitary transformation of Eq. (V.2).

Even when these qualifications are taken into account, it should be possible to make a comparison for elastic channels that are not mixed, such as the 1S_0 and 3P_0 wave. In the first case the agreement is poor and in the second case it is excellent. Also, the single energy phase shifts of two coupled elastic channels should have a larger difference in the two real phases than the results of the R-matrix analysis. For example, phases of the 1D_2 - and 3D_2 -waves would be larger than 15° in magnitude which is generally not found here.

Other aspects should be taken into account as well

a) the low energy R-matrix results (Hal74) are not continuous with the high energy R-matrix results.

b) the R-matrix analysis between 19 and 50 MeV uses only differential cross sections, proton analyzing powers, and total reaction cross sections. This is clearly an inadequate data set.

c) the high energy R-matrix analysis predicted that ^3He analyzing powers would vary between -0.6 and $+0.7$. The actual variations are between -0.3 and 0.4 .

The conclusion that can be drawn from the above is that the R-matrix analysis in this region is not yet complete. To rectify this situation an analysis should be done that includes all low energy data and also all polarization data beyond 19.5 MeV.

In summary, phase shifts for the proton- ^3He have been determined that produced good fits to the present data between 19.5 and 35 MeV. Some anomalies noted in previous analyses have been dealt with successfully.

VI. CONCLUSION AND RECOMMENDATIONS

A. ^3He Polarization

A polarized ^3He target has been built with a performance comparable to that of other targets using optical pumping with discharge light sources (Table 2.2). Possible causes of depolarization have been discussed with emphasis on relaxation in the presence of a weak discharge, and reabsorption of pumping light.

It has been shown in Sec. IV.C that the polarization measurement by fluorescence is sufficiently accurate with regards to its contribution to the stochastic error in the ^3He analyzing power. However, the normalization error in the polarization is not negligible. Further, it was found that the formula conventionally used for the interpretation of the fluorescence observation [Eq. (II.18)] gives a slight underestimate of the polarization. Due to finite pumping light absorption in the target cell a correction has to be applied that depends on the absorption factor [Eq. (II.21)].

If the ^3He analyzing powers need to be determined with a higher accuracy using the optical pumping technique for polarization then it is recommended that the polarization measurement be replaced by a probing beam technique, and that the absorption factor be determined independently. This will reduce the above mentioned normalization error. Work on this is in progress.

An increase in polarization, or better the product of polarization squared and density (see Table 2,2), can be achieved in two ways: by reducing depolarization effects, or increasing the pumping light intensity. With respect to the first approach, developments should be sought in reducing the discharge byproducts without affecting the triplet metastable atom density. One possibility is to investigate different discharge modulation techniques. The author is not aware of any systematic study in this direction, except that the Toronto group reported a decrease of polarization for modulation over 50% (May, private communication). An experiment was performed with a discharge pulsed at 100 Hz. A large range of metastable densities could be achieved by variation of pulse amplitude and pulse width. This would allow a better choice of discharge level for optimum polarization. However, the fluorescence technique of polarization measurement used so far, could not determine the polarization reliably when the discharge is pulsed.

Another line of approach is to look for alternative methods of metastable atom production. These might be accompanied by relatively less depolarization. One such possibility was tried: ionization by irradiation with a proton beam. However, no fluorescence could be detected with a 4 kPa target cell and a 170 nA proton beam at 30 MeV. This indicates that the metastable atom densities produced with this method are small.

An increase in polarization is also obtained by replacing the discharge lamps with a tuneable laser. In principle, any transition shown in Fig. 2.3 could be utilized for optical pumping. Tuning to transitions between singlet states is probably unproductive, because photon trapping in the vacuum UV should effectively quench any polarization. Within the group of triplet state transitions, absorption is strongest for the 1083 nm line, but it might still be worthwhile to test the possibility of optical pumping on the 389 nm line, because tuneable dye lasers are available in this region.

Within the 1083 nm line, there are several wavelengths at which optical pumping could be done. The transition from $2^3S_1; F=3/2$ to $2^3P_0; F=1/2$, also excited by ^4He discharge light, is still the most efficient (Appendix A, Fig. A.1).

A tuneable laser at 1083 nm has only recently been developed (Mol80) based on the use of colour centers in NaF. There are some reports on its use to polarize ^3He (Nac82, Cra83) or metastable ^4He (Gib82). For a nuclear scattering experiment, the major technical problem appears to be the long term intensity stability. A week of continuous operation appears now feasible (Dunning, private communication). A target polarized by laser light optical pumping, increases the efficiency of a nuclear scattering experiment by a factor of five (Table 2.2).

Sec. II.A also mentions a few alternative techniques for polarizing ^3He . Cryogenic methods (Cra83, Hee81) appear to be the most promising, but useable nuclear targets cannot be expected in the near future.

In short, the optical pumping technique still remains the only viable method of polarizing ^3He . Further development should be concentrated on a) the helium discharge characteristics, and b) the users of colour center lasers. A contribution to these two approaches is given by the formulas describing polarization kinematics (Sec. II.C) and the analyses presented in appendices A and B.

B. ^3He Analyzing Powers

The ^3He analyzing powers for angles between 30° and 100° ; and energies between 25 and 35 MeV are listed in Table 4.2. The consistency tests (Sec. IV.B) proved adequate to detect internal inconsistencies. Stochastic errors are mainly determined by counting statistics; the normalization error depends on the polarization determination.

Inclusion of the above mentioned data has proven to be useful in the phase shift analysis, especially with regard to the elastic channels that undergo singlet-triplet coupling parameters.

To complement the present set, it would be advisable to add ^3He analyzing power data at the back angles for energies of 30, 32.5, and 35 MeV, and to measure a complete angular distribution at 40 MeV.

It is also obvious from the phase shift analysis that differential cross sections, proton and ^3He analyzing powers are not sufficient to constrain the solution completely. A set of spin-correlation parameters, such as at 19.5 MeV (Bak71), would be required for this. One set at a higher energy, such as 30 MeV, would help to find a unique

solution for all intermediate energies. Measurements at even higher energies will be hampered by low count rates.

C. Phase Shift Analysis

The data analysis performed here, produced the following

- a) a more flexible and faster computer program, SHOSH2, to carry out single energy phase shift analysis
- b) phase shifts between 19.5 MeV and 35 MeV for the S-, P-, D-, F- and G-waves that are continuous in energy, and that start with the solution of Baker et al. (Bak71) at 19.5 MeV.
- c) the removal of some anomalies in the interpretation of previous phase shift analyses (Dar72, Mor75, Bro78, Mul78); in particular, the case of singlet-triplet mixing in elastic channels.

The results for the S- and P-waves are now well determined. In the D-waves an apparent discontinuity of the 1D_2 phase between 13 MeV and 20 MeV needs to be resolved by single energy phase shift analyses in this region. The real phases of the F- and G-waves are small, except for the 3F_3 partial wave.

To ascertain the uniqueness and to improve the accuracy, spin-correlation data are needed as mentioned in Sec. VI.B. Further, it is recommended that the differential cross sections be remeasured at the back angles between 32.4 MeV and 37.5 MeV.

The inelasticity parameters were not well determined. This ambiguity also affects the errors in the real phases. The total reaction cross section data were not sufficient to resolve this problem. It might be worthwhile to explore the possibility of including observations that are done on the ${}^3\text{He}(p,2p){}^2\text{H}$ and ${}^3\text{He}(p,3p)n$ reactions.

Phase shift analyses at higher energies should now be possible starting from the present results. The more interesting approach is to redo the R-matrix analysis with the full set of data up to 35 MeV. This might culminate in a "global" search involving all data on the A=4 system as already referred to by Baker et al. (Bak71).

APPENDIX A: OPTICAL PUMPING FROM THE TRIPLET METASTABLE STATE IN ^3He

Because it is possible to utilize any transition $2^3\text{S}_1\text{-}n^3\text{P}_{0,1,2}$, the formalism describing the polarization kinetics, needs to be generalized. This section contains the formulas for absorption and angular momentum transfer both with and without collision mixing in the P-state.

When circularly polarized light passes through ^3He -gas it can be absorbed by metastable atoms. These are so well coupled to the ground state that the distribution over the various magnetic substates is determined by the polarization of the ground state (Table A.1).

A photon induces a transition from an initial state with one out of two F-values to one out of five possible P-states: $^3\text{P}_0;F=1/2$, $^3\text{P}_1;F=1/2$, $^3\text{P}_1;F=3/2$, $^3\text{P}_2;F=3/2$ and $^3\text{P}_2;F=5/2$. The transition probabilities are determined by the details of the hyperfine structure. Timsit (Tim70) carried out a detailed analysis of the $2^3\text{S}_1\text{-}2^3\text{P}_{0,1,2}$ transition using perturbation theory. His table is reproduced here (Table A.2), but with a different parametrization through the use of two constants, e_1 and e_2 . In this manner the formulas apply to all triplet S-P transitions in ^3He . Substituting for these constants the values $e_1=-0.319$ and $e_2=-3.869$ leads to the same numerical results as Timsit (Tim70) for the $2^3\text{S}_1\text{-}2^3\text{P}_{0,1,2}$ transition.

We take it here that the absorbed circularly polarized light induces a transition with $\Delta m_F=+1$. Subsequently the atom decays from the intermediate P-state to any of the magnetic sublevels of the $^3\text{S}_1$ -state with the condition $\Delta m_F=-1, 0$ or $+1$. Table A.3 displays the possible 9

Table A.1. Densities of atoms in the magnetic sublevels of the metastable 2^3S_1 -state in equilibrium with polarized groundstate atoms.

F	m_F	density of atoms
$\frac{1}{2}$	$-\frac{1}{2}$	$\frac{n}{6} (1-P)^2 (1+P) / (1+\frac{1}{3}P^2)$
	$+\frac{1}{2}$	$\frac{n}{6} (1-P) (1+P)^2 / (1+\frac{1}{3}P^2)$
$\frac{3}{2}$	$-\frac{3}{2}$	$\frac{n}{6} (1-P)^3 / (1+\frac{1}{3}P^2)$
	$-\frac{1}{2}$	$\frac{n}{6} (1-P)^2 (1+P) / (1+\frac{1}{3}P^2)$
	$+\frac{1}{2}$	$\frac{n}{6} (1-P) (1+P)^2 / (1+\frac{1}{3}P^2)$
	$+\frac{3}{2}$	$\frac{n}{6} (1+P)^3 / (1+\frac{1}{3}P^2)$

Table A.2. Relative transition probabilities for absorption and emission between 3S_1 and $^3P_{0,1,2}$ states (adapted from Tim70).

		$^3S_1; F=\frac{1}{2}$			$^3S_1; F=\frac{3}{2}$		
F	m_F	$m_F = -\frac{1}{2}$	$+\frac{1}{2}$	$m_F = \frac{3}{2}$	$m_F = -\frac{1}{2}$	$m_F = +\frac{1}{2}$	$m_F = +\frac{3}{2}$
3P_0	$\frac{1}{2}$	$\frac{1}{9}(1-e_1)$	$\frac{2}{9}(1-e_1)$	$\frac{3}{18}(2+e_1)$	$\frac{2}{18}(2+e_1)$	$\frac{1}{18}(2+e_1)$	0
	$+\frac{1}{2}$	$\frac{2}{9}(1-e_1)$	$\frac{1}{9}(1-e_1)$	0	$\frac{1}{18}(2+e_1)$	$\frac{2}{18}(2+e_1)$	$\frac{3}{18}(2+e_1)$
3P_1	$\frac{1}{2}$	$\frac{1}{9}(2+e_1)$	$\frac{2}{9}(2+e_1)$	$\frac{3}{18}(1-e_1)$	$\frac{2}{18}(1-e_1)$	$\frac{1}{18}(1-e_1)$	0
	$+\frac{1}{2}$	$\frac{2}{9}(2+e_1)$	$\frac{1}{9}(2+e_1)$	0	$\frac{1}{18}(1-e_1)$	$\frac{2}{18}(1-e_1)$	$\frac{3}{18}(1-e_1)$
3P_1	$\frac{3}{2}$	$\frac{3}{2} \frac{15}{72}(\frac{4}{5}e_2)$	0	$\frac{9}{72}(4+e_2)$	$\frac{6}{72}(4+e_2)$	0	0
	$+\frac{1}{2}$	$\frac{10}{72}(\frac{4}{5}e_2)$	$\frac{5}{72}(\frac{4}{5}e_2)$	$\frac{6}{72}(4+e_2)$	$\frac{1}{72}(4+e_2)$	$\frac{8}{72}(4+e_2)$	0
	$+\frac{1}{2}$	$\frac{5}{72}(\frac{4}{5}e_2)$	$\frac{10}{72}(\frac{4}{5}e_2)$	0	$\frac{8}{72}(4+e_2)$	$\frac{1}{72}(4+e_2)$	$\frac{6}{72}(4+e_2)$
	$+\frac{3}{2}$	0	$\frac{15}{72}(\frac{4}{5}e_2)$	0	0	$\frac{6}{72}(4+e_2)$	$\frac{9}{72}(4+e_2)$
3P_2	$\frac{3}{2}$	$\frac{3}{2} \frac{15}{72}(4+e_2)$	0	$\frac{9}{72}(\frac{4}{5}e_2)$	$\frac{6}{72}(\frac{4}{5}e_2)$	0	0
	$+\frac{1}{2}$	$\frac{10}{72}(4+e_2)$	$\frac{5}{72}(4+e_2)$	$\frac{6}{72}(\frac{4}{5}e_2)$	$\frac{1}{72}(\frac{4}{5}e_2)$	$\frac{8}{72}(\frac{4}{5}e_2)$	0
	$+\frac{1}{2}$	$\frac{5}{72}(4+e_2)$	$\frac{10}{72}(4+e_2)$	0	$\frac{8}{72}(\frac{4}{5}e_2)$	$\frac{1}{72}(\frac{4}{5}e_2)$	$\frac{6}{72}(\frac{4}{5}e_2)$
	$+\frac{3}{2}$	0	$\frac{15}{72}(4+e_2)$	0	0	$\frac{6}{72}(\frac{4}{5}e_2)$	$\frac{9}{72}(\frac{4}{5}e_2)$
3P_2	$\frac{5}{2}$	$\frac{5}{2}$	0	0	1	0	0
	$\frac{3}{2}$	$\frac{3}{2}$	0	0	$\frac{4}{10}$	$\frac{6}{10}$	0
	$\frac{1}{2}$	$\frac{1}{2}$	0	0	$\frac{1}{10}$	$\frac{6}{10}$	$\frac{3}{10}$
	$+\frac{1}{2}$	$+\frac{1}{2}$	0	0	0	$\frac{3}{10}$	$\frac{6}{10}$
	$+\frac{3}{2}$	$+\frac{3}{2}$	0	0	0	0	$\frac{6}{10}$
	$+\frac{5}{2}$	$+\frac{5}{2}$	0	0	0	0	0

Table A.3. Possible modes of optical pumping from the 3S_1 -state in ^3He .

no	initial S-state		intermediate P-state			final S-state		absorption rate	emission rate	Δm total		
	F	m_F	J	F	m_F	F	m_F					
1.	$\frac{1}{2}$	$\frac{1}{2}$	0	$\frac{1}{2}$	$+\frac{1}{2}$	$\frac{1}{2}$	$\frac{1}{2}$	$\frac{4}{18}(1-e_1)$	$\frac{4}{18}(1-e_1)$	0		
						$\frac{1}{2}$	$+\frac{1}{2}$				$\frac{2}{18}(1-e_1)$	1
						$\frac{3}{2}$	$\frac{1}{2}$				$\frac{1}{18}(2+e_1)$	0
						$\frac{3}{2}$	$+\frac{1}{2}$				$\frac{2}{18}(2+e_1)$	1
						$\frac{3}{2}$	$+\frac{3}{2}$				$\frac{3}{18}(2+e_1)$	2
2.	$\frac{1}{2}$	$\frac{1}{2}$	1	$\frac{1}{2}$	$+\frac{1}{2}$	$\frac{1}{2}$	$\frac{1}{2}$	$\frac{4}{18}(2+e_1)$	$\frac{4}{18}(2+e_1)$	0		
						$\frac{1}{2}$	$+\frac{1}{2}$				$\frac{2}{18}(2+e_1)$	1
						$\frac{3}{2}$	$\frac{1}{2}$				$\frac{1}{18}(1-e_1)$	0
						$\frac{3}{2}$	$+\frac{1}{2}$				$\frac{2}{18}(1-e_1)$	1
						$\frac{3}{2}$	$+\frac{3}{2}$				$\frac{3}{18}(1-e_1)$	2
3.	$\frac{1}{2}$	$\frac{1}{2}$	1	$\frac{3}{2}$	$+\frac{1}{2}$	$\frac{1}{2}$	$\frac{1}{2}$	$\frac{5}{72}(\frac{4}{5}e_2)$	$\frac{5}{72}(\frac{4}{5}e_2)$	0		
						$\frac{1}{2}$	$+\frac{1}{2}$				$\frac{10}{72}(\frac{4}{5}e_2)$	1
						$\frac{3}{2}$	$\frac{1}{2}$				$\frac{8}{72}(4+e_2)$	0
						$\frac{3}{2}$	$+\frac{1}{2}$				$\frac{1}{72}(4+e_2)$	1
						$\frac{3}{2}$	$+\frac{3}{2}$				$\frac{6}{72}(4+e_2)$	2
	$\frac{1}{2}$	$+\frac{1}{2}$	1	$\frac{3}{2}$	$+\frac{3}{2}$	$\frac{1}{2}$	$+\frac{1}{2}$	$\frac{15}{72}(\frac{4}{5}e_2)$	$\frac{15}{72}(\frac{4}{5}e_2)$	0		
						$\frac{3}{2}$	$+\frac{1}{2}$				$\frac{6}{72}(4+e_2)$	0
						$\frac{3}{2}$	$+\frac{3}{2}$				$\frac{9}{72}(4+e_2)$	1

Table A.3. continued.

no	initial S-state		intermediate P-state			final S-state		absorption rate	emission rate	Δm total
	F	m_F	J	F	m_F	F	m_F			
4.	$\frac{1}{2}$	$-\frac{1}{2}$	2	$\frac{3}{2}$	$+\frac{1}{2}$	$\frac{1}{2}$	$-\frac{1}{2}$	$\frac{5}{72}(4+e_2)$	$\frac{5}{72}(4+e_2)$	0
						$\frac{1}{2}$	$+\frac{1}{2}$		$\frac{10}{72}(4+e_2)$	1
						$\frac{3}{2}$	$-\frac{1}{2}$		$\frac{8}{72}(\frac{4}{5}-e_2)$	0
						$\frac{3}{2}$	$+\frac{1}{2}$		$\frac{1}{72}(\frac{4}{5}-e_2)$	1
						$\frac{3}{2}$	$+\frac{3}{2}$		$\frac{6}{72}(\frac{4}{5}-e_2)$	2
	$\frac{1}{2}$	$+\frac{1}{2}$	2	$\frac{3}{2}$	$+\frac{3}{2}$	$\frac{1}{2}$	$+\frac{1}{2}$	$\frac{15}{72}(4+e_2)$	$\frac{15}{72}(4+e_2)$	0
						$\frac{3}{2}$	$+\frac{1}{2}$		$\frac{6}{72}(\frac{4}{5}-e_2)$	0
						$\frac{3}{2}$	$+\frac{3}{2}$		$\frac{9}{72}(\frac{4}{5}-e_2)$	1
5.	$\frac{3}{2}$	$-\frac{3}{2}$	0	$\frac{1}{2}$	$-\frac{1}{2}$	$\frac{1}{2}$	$-\frac{1}{2}$	$\frac{3}{18}(2+e_1)$	$\frac{2}{18}(1-e_1)$	1
						$\frac{1}{2}$	$+\frac{1}{2}$		$\frac{4}{18}(1-e_1)$	2
						$\frac{3}{2}$	$-\frac{3}{2}$		$\frac{3}{18}(2+e_1)$	0
						$\frac{3}{2}$	$-\frac{1}{2}$		$\frac{2}{18}(2+e_1)$	1
						$\frac{3}{2}$	$+\frac{1}{2}$		$\frac{1}{18}(2+e_1)$	2
	$\frac{3}{2}$	$-\frac{1}{2}$	0	$\frac{1}{2}$	$+\frac{1}{2}$	$\frac{1}{2}$	$-\frac{1}{2}$	$\frac{1}{18}(2+e_1)$	$\frac{4}{18}(1-e_1)$	0
						$\frac{1}{2}$	$+\frac{1}{2}$		$\frac{2}{18}(1-e_1)$	1
						$\frac{3}{2}$	$-\frac{1}{2}$		$\frac{1}{18}(2+e_1)$	0
						$\frac{3}{2}$	$+\frac{1}{2}$		$\frac{2}{18}(2+e_1)$	1
						$\frac{3}{2}$	$+\frac{3}{2}$		$\frac{3}{18}(2+e_1)$	2

Table A.3. continued.

no	initial S-state		intermediate P-state J	intermediate P-state		final S-state		absorption rate	emission rate	Δm total						
	F	m_F		F	m_F	F	m_F									
6.	$\frac{3}{2}$	$-\frac{3}{2}$	1	$\frac{1}{2}$	$-\frac{1}{2}$	$\frac{1}{2}$	$-\frac{1}{2}$	$\frac{3}{18}(1-e_1)$	$\frac{2}{18}(2+e_1)$	1						
						$\frac{1}{2}$	$+\frac{1}{2}$				$\frac{4}{18}(2+e_1)$	2				
						$\frac{3}{2}$	$-\frac{3}{2}$						$\frac{3}{18}(1-e_1)$	0		
						$\frac{3}{2}$	$-\frac{1}{2}$								$\frac{2}{18}(1-e_1)$	1
						$\frac{3}{2}$	$+\frac{1}{2}$									
	$\frac{3}{2}$	$-\frac{1}{2}$	1	$\frac{1}{2}$	$+\frac{1}{2}$	$\frac{1}{2}$	$-\frac{1}{2}$	$\frac{1}{18}(1-e_1)$	$\frac{4}{18}(2+e_1)$	0						
						$\frac{1}{2}$	$+\frac{1}{2}$				$\frac{2}{18}(2+e_1)$	1				
						$\frac{3}{2}$	$-\frac{1}{2}$						$\frac{1}{18}(1-e_1)$	0		
						$\frac{3}{2}$	$+\frac{1}{2}$								$\frac{2}{18}(1-e_1)$	1
						$\frac{3}{2}$	$+\frac{3}{2}$									
7.	$\frac{3}{2}$	$-\frac{3}{2}$	1	$\frac{3}{2}$	$-\frac{1}{2}$	$\frac{1}{2}$	$-\frac{1}{2}$	$\frac{6}{72}(4+e_2)$	$\frac{10}{72}(\frac{4}{5}-e_2)$	1						
						$\frac{1}{2}$	$+\frac{1}{2}$				$\frac{5}{72}(\frac{4}{5}-e_2)$	2				
						$\frac{3}{2}$	$-\frac{3}{2}$						$\frac{6}{72}(4+e_2)$	0		
						$\frac{3}{2}$	$-\frac{1}{2}$								$\frac{1}{72}(4+e_2)$	1
						$\frac{3}{2}$	$+\frac{1}{2}$									
	$\frac{3}{2}$	$-\frac{1}{2}$	1	$\frac{3}{2}$	$+\frac{1}{2}$	$\frac{1}{2}$	$-\frac{1}{2}$	$\frac{8}{72}(4+e_2)$	$\frac{5}{72}(\frac{4}{5}-e_2)$	0						
						$\frac{1}{2}$	$+\frac{1}{2}$				$\frac{10}{72}(\frac{4}{5}-e_2)$	1				
						$\frac{3}{2}$	$-\frac{1}{2}$						$\frac{8}{72}(4+e_2)$	0		
						$\frac{3}{2}$	$+\frac{1}{2}$								$\frac{1}{72}(4+e_2)$	1
						$\frac{3}{2}$	$+\frac{3}{2}$									

Table A.3. continued.

no	initial S-state		intermediate P-state		final S-state		absorption rate	emission rate	Δm total	
	F	m_F	J	F	m_F	F				m_F
7. cont.	$\frac{3}{2}$	$+\frac{1}{2}$	1	$\frac{3}{2}$	$+\frac{3}{2}$	$\frac{1}{2}$	$+\frac{1}{2}$	$\frac{6}{72}(4+e_2)$	$\frac{15}{72}(\frac{4}{5}-e_2)$	0
						$\frac{3}{2}$	$+\frac{1}{2}$		$\frac{6}{72}(4+e_2)$	0
						$\frac{3}{2}$	$+\frac{3}{2}$		$\frac{9}{72}(4+e_2)$	1
8.	$\frac{3}{2}$	$-\frac{3}{2}$	2	$\frac{3}{2}$	$-\frac{1}{2}$	$\frac{1}{2}$	$-\frac{1}{2}$	$\frac{6}{72}(\frac{4}{5}-e_2)$	$\frac{10}{72}(4+e_2)$	1
						$\frac{1}{2}$	$+\frac{1}{2}$		$\frac{5}{72}(4+e_2)$	2
						$\frac{3}{2}$	$-\frac{3}{2}$		$\frac{6}{72}(\frac{4}{5}-e_2)$	0
						$\frac{3}{2}$	$-\frac{1}{2}$		$\frac{1}{72}(\frac{4}{5}-e_2)$	1
						$\frac{3}{2}$	$+\frac{1}{2}$		$\frac{8}{72}(\frac{4}{5}-e_2)$	2
$\frac{3}{2}$	$-\frac{1}{2}$	2	$\frac{3}{2}$	$+\frac{1}{2}$	$\frac{1}{2}$	$-\frac{1}{2}$	$\frac{8}{72}(\frac{4}{5}-e_2)$	$\frac{5}{72}(4+e_2)$	0	
					$\frac{1}{2}$	$+\frac{1}{2}$		$\frac{10}{72}(4+e_2)$	1	
					$\frac{3}{2}$	$-\frac{1}{2}$		$\frac{8}{72}(\frac{4}{5}-e_2)$	0	
					$\frac{3}{2}$	$+\frac{1}{2}$		$\frac{1}{72}(\frac{4}{5}-e_2)$	1	
					$\frac{3}{2}$	$+\frac{3}{2}$		$\frac{6}{72}(\frac{4}{5}-e_2)$	2	
$\frac{3}{2}$	$+\frac{1}{2}$	2	$\frac{3}{2}$	$+\frac{3}{2}$	$\frac{1}{2}$	$+\frac{1}{2}$	$\frac{6}{72}(\frac{4}{5}-e_2)$	$\frac{15}{72}(4+e_2)$	0	
					$\frac{3}{2}$	$+\frac{1}{2}$		$\frac{6}{72}(\frac{4}{5}-e_2)$	0	
					$\frac{3}{2}$	$+\frac{3}{2}$		$\frac{9}{72}(\frac{4}{5}-e_2)$	1	

Table A.3. continued.

no	initial S-state		J	intermediate P-state		final S-state		absorption rate	emission rate	Δm total
	F	m_F		F	m_F	F	m_F			
9.	$\frac{3}{2}$	$-\frac{3}{2}$	2	$\frac{5}{2}$	$-\frac{1}{2}$	$\frac{3}{2}$	$-\frac{3}{2}$	$\frac{1}{10}$	$\frac{1}{10}$	0
						$\frac{3}{2}$	$-\frac{1}{2}$		$\frac{6}{10}$	1
						$\frac{3}{2}$	$+\frac{1}{2}$		$\frac{3}{10}$	2
	$\frac{3}{2}$	$-\frac{1}{2}$	2	$\frac{5}{2}$	$+\frac{1}{2}$	$\frac{3}{2}$	$-\frac{1}{2}$	$\frac{3}{10}$	$\frac{3}{10}$	0
						$\frac{3}{2}$	$+\frac{1}{2}$		$\frac{6}{10}$	1
						$\frac{3}{2}$	$+\frac{3}{2}$		$\frac{1}{10}$	2
	$\frac{3}{2}$	$+\frac{1}{2}$	2	$\frac{5}{2}$	$+\frac{3}{2}$	$\frac{3}{2}$	$+\frac{1}{2}$	$\frac{6}{10}$	$\frac{6}{10}$	0
						$\frac{3}{2}$	$+\frac{3}{2}$		$\frac{4}{10}$	1
	$\frac{3}{2}$	$+\frac{3}{2}$	2	$\frac{5}{2}$	$+\frac{5}{2}$	$\frac{3}{2}$	$+\frac{3}{2}$	1	$\frac{1}{10}$	0

modes with different energies. Each mode consists of 5 to 13 different branches. From Tables A.1 to A.3 the polarization dependence of the various properties can be calculated.

The absorption rate follows from multiplying the metastable atom density of each magnetic sublevel (Table A.1) with the transition probability for excitation (Table A.3, column 5). The results, $I(P)$, are presented in Table A.4. The normalization is such that the sum over all 9 modes equals unity. In this manner the photoabsorption cross section for photons in a particular mode is $\sigma I(P)$, where σ is the combined cross section. The last column in Table A.4 is relevant to the interpretation of polarization measurements by absorption or fluorescence.

Because the transition probabilities of each branch in the process of absorption and reemission are known (Tables A.2 and A.3), the average angular momentum transferred to the system can be calculated. This results in the two functions, $T_A(P)$ and $T_R(P)$ (Table A.5), for respectively the case with complete collision mixing and the case without collision mixing.

An application is the expected performance of pumping light sources with respect to their efficiency of transferring angular momentum to the spin system, which is proportional to

$$\sum_{i=1}^9 \alpha_i I_i(P) [T_{Ai}(P)u + T_{Ri}(P)(1-u)], \quad (A.1)$$

where

Table A.4. Absorption rate, $I(P)$, of circularly polarized light as a function of the polarization.

no	mode	$I(0)$	$I(P)/I(0)$	$1-I(P)/I(0)$
1.	$F=\frac{1}{2}$ ${}^3P_0; F=\frac{1}{2}$	$\frac{1}{27}(1-e_1)$	$\frac{(1-P)^2(1+P)}{1+\frac{1}{3}P^2}$	$P \frac{1+\frac{4}{3}P-P^2}{1+\frac{1}{3}P^2}$
2.	$F=\frac{1}{2}$ ${}^3P_1; F=\frac{1}{2}$	$\frac{1}{27}(2+e_1)$		
3.	$F=\frac{1}{2}$ ${}^3P_1; F=\frac{3}{2}$	$\frac{5}{108}(\frac{4}{5}-e_2)$	$\frac{(1-P^2)(1+\frac{1}{2}P)}{1+\frac{1}{3}P^2}$	$-\frac{1}{2}P \frac{1-\frac{8}{3}P-P^2}{1+\frac{1}{3}P^2}$
4.	$F=\frac{1}{2}$ ${}^3P_2; F=\frac{3}{2}$	$\frac{5}{108}(4+e_2)$		
5.	$F=\frac{3}{2}$ ${}^3P_0; F=\frac{1}{2}$	$\frac{1}{27}(2+e_1)$	$\frac{(1-P)^2(1-\frac{1}{2}P)}{1+\frac{1}{3}P^2}$	$\frac{5}{2}P \frac{1-\frac{2}{3}P+\frac{1}{5}P^2}{1+\frac{1}{3}P^2}$
6.	$F=\frac{3}{2}$ ${}^3P_1; F=\frac{1}{2}$	$\frac{1}{27}(1-e_1)$		
7.	$F=\frac{3}{2}$ ${}^3P_1; F=\frac{3}{2}$	$\frac{5}{108}(4+e_2)$	$\frac{(1-P)(1+\frac{1}{5}P^2)}{1+\frac{1}{3}P^2}$	$P \frac{1+\frac{2}{15}P+\frac{1}{5}P^2}{1+\frac{1}{3}P^2}$
8.	$F=\frac{3}{2}$ ${}^3P_2; F=\frac{3}{2}$	$\frac{5}{108}(\frac{4}{5}-e_2)$		
9.	$F=\frac{3}{2}$ ${}^3P_2; F=\frac{5}{2}$	$\frac{1}{3}$	$\frac{1+\frac{3}{2}P+\frac{6}{5}P^2+\frac{3}{10}P^3}{1+\frac{1}{3}P^2}$	$-\frac{3}{2}P \frac{1+\frac{26}{45}P+\frac{1}{5}P^2}{1+\frac{1}{3}P^2}$

Table A.5. Net angular momentum transfer rates in units h per absorbed photon.

mode no.	transfer rate for absorption only $[T_A(P)]$	transfer rate for absorption and reemission $[T_R(P)]$
1.	$\frac{1}{2}$	$1 + \frac{1}{3}e_1$
2.	$\frac{1}{2}$	$\frac{2}{3} - \frac{1}{3}e_1$
3.	$-\frac{1}{4} \frac{1+2P}{1+\frac{1}{2}P}$	$\frac{(\frac{7}{12} + \frac{5}{48}e_2) + (\frac{1}{6} + \frac{1}{12}e_2)P}{1 + \frac{1}{2}P}$
4.	$-\frac{1}{4} \frac{1+2P}{1+\frac{1}{2}P}$	$\frac{(\frac{1}{4} - \frac{5}{48}e_2) - (\frac{1}{10} + \frac{1}{12}e_2)P}{1 + \frac{1}{2}P}$
5.	$\frac{5}{4} \frac{1 - \frac{4}{5}P}{1 - \frac{1}{2}P}$	$\frac{(1 - \frac{1}{6}e_1) - (\frac{1}{2} - \frac{1}{3}e_1)P}{1 - \frac{1}{2}P}$
6.	$\frac{5}{4} \frac{1 - \frac{4}{5}P}{1 - \frac{1}{2}P}$	$\frac{(\frac{7}{6} + \frac{1}{6}e_1) - (\frac{5}{6} + \frac{1}{3}e_1)P}{1 - \frac{1}{2}P}$
7.	$\frac{1}{2} \frac{1 - \frac{12}{5}P + \frac{1}{5}P^2}{1 + \frac{1}{5}P^2}$	$\frac{(\frac{5}{6} + \frac{1}{24}e_2) - (\frac{2}{5} - \frac{1}{10}e_2)P + (\frac{1}{6} + \frac{1}{120}e_2)P^2}{1 + \frac{1}{5}P^2}$
8.	$\frac{1}{2} \frac{1 - \frac{12}{5}P + \frac{1}{5}P^2}{1 + \frac{1}{5}P^2}$	$\frac{(\frac{7}{10} - \frac{1}{24}e_2) - (\frac{18}{25} + \frac{1}{10}e_2)P + (\frac{7}{50} - \frac{1}{120}e_2)P^2}{1 + \frac{1}{5}P^2}$
9.	$-\frac{3}{4} \frac{1 + \frac{18}{5}P + \frac{13}{5}P^2 + \frac{4}{5}P^3}{1 + \frac{3}{2}P + \frac{6}{5}P^2 + \frac{3}{10}P^3}$	$\frac{\frac{3}{10} - \frac{9}{50}P - \frac{3}{50}P^2 - \frac{3}{50}P^3}{1 + \frac{3}{2}P + \frac{6}{5}P^2 + \frac{3}{10}P^3}$

α_i = relative amplitude of the source light to excite mode i ,

u = collision mixing factor (Eq. II.10), and

the subscript i counts the nine modes.

As will be shown in Appendix B, there are 5 different energies at which photons are absorbed (Table B.1). So a laser could be tuned to any of these five and it can be evaluated with Eq. (A.1) that the most useful energies are D5 and D3 (Fig. A.1). A similar analysis can be done for the comparison of an ^4He -lamp with an ^3He -lamp (Fig. A.2). Although an ^3He -lamp has a higher angular momentum transfer rate at the lower pressures ($u=0$), it actually removes angular momentum out of the system at the higher pressures. This is confirmed by previous experiments (Col63), which show that an ^4He -lamp is more efficient above 0.04 kPa (0.3 Torr or $u=0.6$).

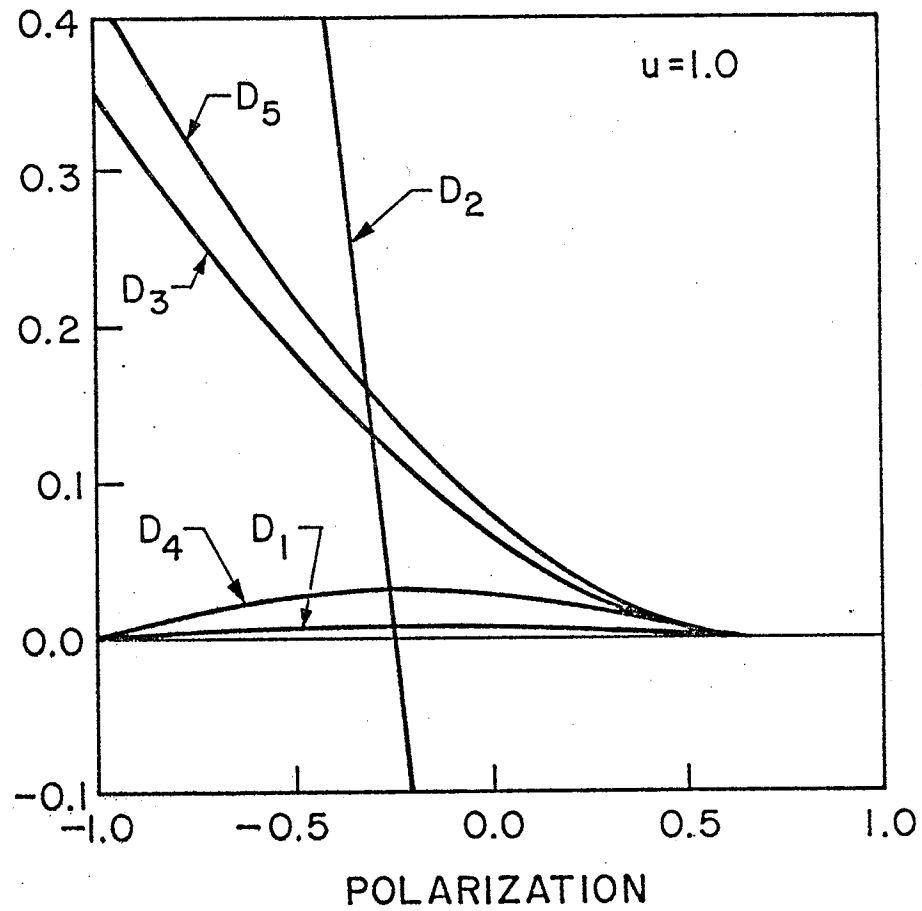
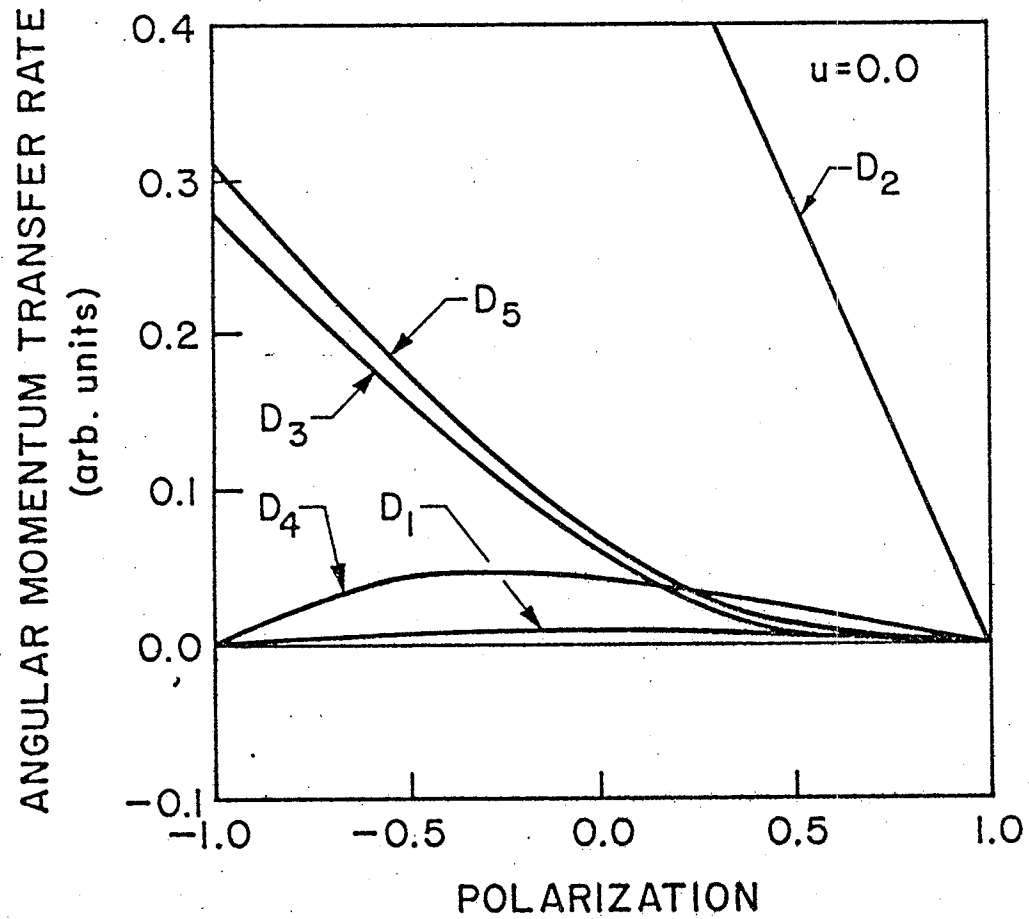
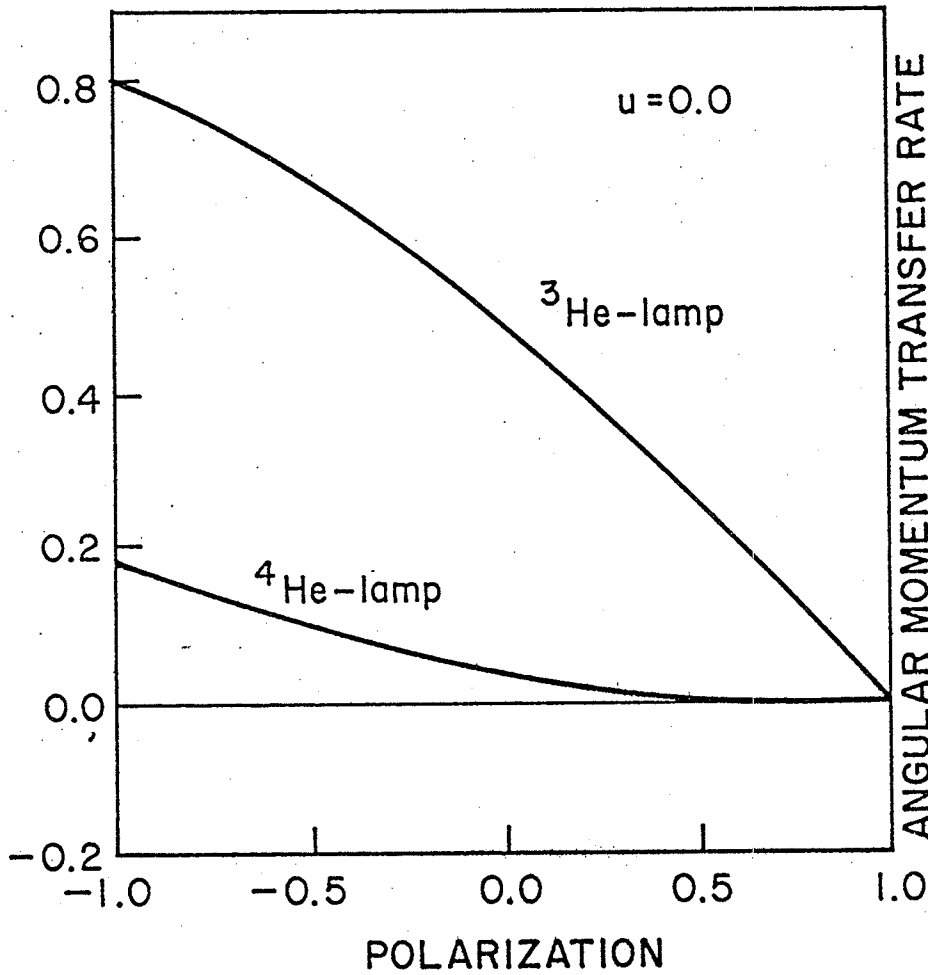


FIG. A.1 Comparison of optical pumping efficiency with a laser tuned to either of five lines at minimum and at maximum collision mixing.

ANGULAR MOMENTUM TRANSFER RATE
(arb. units)



ANGULAR MOMENTUM TRANSFER RATE
(arb. units)

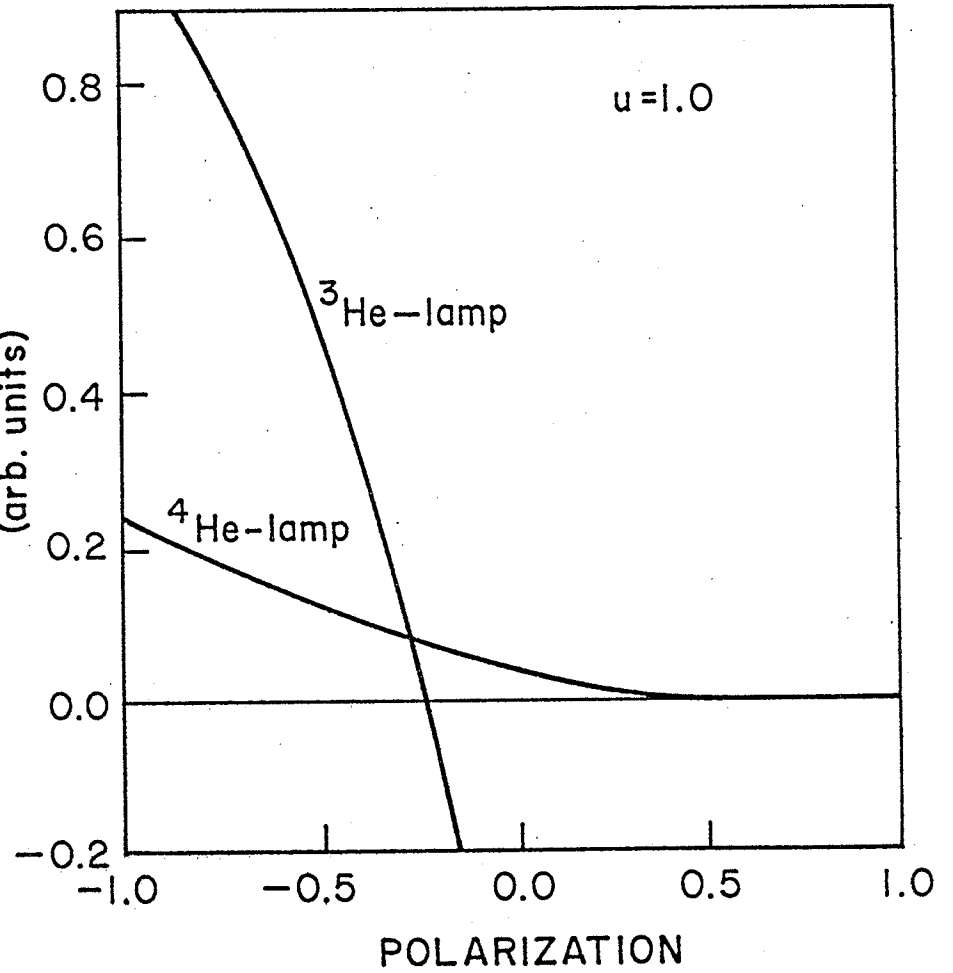


FIG. A.2 Comparison of optical pumping efficiency with an ^3He - and an ^4He -lamp at minimum and at maximum collision mixing.

APPENDIX B: ESTIMATION OF THE REABSORPTION FACTOR

After the absorption of pumping light in a cell filled with ^3He , the reemitted light can be absorbed again by the metastable atoms. Because this light has a random direction and no polarization each such absorption depolarizes the system. It is the number of such interactions per absorbed photon that appears in Eq. (II.1) describing the polarization rate and that is here called the reabsorption factor. The aim of this section is to find a numerical estimate for this factor. Previously (Phe58), a quantitative analysis was done to estimate the influence of radiation imprisonment on the effective lifetime of excited states in the decay of singlet P-states.

In the interaction processes of photons with metastable atoms all nine modes of the $2^3\text{S}-2^3\text{P}$ transition will occur, because collision mixing of the excited P-state causes the atom to decay along all possible modes. However, some transition modes have energies less than a linewidth apart and should therefore be considered as one group. The measurements of Timsit and May (Tim72) show that five such groups can be identified (Fig. B.1) with one to four modes constituting a photon group. These groups are designated here as D_1 to D_5 (Table B.1) and they will be referred to with the index k .

Similarly, there are five excited states: $2^3\text{P}_0;F=1/2$, $2^3\text{P}_1;F=1/2$, $2^3\text{P}_1;F=3/2$, $2^3\text{P}_2;F=3/2$, and $2^3\text{P}_2;F=5/2$. To facilitate easy reference, these will be numbered from 1 to 5 with the index l .

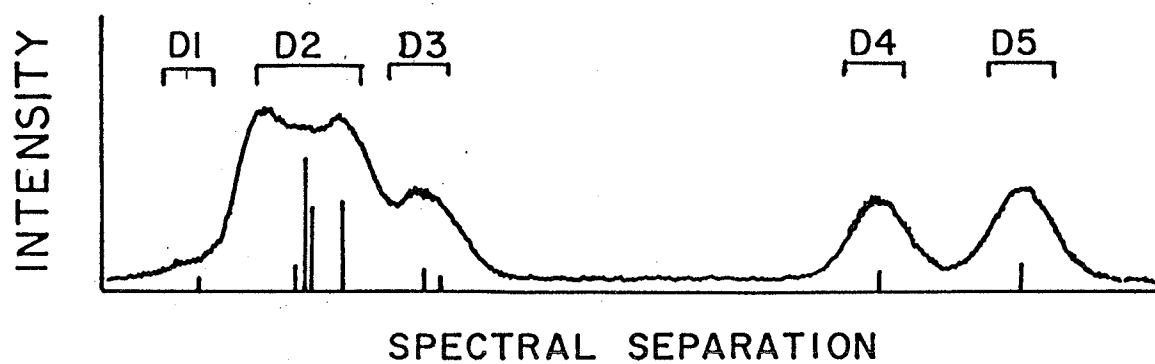


FIG. B.1 Spectral profile of the $2^3S - 2^3P$ transition in ^3He (after Tim72) showing the division in groups adopted here.

Table B.1. Grouping of $2^3S - 2^3P$ transitions that are less than one linewidth apart.

Group	Transitions	Relative amplitude in the emission spectrum after Timsit and May (Tim72)	
D1	$^3S_1; F=\frac{1}{2}$ $^3P_2; F=\frac{3}{2}$	0.0061	0.0061
D2	$^3S_1; F=\frac{1}{2}$ $^3P_1; F=\frac{1}{2}$	0.0623	
	$^3S_1; F=\frac{1}{2}$ $^3P_1; F=\frac{3}{2}$	0.2162	0.8279
	$^3S_1; F=\frac{3}{2}$ $^3P_2; F=\frac{3}{2}$	0.2162	
	$^3S_1; F=\frac{3}{2}$ $^3P_2; F=\frac{5}{2}$	0.3333	
D3	$^3S_1; F=\frac{3}{2}$ $^3P_1; F=\frac{1}{2}$	0.0489	0.0549
	$^3S_1; F=\frac{3}{2}$ $^3P_1; F=\frac{3}{2}$	0.0061	
D4	$^3S_1; F=\frac{1}{2}$ $^3P_0; F=\frac{1}{2}$	0.0489	0.0489
D5	$^3S_1; F=\frac{3}{2}$ $^3P_0; F=\frac{1}{2}$	0.0623	0.0623

Interactions of photons with the metastable atoms is through radiative absorption. When the photon density, ϕ_k , and the metastable atom density, n , are known, then the interaction rate per unit volume for transitions starting from $^3S_1; F=1/2$ or $F=3/2$ is given by

$$\frac{2F+1}{6} n \sigma \phi_k c A_{F\ell} \quad (\text{B.1})$$

where

c = velocity of light (in ms^{-1}),

σ = total photoabsorption cross section, and

$A_{F\ell}$ = relative absorption probability (Table B.2).

The relative absorption probabilities are obtained from Table A.2 by weighted summation over all possible branches for absorption of unpolarized light.

The atoms then appear in any of five excited states, whereby the endpoint is determined by the absorption mode. This P-state atom decays radiatively with a decay time, τ_e ($=105$ ns, Lif65) causing a loss rate out of the excited atom density, N_ℓ , which equals

$$\frac{N_\ell}{\tau_e} \quad (\text{B.2})$$

This is associated with the emission of a photon leading to a photon production rate of

$$E_{F\ell} \frac{N_\ell}{\tau_e} \quad (\text{B.3})$$

depending on the endpoint of the decay i.e. the $^3S_1; F=1/2$ or $F=3/2$ state. The relative emission probabilities, $E_{F\ell}$ (Table B.2), are also obtained from Table A.2 by appropriate summation over all possible branches for emission.

Besides radiative emission an excited P-state atom undergoes thermal collisions resulting in another loss term for the P-state atom density

$$\frac{N_\ell}{\tau_c} \tag{B.4}$$

where τ_c is the collision time. Because the energies exchanged in thermal collisions are small compared to the energy difference between the 2^3P -state and any other excited state, the result of collision mixing is that the atoms redistribute over all 18 2^3P -states according to the degeneracy, $2F+1$, of each state. Consequently each P-state is repopulated at a rate of

$$C_\ell \frac{\sum_{\ell'} N_{\ell'}}{\tau_c} \tag{B.5}$$

where

C_1 and $C_2 = 2/18$ i.e. the states with $F=1/2$,

C_3 and $C_4 = 4/18$ i.e. the states with $F=3/2$, and

$C_5 = 6/18$ i.e. the state with $F=5/2$.

Thus the primarily emitted photons cause a series of processes described by Eqs. (B.1) to (B.5) until a photon escapes from the gas cell. In the case that the number of reabsorptions per primary photon is small

Table B.2. Relative absorption and emission probabilities for unpolarized light matching 2^3S-2^3P transitions.

P-state	1	Rel. abs. prob. A_{F1}		Rel. emission prob. E_{F1}	
		S	P	P	S
		$2^3S_1; F=\frac{1}{2}$	$2^3S_1; F=\frac{3}{2}$	$2^3S_1; F=\frac{1}{2}$	$2^3S_1; F=\frac{3}{2}$
$2^3P_0; F=\frac{1}{2}$	1	$\frac{1}{9}(1-e_1)$	$\frac{1}{18}(2+e_1)$	$\frac{1}{3}(1-e_1)$	$\frac{1}{3}(2+e_1)$
$2^3P_1; F=\frac{1}{2}$	2	$\frac{1}{9}(2+e_1)$	$\frac{1}{18}(1-e_1)$	$\frac{1}{3}(2+e_1)$	$\frac{1}{3}(1-e_1)$
$2^3P_1; F=\frac{3}{2}$	3	$\frac{10}{72}(\frac{4}{5}e_2)$	$\frac{5}{72}(4+e_2)$	$\frac{15}{72}(\frac{4}{5}e_2)$	$\frac{15}{72}(4+e_2)$
$2^3P_2; F=\frac{3}{2}$	4	$\frac{10}{72}(4+e_2)$	$\frac{5}{72}(\frac{4}{5}e_2)$	$\frac{15}{72}(4+e_2)$	$\frac{15}{72}(\frac{4}{5}e_2)$
$2^3P_2; F=\frac{5}{2}$	5	0	$\frac{1}{2}$	0	1

compared to unity, the spatial variation of the densities N_{ℓ} and ϕ_k will be limited and they can be considered as being constant throughout the cell. The photon flux of group D_k everywhere in the gas cell is then $c\phi_k$. On the surface, S_c , of the cell half the flux is directed outwardly and escapes. The loss rate per unit volume is given by

$$\frac{1}{2} \frac{S_c c \phi_k}{V_c} \quad (\text{B.6})$$

where V_c is the the total cell volume. For a spherical cell with radius R this is

$$\frac{3}{2} \frac{c}{R} \phi_k \quad (\text{B.7})$$

As most of our cells are spherical or nearly spherical, and Eq. (B.6) is also an approximation, for computational simplicity we use Eq. (B.7) rather than Eq. (B.6), whereby the radius R could be redefined for each cell shape to be a characteristic dimension.

So far no term has been included to describe the primary source of the radiation in the system. In the case of optical pumping with an external ^4He light source, the pumping process produces excited atoms in the $^3\text{P}_0$ -state ($\ell=1$), so that this could be described with a single source term, S_1 , being the production rate for the $^3\text{P}_0$ -atoms per unit volume. In order to include other processes this can be generalized by defining

$$\left(\frac{dN_\ell}{dt}\right)_{\text{source}} = S_\ell \quad (\text{B.8})$$

as the production rate per unit volume of excited atoms in state ℓ .

Examples of other processes are the optical pumping with an ^4He -lamp and the occurrence of discharge-produced P-states.

The rates of change in the excited atom densities, dN_ℓ/dt , and the photon densities, $d\phi_k/dt$, can now be calculated. To find dN_ℓ/dt for each P-state the production terms [Eqs. (B.1), (B.5), and (B.8)] are added and the loss terms [Eqs. (B.2) and (B.4)] are subtracted. The results for each P-state are

$$\begin{aligned} \frac{dN_1}{dt} = & \frac{n\sigma c}{3} A_{1/2,1} \phi_4 + \frac{2n\sigma c}{3} A_{3/2,1} \phi_5 - \frac{N_1}{\tau_e} - \frac{N_1}{\tau_c} \\ & + \frac{1}{9\tau_c} (N_1 + N_2 + N_3 + N_4 + N_5) + S_1 \end{aligned} \quad (\text{B.9})$$

$$\begin{aligned} \frac{dN_2}{dt} = & \frac{n\sigma c}{3} A_{1/2,2} \phi_2 + \frac{2n\sigma c}{3} A_{3/2,2} \phi_3 \\ & - \frac{N_2}{\tau_e} - \frac{N_2}{\tau_c} + \frac{1}{9\tau_c} (N_1 + N_2 + N_3 + N_4 + N_5) + S_2 \end{aligned} \quad (\text{B.10})$$

$$\frac{dN_3}{dt} = \frac{n\sigma c}{3} A_{1/2,3} \phi_2 + \frac{2n\sigma c}{3} A_{3/2,3} \phi_3 \quad (\text{B.11})$$

$$- \frac{N_3}{\tau_e} - \frac{N_3}{\tau_c} + \frac{2}{4\tau_c} (N_1 + N_2 + N_3 + N_4 + N_5) + S_3$$

$$\frac{dN_4}{dt} = \frac{n\sigma c}{3} A_{1/2,4} \phi_1 + \frac{2n\sigma c}{3} A_{3/2,4} \phi_2 \quad (\text{B.12})$$

$$- \frac{N_4}{\tau_e} - \frac{N_4}{\tau_c} + \frac{2}{9\tau_c} (N_1 + N_2 + N_3 + N_4 + N_5) + S_4$$

$$\frac{dN_5}{dt} = \frac{2n\sigma c}{3} A_{3/2,5} \phi_2 \quad (\text{B.13})$$

$$- \frac{N_5}{\tau_e} - \frac{N_5}{\tau_c} - \frac{3}{9\tau_c} (N_1 + N_2 + N_3 + N_4 + N_5) + S_5$$

Similarly $d\phi_k/dt$ is calculated from Eqs. (B.1), (B.3) and (B.7)

$$\frac{d\phi_1}{dt} = \frac{E_{1/2,4}}{\tau_e} N_4 - \frac{n\sigma c}{3} A_{1/2,4} \phi_1 - \frac{3c}{2R} \phi_1 \quad (\text{B.14})$$

$$\begin{aligned} \frac{d\phi_2}{dt} = & \frac{E_{1/2,2}}{\tau_e} N_2 + \frac{E_{1/2,3}}{\tau_e} N_3 + \frac{E_{3/2,4}}{\tau_e} N_4 + \frac{E_{3/2,5}}{\tau_e} N_5 \\ & - \frac{n\sigma c}{3} A_{1/2,2} \phi_2 - \frac{n\sigma c}{3} A_{1/2,3} \phi_2 - \frac{2n\sigma c}{3} A_{3/2,4} \phi_2 \\ & - \frac{2n\phi c}{3} A_{3/2,5} \phi_5 - \frac{3c}{2R} \phi_2 \end{aligned} \quad (\text{B.15})$$

$$\frac{d\phi_3}{dt} = \frac{E_{3/2,2}}{\tau_e} N_2 + \frac{E_{3/2,3}}{\tau_e} N_3 - \frac{2n\sigma c}{3} A_{3/2,2} \phi_3 - \frac{2n\sigma c}{3} A_{3/2,3} \phi_3 - \frac{3c}{2R} \phi_3 \quad (\text{B.16})$$

$$\frac{d\phi_4}{dt} = \frac{E_{1/2,1}}{\tau_e} N_1 - \frac{n\sigma c}{3} A_{1/2,1} \phi_4 - \frac{3c}{2R} \phi_4 \quad (\text{B.17})$$

$$\frac{d\phi_5}{dt} = \frac{E_{3/2,1}}{\tau_e} N_1 - \frac{2n\sigma c}{3} A_{3/2,1} \phi_5 - \frac{3c}{2R} \phi_5 \quad (\text{B.18})$$

In the stationary state all derivatives with respect to time are set to zero and the above reduces to ten linear equations in N_ℓ and ϕ_k , which are solvable for any given set of values for S_1 .

The number of reabsorptions per primary photon can now be calculated. It is equal to the ratio of the total number of absorption processes over the total number of absorbed primary photons.

Consequently, the reabsorption factor r_0 is

$$r_0 = \frac{\sum_{k,F} \left[\frac{(2F+1)}{6} A_{F\ell} n\sigma c \phi_k \right]}{\sum_{\ell} S_{\ell}} \quad (\text{B.19})$$

An analysis of Eqs. (B.9) to (B.18) shows that given the values of Table B.2, the reabsorption factor is a function only of $n\sigma R$, the ratio τ_e/τ_c , and the relative distribution of the source terms S_1 . To use the same formalism as in chapter II these parameters are related to previously defined variables: a_n , the absorption factor for ^4He pumping light, and u , the collision mixing probability

$$a_n = n\sigma_o R \approx n \left(\frac{2}{3} A_{3/2,1} \sigma \right) R \quad (\text{B.20})$$

$$u = \frac{\tau_e}{\tau_e + \tau_c} \quad (\text{B.21})$$

So for each distribution of source terms the reabsorption factor, r_0 , can be calculated as a function of a_n and u .

The stationary state solution of Eqs. (B.9) to (B.18) has been obtained for the case of optical pumping with an ^4He -light source (Fig. B.2). At small values of the absorption, r_0 is nearly linear in a_n and u

$$r_0 \approx a_n (0.75 + 5.98u) \text{ for } a_n < 0.2 \quad (\text{B.22})$$

Also the solution has been evaluated for optical pumping with an ^3He -lamp. The values of S_λ are calculated from the relative emission and absorption probabilities (Table B.2). For small values of a_n

$$r_0 \approx a_n (8.03 - 1.47u) \text{ for } a_n < 0.2 \quad (\text{B.23})$$

Finally, r_0 has been calculated for photons produced in the weak discharge itself. Here the source terms S_λ reflect the random nature of excited P-state atom production, which is proportional to the magnitude of the constants C_1 in Eq. (B.5). In this case

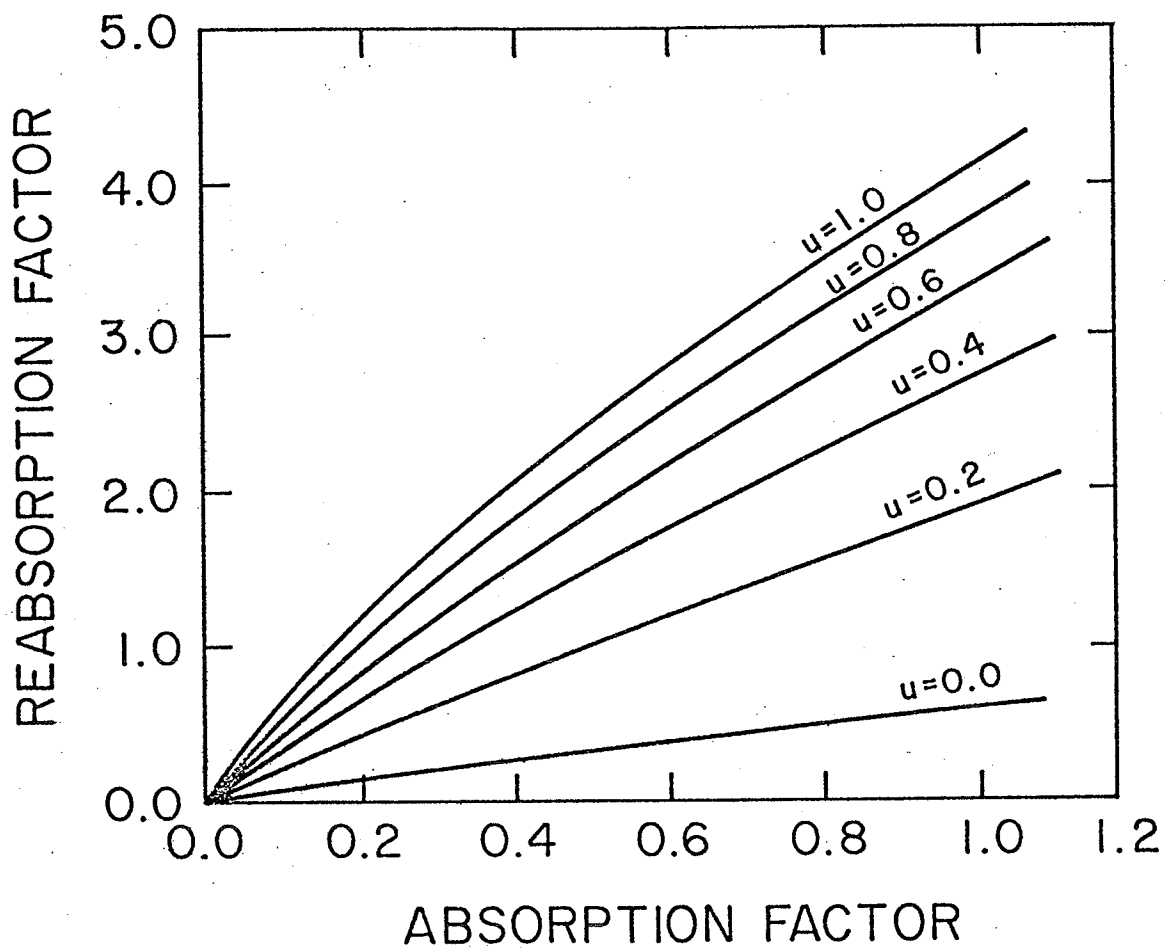


FIG. B.2 Reabsorption factor as a function of the absorption factor for pumping light from an ^4He -lamp at different values of the collision mixing probability.

$$r_{on} \approx a_n (7.14 - 0.57u) \text{ for } a_n < 0.2 \quad (\text{B.24})$$

It is noteworthy that apparently the reabsorption associated with optical pumping with an ^4He -lamp [Eq. (B.22)] is less than for the other two processes (Eqs. (B.23) and (B.24)] especially when the collision mixing is small.

To summarize, it has been shown that the reabsorption factor is calculated with Eqs. (B.9) to (B.18). A number of approximations were hereby made:

- a. The relative transition probabilities used here were taken from perturbation theory calculations of the hyperfine structure in ^3He (Tim72).
- b. The spectrum was divided into five groups and it was assumed that a photon belonging to a particular group excites only transitions belonging to that group and none outside the group.
- c. All photon densities, metastable and excited atom densities were assumed to be constant throughout the gas cell.
- d. The "escape" term [Eq. (B.7)] provides only an approximation for the leakage rate of photons out of the system, which should be described by a more detailed function of the geometry.
- e. Implicit in the use of the absorption factor a is the assumption that the photoabsorption cross section for the relevant line in the ^4He spectrum equals that of the same line in the spectrum of the reemitted light.

The theory presented here can be improved, for example, by using measured relative absorption and emission probabilities, and extending the formulas to allow for spatial dependence.

REFERENCES

- Arn66 Arndt, R.A., and M.H. MacGregor, 1966, in: *Methods in Computational Physics*, Vol. 6, eds. B. Alder et al., Academic Press, New York, pp. 253-296.
- Bak69 Baker, S.D., D.H. McSherry and D.O. Findley, 1969, *Phys. Rev.*, 179, 1616-1621.
- Bak71 Baker, S.D., T.A. Cahill, P. Catillon, J. Durand, and D. Garetta, 1971, *Nucl. Phys.*, A160, 428-436.
- Bec74 Beckmann, R., U. Holm, and K. Lorenzen, 1974, *Z. Physik*, 271, 89-91.
- Bec75 Beckmann, R., U. Holm, and B. Lindner, 1975, *Z. Physik*, A275, 319-321.
- Bec77 Beckmann, R., U. Holm, and D. Muller, 1977, *Nucl. Instrum. Methods*, 141, 525-527.
- Ber80 Berg, H., W. Arnold, E. Huttel, H.H. Krause, J. Ulbricht, and G. Clausnitzer, 1980, *Nucl. Phys.*, A334, 21-34.
- Bha82 Bhaskar, N.D., W. Happer and T. McClelland, 1982, *Phys. Rev. Lett.*, 49, 25-28.
- Bir81 Birchall, J., W.T.H. van Oers, H.E. Conzett, P. von Rossen, R.M. Larimer, J. Watson, and R.E. Brown, 1981, in: *AIP Conference Proceedings No 69, 'Polarization Phenomena in Nuclear Physics-1980'*, eds. G.G. Ohlsen, et al., American Institute of Physics, New York, pp. 1263-1265.
- Bro78 Brown, R.E., 1978, in: *AIP Conference Proceedings No 47, 'Clustering Aspects of Nuclear Structure and Nuclear Reactions'*, eds. W.T.H. Van Oers et al., American Institute of Physics, New York, pp. 90-111.
- Bye67 Byerly, R., 1967, PhD Thesis, Rice University, Houston, pp. 124.
- Che82 Cheng, C., K.W. Giberson, A.R. Harrison, F.K. Tittel, F.B. Dunning, and G.K. Walters, 1982, *Rev. Sci. Instrum.*, 53, 1434-1437.
- Coh69 Cohen-Tannoudji, C., J. DuPont-Roc, S. Haroche, and F. Laloe, 1969, *Phys. Rev. Lett.*, 22, 758-760.
- Col63 Colegrove, F.D., L.D. Schearer and G.K. Walters, 1963, *Phys. Rev.*, 132, 2561-2572.
- Cra83 Crampton, S.B., P.J. Nacher, M. Leduc, and F. Laloe, Report to a workshop on 'High intensity polarized proton sources', TRIUMF, Vancouver, May 23-28, 1983.

- Dan71a Daniels, J.M., and R.S. Timsit, 1971, *Can. J. Phys.*, 49, 525-538.
- Dan71b Daniels, J.M., and R.S. Timsit, 1971, *Can. J. Phys.*, 49, 539-544.
- Dan71c Daniels, J.M., R.S. Timsit, A.D. May, and V.L.S. Yuen, 1971, *Can. J. Phys.*, 49, 517-524.
- Dar72 Darves-Blanc, R., Nguyen Van Sen, J. Arvieux, J.C. Gondrand, A. Fiore and G. Perrin, 1972, *Nucl. Phys.*, A191, 353-360.
- DeJ81 De Jong, M.S., 1981, PhD Thesis, University of Manitoba, Winnipeg, pp. 115.
- Dri67 Drigo, L., G. Pisent, 1967, *Nuovo Cimento*, 51B, 419-436.
- Dup73 Dupont-Roc, J., M. Leduc and F. Laloe, 1973, *J. Phys. (Paris)*, 34, 961-975.
- Fia73 Fiarman, S., and W.E. Meyerhof, 1973, *Nucl. Phys.*, A206, 1-64.
- Gam65 Gamblin, R.L., and T.R. Carver, 1965, *Phys. Rev.*, 138, A946-A960.
- Gan73 Ganiere, J.G., 1973, *Helv. Phys. Acta*, 46, 129-145.
- Gib82 Giberson, K.W., C. Cheng, M. Onellion, F.B. Dunning, and G.K. Walters, 1982, *Rev. Sci. Instrum.*, 53, 1789-1790.
- Gre64 Greenhow, R.C., 1964, *Phys. Rev.*, 136, A660-A661.
- Hal74 Hale, G.M., J.J. Devaney, D.C. Dodder, and K. Witte, 1974, *Bull. Am. Phys. Soc.*, 19, 506.
- Har68 Harbison, S.A., F.G. Kingston, R.J. Griffiths, A.R. Johnston, and J.H.P.C. Megaw, 1968, *Nucl. Phys.*, A112, 137-144.
- Har70 Harbison, S.A., R.J. Griffiths, N.M. Stewart, A.R. Johnston, and G.T.A. Squier, 1970, *Nucl. Phys.*, A150, 570-586.
- Hee81 Heeringa, W., 1981, in: AIP Conference Proceedings No 69, Polarization Phenomena in Nuclear Physics-1980, eds. G.G. Ohlsen, et al., American Institute of Physics, New York, pp. 770-784.
- Hil72 Hilger, W., 1972, *Rev. Sci. Instrum.*, 43, 1630-1632.
- Hou78 Houdayer, A., N.E. Davison, S.A. Elbakr, A.M. Sourkes, W.T.H. van Oers, and A.D. Bacher, 1978, *Phys. Rev.*, C18, 1985-2000.
- Hub69 Huber, P., C. Leemann, U. Rohrer, and F. Seiler, 1969,

Helv. Phys. Acta, 42, 907-909.

- Hut71 Hutson, R.L., N. Jarmie, J.L. Detch, and J.H. Jett, 1971, Phys. Rev., C4, 17-22.
- LaF80 La France, P., and P. Winternitz, 1980, J. Physique, 41, 1391-1417.
- Lan58 Lane, A.M., and R.G. Thomas, 1958, Rev. Mod. Phys., 30, 257-352.
- Lee71 Leemann, C., H. Burgisser, P. Huber, U. Rohrer, H. Paetz-Schieck, and F. Seiler, 1971, Helv. Phys. Acta, 44, 141-159.
- Lef82 Lefevre-Seguin, V., P.J. Nacher and F. Laloe, 1982, J. Phys. (Paris), 43, 737-753.
- Lif65 Lifshitz, J., and R.H. Sands, 1965, Bull. Am. Phys. Soc., 10, 1214.
- Kim64 Kim, C.C, S.M. Bunch, D.W. Devins, and H.H. Forster, Nucl. Phys., 58, 32-48.
- McA68 McAdams, H.H., 1968, Phys. Rev., 170, 276-285. 436-438.
- McS69 McSherry, D.H., S.D. Baker, G.R. Plattner, and T.B. Clegg, 1969, Nucl. Phys., A126, 233-240.
- McS70 McSherry, D.H., and S.D. Baker, 1970, Phys. Rev., C1, 888-892.
- Mol80 Mollenauer, L.F., 1980, Optics Letters, 5, 188-190.
- Mor69 Morrow, L.W., and W. Haeberli, 1969, Nucl. Phys., A126, 225-232.
- Mor75 Morales, J.R., T.A. Cahill, D.J. Shadoan, and H. Willmes, 1975, Phys. Rev., C11, 1905-1912.
- Mul78 Muller, D., R. Beckmann and U. Holm, 1978, Nucl. Phys., A311, 1-10.
- Mur79 Murdoch, B.T., D.K. Hasell, A.M. Sourkes, W.T.H. Van Oers, and R.E. Brown, 1979, Los Alamos Scientific Laboratory, Preprint LA-UR-79-3423, to be published.
- Nac82 Nacher, P.J., M. Leduc, G. Trenc and F. Laloe, 1982, J. Phys. Lett. (Paris), 43, L525-L529.
- Pav70 Pavlovic, M., and F. Laloe, 1970, J. Phys. (Paris), 31, 173-194.
- Pet72 Peterson D.G., 1972, Nucl. Instrum. Meth., 104, 451-454.
- Phe58 Phelps, A.V., 1958, Phys. Rev., 110, 1362-1368.

- Ph162 Phillips, G.C., R.R. Perry, P.M. Windham, G.K. Walters,
L.D. Schearer and F.D. Colegrove, 1962, Phys. Rev. Lett., 9,
502-504.
- Pin74 Pinard, M., and J. Van Der Linde, 1974, Can. J. Phys., 52,
1615-1621.
- Rad81 Rad, F.N., R.G. Graves, D.P. Saylor, M.L. Evans,
E.P. Chamberlin, J.W. Watson, and L.C. Northcliffe, 1981,
Nucl. Instr. Meth., 190, 459-478.
- Rog83 Roger, M., J.H. Hetherington, J.M. Delrieu, 1983,
Rev. Mod. Phys., 55, 1-64.
- Roh71 Rohrer, U., P. Huber, C. Leemann, H. Meiner, and F. Seiler,
1971, Helv. Phys. Acta, 44, 846-865.
- Sch65 Schearer, L.D., and G.K. Walters, 1965, Phys. Rev., 139,
A1398-A1402.
- Sch67 Schearer, L.D., 1967, Phys. Rev., 160, 76-80.
- Sch70 Schearer, L.D., and L.A. Riseberg, 1970, Phys. Lett., 33A,
325-326.
- Sil59 Silverstein, E.A., 1959, Nucl. Instrum. Meth., 4, 53-66.
- Sou76 Sourkes, A.M., A. Houdayer, W.T.H. Van Oers, R.F. Carlson,
R.E. Brown, 1976, Phys. Rev., C13, 451-460.
- Smy64 Smythe, R., 1964, Rev. Sci. Instrum., 35, 1197-1200.
- Sza70 Szaloky, G., P. Huber, C. Leemann, U. Rohrer, and F. Seiler,
1970, Helv. Phys. Acta, 43, 745.
- Sza75 Szaloky, G., 1975, PhD Thesis, University of Basel, Switzerland,
pp. 30.
- Sza78a Szaloky, G., and F. Seiler, 1978, Nucl. Phys., A303, 57-66.
- Sza78b Szaloky, G., F. Seiler, W. Gruebler and V. Konig, 1978,
Nucl. Phys., A303, 51-56.
- Tim70 Timsit, R.S., 1970, PhD Thesis, University of Toronto, Toronto,
pp. 196.
- Tim71a Timsit, R.S., and J.M. Daniels, 1971, Can. J. Phys., 49,
545-559.
- Tim71b Timsit, R.S., J.M. Daniels, and A.D. May, 1971, Can. J. Phys.,
49, 560-575.
- Tim71c Timsit, R.S., J.M. Daniels, E.I. Dennig, A.K.C. Kiang and

- A.D. May, 1971, Can. J. Phys., 49, 508-516.
- Tim72 Timsit, R.S., and A.D. May, 1972, Can. J. Phys., 50, 67-72.
- Tim76 Timsit, R.S., and J.M. Daniels, 1976, Rev. Sci. Instrum., 47, 953-959.
- Tiv68 Tivol, W., 1968, Lawrence Radiation lab report UCRL-18137, unpublished.
- Tom62 Tombrello, T.A., C.M. Jones, G.C. Phillips and J.L. Weil, 1962, Nucl. Phys., 39, 541-550.
- Tom65 Tombrello, T.A., 1965, Phys. Rev., 138, B40-47.
- War75 Ware, R.H., W.R. Smythe and P.D. Ingalls, 1975, Nucl. Phys., A242, 309-316.
- Wat77 Watson, J.W., H.E. Conzett, R.M. Larimer, B.T. Leeman, and, E.J. Stephenson, 1977, Bull. Am. Phys. Soc., 22, 531.
- Wie67 Wiese, W.L., M.W. Smith, B.M. Glennon, 1966, National Standard Reference Series, Atomic Transition Probabilities, Vol. I, He through Ne.